

ABSTRACT

Title of Document: DIFFUSION OF OXYGEN AND LITHIUM ISOTOPES AT A CONTACT BETWEEN THE BUSHVELD COMPLEX AND METASEDIMENTARY ROCK: IMPLICATIONS FOR THE TIMESCALE OF PHEPANE DOME DIAPIRISM

Rachel H. Potter, Master of Science, 2009

Directed By: Dr. Sarah Penniston-Dorland, Department of Geology

Within the Eastern Lobe of the Bushveld Complex, the Phepane Dome is a circular structure of metasedimentary rock hypothesized to have formed as a wallrock diapir. To constrain the duration of Phepane Dome formation using one-dimensional diffusion models of oxygen and lithium exchange between the Bushveld Complex and the Phepane Dome, samples taken across the contact between these two lithologies were measured for their O and Li isotopic compositions and Li concentrations. Models of O and Li diffusion through melt and through aqueous fluid were fit to the data, resulting in a diffusive distance of 1.0 m for oxygen and 14.1 m for lithium. Using experimentally constrained parameters for O and Li diffusion, a range of 2 kyrs to 2 Myrs was calculated from the diffusive distances. This is consistent with previous studies of the time for crystallization of the Bushveld Complex and a model of Phepane diapir development.

DIFFUSION OF OXYGEN AND LITHIUM ISOTOPES AT A CONTACT
BETWEEN THE BUSHVELD COMPLEX AND METASEDIMENTARY ROCK:
IMPLICATIONS FOR THE TIMESCALE OF PHEPANE DOME DIAPIRISM

By

Rachel H. Potter

Thesis submitted to the Faculty of the Graduate School of the
University of Maryland, College Park, in partial fulfillment
of the requirements for the degree of
Master of Science
2009

Advisory Committee:
Dr. Sarah Penniston-Dorland, Chair
Dr. James Farquhar
Dr. Roberta Rudnick

© Copyright by
Rachel H. Potter
2009

Acknowledgements

Many people have extended their knowledge, support and time to me during this project, without which this thesis could not have been completed. No one deserves acknowledgement more than Dr. Sarah Penniston-Dorland, who has been a constant mentor and supporter throughout this project. She broke her leg as the first samples were collected, but continued to work and inspire me towards the completion of a rigorous scientific study, even returning to South Africa in each of the following summers to collect more samples and endlessly searching for a Universal stage that I could use. I am grateful for her guidance and for the guidance of my committee members, Dr. James Farquhar and Dr. Roberta Rudnick.

This work started in South Africa, with the support and assistance of Dr. Judith Kinnaird and Dr. Paul Nex from the University of Witwatersrand, Johannesburg. Dr. Michael Brown and Dr. Boz Wing introduced the unusual setting of the Phepane Dome, and Dr. Sarah Penniston-Dorland as well as a Graduate Student Research grant from the Geological Society of America enabled me to visit and sample the Phepane Dome in the countryside of South Africa. Field work at the Phepane Dome was accomplished first with Dr. Boz Wing, and then the following summer with Dr. Tim Johnson, both of whom provided their invaluable insight and expertise of the geology of the Phepane Dome. Geologic maps of the region were provided by Jim Crotty and George Chunnnett of Anglo Platinum.

I would like to thank Dr. John Valley and Dr. Mike Spicuzza of the Department of Geology and Geophysics at the University of Wisconsin-Madison for their oxygen isotope analyses of my samples, as well as Dr. Peter Zavalij of the X-ray Crystallography Laboratory at the University of Maryland, who helped me prepare the samples even with only a day's notice. I also thank Dr. Sorena Sorensen of the Smithsonian Institute for assisting me with Cathodoluminescence optical-microscopy.

I express my gratitude for the support of the Geology Department at the University of Maryland. Many professors, researchers, graduate students, and lab assistants have contributed to my study here. Dr. Richard Ash and Dr. Phil Piccoli

offered their assistance with smiles whenever I asked. Their expertise in the Plasma Lab and with the Electron Microprobe was crucial to this work. I thank the all of the Graduate Students who helped me in the lab and listened and discussed my research with me. Their knowledge and friendship has been indispensable throughout my graduate career. I am especially grateful for the love and support of Mr. (soon to be Dr.) Thomas Ireland, who made graduate student life even more enjoyable. A final thank you goes to my family, who wished I hadn't gone so far away, but supported me continuously.

Table of Contents

Acknowledgements.....	ii
Table of Contents.....	iv
List of Tables.....	v
List of Figures.....	vi
Chapter 1: Introduction.....	1
1.1: Overview of Phepane Dome diapirism.....	1
1.2: Previous timescale estimates.....	4
1.3: Purpose and importance of study.....	7
Chapter 2: Diffusion Theory and Modeling.....	9
2.1: Using diffusion to constrain duration.....	9
2.2: Diffusion parameters.....	10
2.3: Governing equations.....	12
2.4: Previous studies.....	15
Chapter 3: Geologic Setting.....	17
3.1: Bushveld Complex.....	17
3.2: Contact aureole of the Bushveld Complex.....	20
3.3: Phepane Dome.....	21
3.4: Diapirism of the Phepane Dome.....	23
Chapter 4: Analytical Methods.....	25
4.1: Sampling methodology.....	25
4.2: Sample characterization technique.....	28
4.3: Dihedral angle analyses.....	29
4.4: Oxygen isotope measurement technique.....	31
4.5: Lithium isotopic and compositional measurement technique.....	32
Chapter 5: Results.....	35
5.1: Petrology.....	35
5.2: Evidence for melt.....	41
5.3: Evidence for aqueous fluid.....	44
5.4: Oxygen isotopic compositions.....	54
5.5: Lithium concentrations.....	59
5.6: Lithium isotopic compositions.....	68
Chapter 6: Discussion and Modeling.....	75
6.1: Oxygen compositions.....	75
6.2: Lithium compositions.....	77
6.3: Lithium fractionation.....	81
6.4: Oxygen models.....	86
6.5: Lithium models.....	92
6.6: Li and O diffusion timescales.....	103
Chapter 7: Conclusions.....	106
7.1: The Phepane Dome-Bushveld Complex system.....	106
7.2: Modeling of lithium and oxygen isotopic exchange.....	107
7.3: Time estimates.....	108
References.....	112

List of Tables

Table 1: Mineral modes of representative rock types.....	37
Table 2: (a) Major element compositions.....	38
(b) Percent error of weight %	40
Table 3: Oxygen isotopic compositions.....	57
Table 4: Li isotopic compositions and concentrations	
(a) of the East Phepane.....	63
(b) of the West Phepane.....	64
(c) of the Transvaal Supergroup.....	64
Table 5: Individual mineral Li concentrations.....	65
Table 6: Time estimates of the Li and O models.....	98

List of Figures

Figure 1: (a) Bushveld Complex of South Africa.....	2
(b) Eastern Lobe of the Bushveld Complex.....	3
Figure 2: Model of Phepane diapirism by Gerya et al. (2004).....	6
Figure 3: Diffusion profiles from different timescales of exchange.....	16
Figure 4: Sedimentary lithologies.....	19
Figure 5: Phepane Dome map.....	22
Figure 6: The Phepane diapir: a 3-D schematic from Gerya et al. (2004).....	24
Figure 7: Transects taken at the Phepane Dome.....	26
Figure 8: Sedimentary samples from the Transvaal Supergroup.....	27
Figure 9: Example dihedral angles.....	31
Figure 10: Dihedral angles in thin section.....	42
Figure 11: Histograms of dihedral angle measurements.....	43
Figure 12: Fluid inclusions in quartz.....	45
Figure 13: CL images of sedimentary rock and non-luminescent textures.....	51
Figure 14: CL images of P06-19.....	52
Figure 15: CL images of blue luminescent textures.....	53
Figure 16: Oxygen isotopic compositions for the two measured transects.....	58
Figure 17: (a) Li concentrations of the East Phepane.....	66
(b) Li concentrations of the West Phepane.....	67
Figure 18: Feldspar abundance compared to Li whole rock concentration.....	68
Figure 19: (a) Lithium isotopic compositions of the East Phepane.....	72
(b) Lithium compositions of the East Phepane Transects 06 and 07.....	73
(c) Lithium isotopic compositions of the West Phepane.....	74
Figure 20: Li concentration vs. Li isotopic composition.....	83
Figure 21: (a) Model of oxygen isotopic exchange in the East Phepane.....	90
(b) Model of oxygen isotopic exchange in the West Phepane.....	90
(c) Maximum diffusive distance in oxygen isotope exchange models...	91
Figure 22: (a) Model of Li diffusion in the East Phepane.....	99
(b) Beta values of the East Phepane model.....	100
Figure 23: Model of Li diffusion in the West Phepane Small Scale Transect.....	101
Figure 24: Model of Li diffusion in the West Phepane Large Scale Transect.....	102

Chapter 1: Introduction

1.1: Overview of Phepane Dome diapirism

The Bushveld Complex of South Africa was formed as mafic to ultramafic magma intruded sedimentary rocks of the Transvaal Supergroup ~2060 Ma (Walraven et al., 1990; Buick et al., 2001) (Figure 1a). Domes of metasedimentary rocks within the mafic rock of the eastern lobe of the Bushveld Complex are interpreted to have formed as diapirs of partially melted, sedimentary footwall rock that rose through the denser mafic magma (Uken and Watkeys, 1997) (Figure 1b). Diapirism is believed to be triggered by crustal loading of the sedimentary rock by long finger-shaped injections of denser mafic magma, with diapirs initiating in the inter-finger areas (Uken and Watkeys, 1997). As the magma of the Bushveld Complex continued to intrude, sedimentary perturbations in the inter-finger areas heated, partially melted, and were able to rise as colder diapirs into the more dense magma. The Phepane Dome is a circular exposure of metasedimentary rocks surrounded by Bushveld Complex rock, and therefore hypothesized to be one of these sedimentary diapirs (Gerya et al., 2004; Johnson et al., 2004). However, the timescale for the diapir to initiate, rise, and freeze into the Bushveld Complex is uncertain.

Figure 1a: Bushveld Complex of South Africa

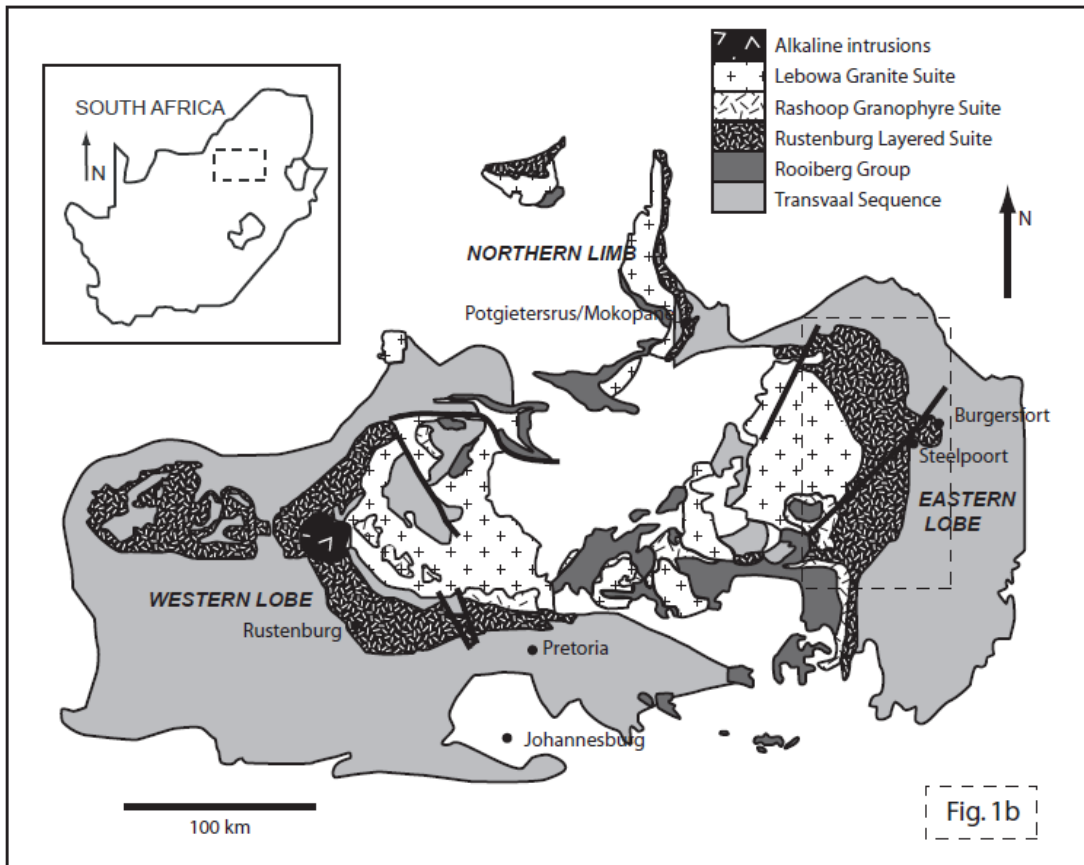


Figure 1a: Map of the Bushveld Complex in South Africa modified from Kinnaird et al. (2005).

Figure 1b: Eastern Lobe of the Bushveld Complex

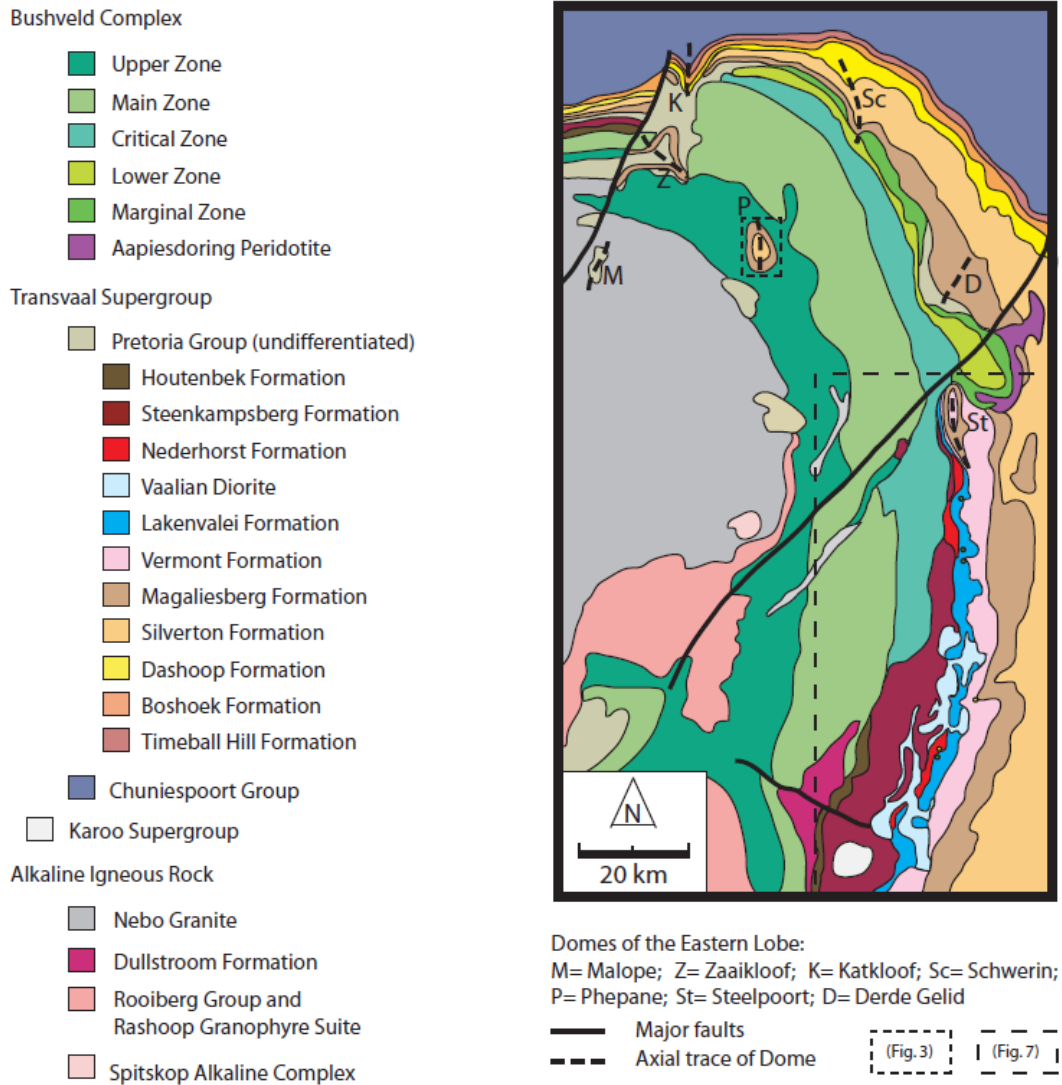


Figure 1b: Close up of Eastern Lobe (dotted line in Figure 1a) showing each igneous Zone, the sedimentary rocks of the aureole, and the metasedimentary domes within the Bushveld Complex. Modified from Clarke et al. (2005) and geologic maps provided by the Geological Society of South Africa.

1.2: Previous timescale estimates

Two previous studies provide time constraints on the development of the Phepane Dome diapir. The first study models the crystallization of the Bushveld Complex magma (Cawthorn and Walraven, 1998), while the second models the formation of the Phepane Dome diapir (Gerya et al., 2004). Cawthorn and Walraven (1998) use a thermal model to determine the amount of time a 7.5 km thick intrusion the size of the Bushveld Complex would require to cool and crystallize. This is accomplished using cells of the same thickness to represent layers of wallrock with an initial thermal gradient, and adding cells of hot magma according to each stage of Bushveld Complex magma injection. The temperature of each wallrock and magma cell is calculated using equations of conductive heat flow to determine the changes in heat content of adjacent cells for small increments of time. The model accounts for the crystallization or partial crystallization between stages of magma injection by subtracting latent heat of solidification from heat content in the temperature calculations. Using geochemical and mineralogical evidence to constrain the thickness of each stage, the model begins with an estimated 75 kyrs of 1300°C and 1200°C magma injections. After 180 kyrs, the entire intrusion has cooled to less than 900°C. The model assumes a solidus temperature of ~900°C, rendering the intrusion completely crystallized by 200 kyrs, and thus prohibiting further diapiric rise. Therefore, according to this model, the Phepane Dome diapir must form within this 200 kyr time period.

The second model uses inferred viscosity and thermal properties of the sedimentary rock and heat flow associated with the Bushveld Complex magma to

predict the development of the Phepane diapir (Gerya et al., 2004). The model relies on the formation of the diapir from initial perturbations in the sedimentary rock caused by linear crustal loading of the Bushveld Complex magma (Figure 2). The duration of Phepane Dome formation is resolved from time steps in the model as the diapir develops. Each time step is calculated using coupled equations representing changes in temperature, viscosity, and material flow with time over a two dimensional grid. The grid is 30 km across, which represents the wavelength between diapirs, and 22 km deep. The different rock types are accounted for by changes in the physical properties of the model with depth. At the surface, the felsic volcanics of the Rooiberg Group are approximated by wet granite flow properties and gradually increase in temperature (from 25°C to 625°C) while decreasing in viscosity (10^{24} to 10^{21} Pa·s) to 5 km depth. From 5 km to 13 km depth, the Bushveld magma is 1200°C with lower viscosity (10^{18} Pa·s) and approximated by plagioclase (An75). From 13 km to 22 km, the Transvaal sedimentary rock is 400°C and has the greatest viscosity (10^{24} Pa·s). At the top of the Transvaal Group (13 km), a one km tall anticline is used for the initial perturbation in the Transvaal sedimentary rock. The model results in a 200-300°C gradient from the cooler core to hotter rim of the diapir. The viscosity inverts as the diapir develops, resulting in a lower viscosity for the Transvaal Group relative to the Bushveld magma. When the viscosity of the Bushveld magma becomes too great as solidification occurs less than 900°C, the diapir is immobilized. Gerya et al. (2004) found the formation of the diapir within the hotter mafic rock to be plausible in one million years.

Figure 2: Model of Phepane diapirism by Gerya et al. (2004)

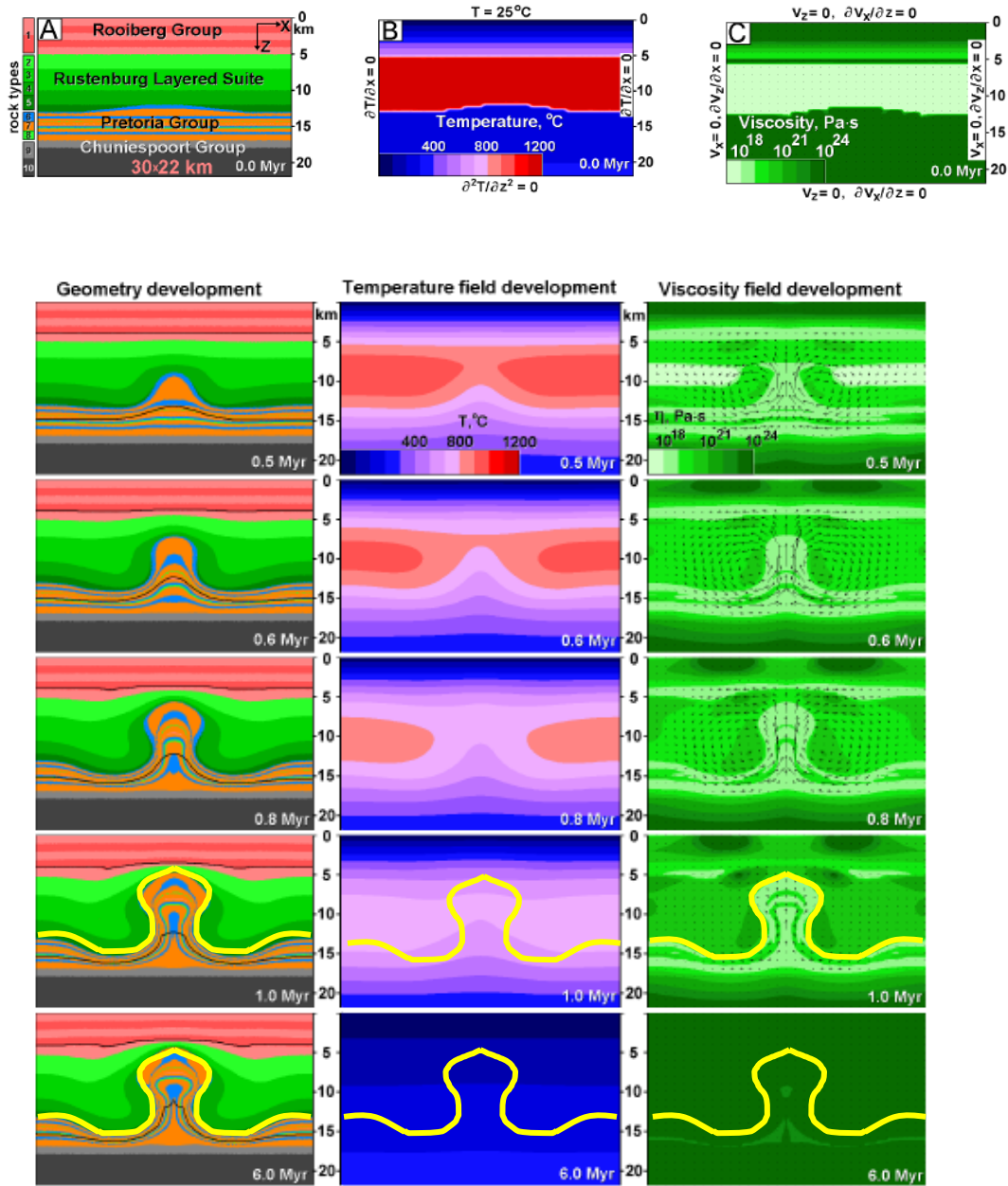


Figure 2: Model by Gerya et al. (2004) of Phepane Dome diapir formation. **(top)** Initial conditions for Material Flow model (A), Temperature model (B), and Viscosity model (C). **(below)** Diapir formation with time. The Material Flow model is on the left, Temperature in the middle, and Viscosity on the right. From the model below, it can be seen that a diapir will form and be frozen in by 1 million years (yellow line).

1.3: Purpose and importance of study

The formation of the Phepane Dome as a diapir of colder material rising into the intruding Bushveld Complex magma opposes the standard assumption that colder material is more dense. In magmatic settings, diapirism is usually described as rising melt that is hotter and therefore a lower density than the surrounding country-rock. In the case of the Phepane Dome, the diapir is colder country-rock that rises into the hotter magma because the colder sedimentary material is less dense than the mafic-ultramafic magma. However, there is limited study of these thermally dynamic settings where chemical buoyancy plays such an important role. Studies have hypothesized the occurrence of cold diapirism in subduction zones, where diapirs of hydrous peridotite from the subducting slab rise into the hotter, dry mantle (Hall and Kincaid, 2001; Gerya and Yuen, 2003). This study intends to aid in the understanding of these settings by investigating the timescale of cold diapirism.

The two models described above present the only known time estimates for the Phepane Dome formation as a diapir in 200 kyrs and 1 Myrs. This study investigates the two given time estimates by measuring oxygen and lithium isotopic compositions across a contact between the Phepane Dome and the Bushveld Complex and fitting the results with a numerical diffusion model. The best fit model to the data will constrain the amount of time diffusion of lithium and oxygen occurred in this system, and therefore constrain the duration of the Phepane diapir formation. Thus, this study provides another time estimate for the processes involved during this cold diapirism.

In addition to determining the duration of diffusion, this study is the first to couple both Li and O as chemical tracers of diffusion, directly comparing the two systems. While previous studies have used O isotopic compositions at intrusion-wallrock contacts (Shieh and Taylor, 1969; Cartwright and Valley, 1991; Park et al., 1999), and recent studies have used Li isotopic composition and concentrations in contact metamorphic settings (Teng et al. 2006a; Marks et al., 2007), no study has used both systems and compared the diffusion of O to that of Li. This study provides an important assessment of each system at the same contact metamorphic setting. It is an important corollary to the experimental studies that show that Li will diffuse orders of magnitude faster than other components in basaltic and rhyolitic melts (Richter et al., 2003).

Chapter 2: Diffusion Theory and Modeling

2.1: Using diffusion to constrain duration

When two lithologies with different chemical and isotopic compositions are placed directly adjacent at elevated temperature, diffusional exchange will occur across the contact as the system tries to reach equilibrium. Therefore, during intrusion of magma and subsequent metamorphism of country-rock, diffusional exchange smoothes out the initially steep compositional gradient between the two disparate rock types. If the system cools and diffusion ceases before complete equilibration between the two lithologies is achieved, then a diffusion profile across the contact will be “frozen” in. Isotopic measurements along a transect perpendicular to the contact will reveal the shape and extent of the profile. Because the shape of the profile depends on the amount of time that diffusion was able to occur, the duration of the metamorphic event may be constrained from examination of the diffusion profile (see Figure 3).

The inherent assumptions in this determination are that diffusion was able to occur in the same amount of time as the formation of the Phepane Dome, and that there has been no resetting of the rocks in a subsequent event. The latter is a reasonable assumption, because there have not been any subsequent metamorphic events documented in the region of the Bushveld Complex. The first assumption can also be accepted, because the formation of the Phepane Dome was caused by heating and cooling of the Transvaal Sedimentary rocks. The start of isotopic exchange occurs after the sedimentary rock reaches the temperature at which minerals begin to

exchange, which is also known as the closure temperature when minerals stop exchanging during cooling. Isotopic exchange occurs as long as the rock stays above this temperature, and therefore diffusive exchange between the two lithologies depends on this temperature. In the Phepane Dome, the termination of diffusion will occur as both the meta-sedimentary rocks and the mafic magma cool. Because the Phepane Dome is cooler material, it should aid in the local cooling of the Bushveld Complex magma. Both the Cawthorn and Walraven (1998) and the Gerya et al. (2004) models use a solidus temperature for the Bushveld Complex magma of $\sim 900^{\circ}\text{C}$. While the exact closure temperature for Li is not known, diffusion of Li has been documented at temperatures from $\sim 600^{\circ}$ to 350°C in the contact metamorphic setting of the Tin Mountain pegmatite (Teng et al., 2006a). Thus, diffusion may continue after crystallization, and any time estimation determined from diffusion duration will be a maximum time of formation of the Phepane Dome.

2.2: Diffusion parameters

Before analyzing a diffusion profile, the type of diffusion and the composition of the system must be considered. First, diffusion that occurs due to a sharp compositional discontinuity across a contact requires chemical transport through the rock (Watson and Baxter, 2007). For a near-surface cooling event, this is likely to be transport of the element or isotope of interest through the intergranular medium. This assumes that local equilibrium between the rock and the intergranular medium was maintained during contact metamorphism, which is reasonable considering dissolution-precipitation as the likely mechanism (e.g., Cartwright and Valley, 1991). The type of intergranular medium (dry grain boundaries, fluid, or melt) will affect the

rate of diffusion, or diffusivity, of the element or isotope. For example, diffusion through fluid is much faster than diffusion on dry grain boundaries, because it is easier for atoms to move through a non-rigid medium as there are more “sites” available for the diffusing element or isotope to move into (Cole and Chakraborty, 2001). The connectivity of the fluid medium is also important for the diffusing element or isotope to be transported a significant distance. This is limited by the porosity of the rock, where very low porosities restrict the connectivity of the medium.

Second, the chemical composition of both the diffusing element/isotope and the intergranular medium of the system will affect the ability of the element/isotope to diffuse. This is illustrated by the faster diffusion of oxygen through basalt melt than andesite melt, due to the decreased amount of network forming elements such as Si and Al in basalt melt (Wendlandt, 1991). The presence of water in the system can also affect diffusivity. Diffusion of oxygen is faster through hydrous melts compared to anhydrous melts, and greatest through aqueous fluids (Watson and Baxter, 2007). In rhyolitic melt, this has been attributed to the dominance of molecular H₂O as the carrier of oxygen during diffusive exchange, while other oxygen species (OH⁻, O₂, CO₂) are relatively motionless and only participate in local isotopic exchange with H₂O (Behrens et al., 2007). In aqueous fluids, oxygen may also be transported as O₂, OH⁻, H₃O⁺, and CO₂, which likely move faster through an aqueous fluid than melt due to the decrease in viscosity (Cole and Chakraborty, 2001). However, the presence of water does not affect the diffusivity of cations within crystals (Watson and Baxter, 2007). In aqueous fluids, Li ions can be bonded in tetrahedral coordination with H₂O

(Wunder et al., 2007) or Cl (Teng et al., 2006a). A possible difference between Li diffusivities in aqueous fluid and/or melt has not been quantified, with one constraint for Li diffusion through aqueous fluid coming from a study of ions in seawater that determined cations may diffuse slightly faster than anions (Li and Gregory, 1974).

Additionally, each element has a specific diffusivity, which is due to differences in the mass of the element. For example, the diffusivity of the lighter element lithium is much faster than the diffusivity of oxygen. This difference can range up to three orders of magnitude in melt (Richter et al., 2003). Thus, a lithium atom will diffuse farther than an oxygen atom in the same amount of time. In the same way, the 17% mass difference between Li isotopes causes ${}^6\text{Li}$ atoms to diffuse faster than ${}^7\text{Li}$ atoms (Teng et al., 2006a). Therefore, the relative size of the element or isotope's ionic radius seems insignificant in comparison to the effect of mass differences.

Lastly, the effective partition coefficient also plays a role in the diffusion of an element or isotope. An element or isotope that prefers the fluid will be transported more rapidly than one that is partitioned preferentially into the solid (Bickle and McKenzie, 1987). This may add to the difference in diffusive distances between O and Li, because Li is a fluid mobile element while O can be more compatible.

2.3: Governing equations

Once the system for diffusion is established, the diffusion profile may be modeled, taking into account the parameters explained above. This is accomplished using Fick's second law (Equation 1), which describes one-dimensional diffusion. The singular direction of diffusion is assumed to be perpendicular to the contact, and

is reasonable in situations where the length of the contact is much greater than the diffusion path across the contact. Diffusion is assumed to occur within a static intergranular medium, which can be verified through inspection of the data.

Displacement of the measured diffusive profile to either side of the contact would indicate advection across the contact has also occurred. Because this is not the case, the model uses diffusion through a static medium as the only mechanism of transport. Fick's second law states that the change in concentration with time is proportional to the change in compositional gradient with distance from the contact:

$$\frac{\partial C_i}{\partial t} = D_i \frac{\partial^2 C_i}{\partial x^2} \quad (1)$$

The constant of proportionality is the diffusivity (D) of the element or isotope of choice (i), and C is the concentration of this element or isotope. Fick's second law is solved to determine the concentration C(x,t) at a position that is a certain distance (x) from the contact at a certain time (t) (Crank, 1975).

$$C(x,t) = C^o - \frac{\Delta C}{2} \operatorname{erfc} \left(\frac{x}{2\sqrt{D_e t K_e^{-1}}} \right) \quad (2)$$

The initial concentration at that distance (x) is C^o, the difference between the initial concentrations on each side of the contact is ΔC, the effective diffusivity is D_e, and K_e is the effective partition coefficient that takes into account the porosity (φ) of the rocks, as well as the fractionation of the elements into the solid or fluid (Cartwright and Valley, 1991).

$$K_e = \frac{\rho_s K_c}{\rho_f} (1 - \phi) + \phi \quad (3)$$

The density of the solid and density of the fluid are ρ_s and ρ_f respectively. K_c is the partition coefficient experimentally determined for the element/isotope of choice.

In equation (2), the effective diffusivity D_e must be used to account for the properties of the connected intergranular medium, since diffusivities (D) are measured as diffusion through a melt or fluid. The effective diffusivity is defined by the porosity (ϕ) and tortuosity (τ) of the system, as well as the specific diffusivity (D) of the element or isotope present in the intergranular medium (Cartwright and Valley, 1991).

$$D_e = \phi D \tau \quad (4)$$

Using these equations, the concentrations at each finite distance (x) from the contact after a certain amount of time (t) may be solved for, resulting in a diffusion profile across the contact. This modeled profile is matched to the actual measured diffusion profile to solve for the diffusive distance $\sqrt{D_e t K_e^{-1}}$ from equation (1) and to resolve the duration of a metamorphic event by estimating the effective diffusivity and effective partition coefficient and solving for (t).

It is recognized that the diffusive Li isotopic profile is different in shape compared to an oxygen isotopic profile (Teng et al., 2006a). This difference is caused by the faster diffusion of ^6Li relative to ^7Li , causing the rock with greater Li concentration to lose ^6Li faster and become ^7Li enriched right at the contact. The difference in diffusivity of ^6Li relative to ^7Li is quantified through the empirical term β (Richter et al., 2003).

$$\frac{D_{^6\text{Li}}}{D_{^7\text{Li}}} = \left(\frac{m_{^7\text{Li}}}{m_{^6\text{Li}}} \right)^\beta \quad (5)$$

A larger β will produce a larger isotope fractionation at the contact, but does not control the diffusive distance. For condensed material, β is <0.5 , with studies finding $\beta= 0.215$ for silicate melts, $\beta= 0.12$ for aqueous fluid, and $\beta < 0.071$ for Li diffusion in water (Richter et al, 2003; Teng et al., 2006; Fritz, 1992 and Richter et al., 2006; respectively). To model Li diffusion with differing isotopic diffusivities, the ^7Li and ^6Li concentrations are modeled separately, with each D_{Li} calculated from β . The $\delta^7\text{Li}$ at each distance from the contact can be calculated from the modeled isotopic concentrations at that distance. This is in contrast to the diffusion of oxygen isotopes, in which the $\delta^{18}\text{O}$ values are modeled as concentration.

The distance of Li and O isotopic exchange across a contact depends on the length of time (t) that diffusional exchange occurs. Because Li diffuses faster than heavier elements, it should diffuse farther from the contact than O in the same amount of time. Therefore, while a major goal of this study is to constrain the timescale for active diffusion in the Bushveld Complex-Phepane Dome system, it also provides a comparison of Li and O isotopic diffusion.

2.4: Previous studies

Several studies have modeled diffusion of oxygen isotopes at magma and wall-rock contacts (e.g., Shieh and Taylor, 1969; Cartwright and Valley, 1991; Park et al., 1999). Recently, studies have modeled the diffusion of Li isotopes in contact metamorphic settings (Teng et al. 2006a; Marks et al., 2007). These studies use constraints from the rock types present as well as empirically defined diffusion data to determine the parameters for the model (e.g., K_e and D_e , equations (3) and (4)). The model is calculated using initial compositions of each rock type determined from

the measured values of samples farthest from the contact. The results of the model are matched to the measured oxygen or lithium isotopic values of the transect. The time, or range in time, that produces the closest fit to the data corresponds to the formation and cooling time of the system. This method is used to constrain the timescale of high temperature diffusion in the Bushveld Complex and Phepane Dome. Because it is unknown if the dominant process was diffusion through fluid or diffusion through melt, both systems will be used in determining the parameters of the models.

Figure 3: Diffusion profiles of different timescales

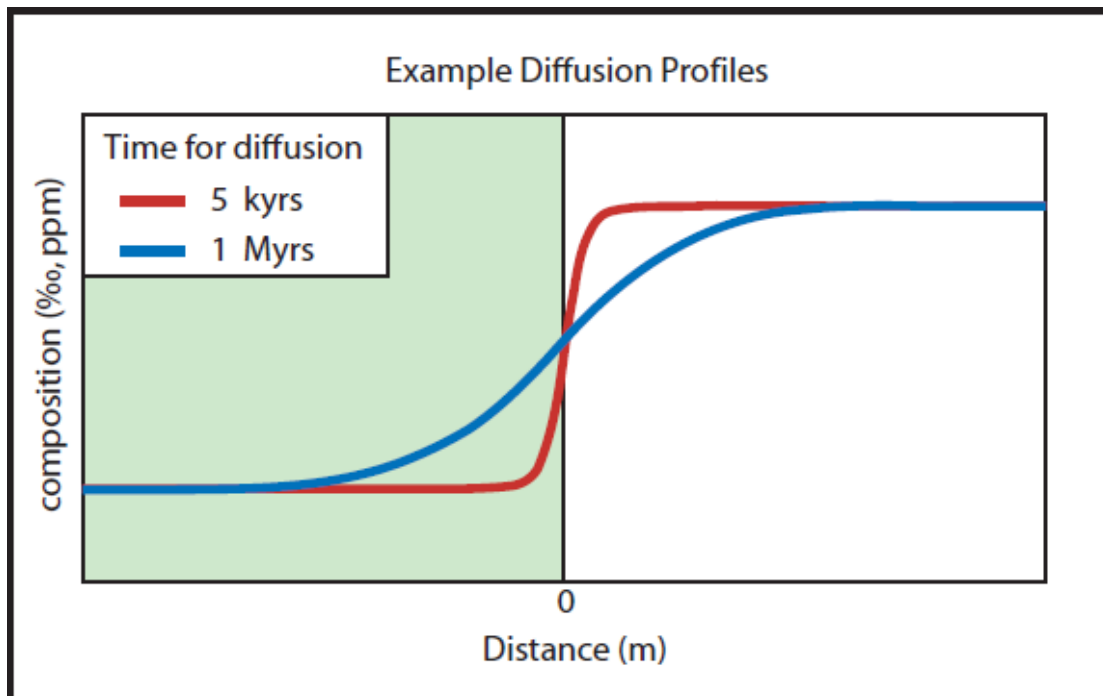


Figure 3: When two rocks of differing composition are emplaced next to each other, diffusive exchange across the contact smooths the initial compositional difference. The distance that diffusion reaches into each rock type depends on the amount of time the two rocks were able to exchange, where longer timescales create broader diffusion profiles (blue profile vs. red profile).

Chapter 3: Geologic Setting

3.1: Bushveld Complex

The Bushveld Complex is a sill-like intrusion of the mafic-ultramafic Rustenburg Layered Suite into the Transvaal Basin of South Africa (Figure 1a). The estimated volume of the Bushveld Complex is 370,000 to 600,000 cubic kilometers, and outcrop is recognized over a distance of 400 kilometers east to west (Cawthorn and Walraven, 1998). The structure forms a bowl shape, which has been divided into a Western Lobe, an Eastern Lobe, and a thin 100 kilometer Northern extension. Important ore concentrations are found throughout the Complex, including 75% of the world's Pt reserves and 50% of the world's Pd reserves (Cawthorn, 1999).

The entire Complex formed through multiple injections of magma into the clastic and chemical sedimentary rocks of the Transvaal Supergroup (Cawthorn and Walraven, 1998). The Transvaal Supergroup sediments were deposited onto the Archean granite of the Kaapvaal craton, and consist of Archean basinal rocks overlain by the Black Reef Formation, the Chuniespoort Group carbonates and banded iron formation, and the Proterozoic age Pretoria Group (Figure 4) (Eriksson et al., 2001). Prior to intrusion, minor and major volcanic episodes occurred approximately concurrent to Transvaal sediment deposition. The rhyolite and andesite lavas of the Rooiberg Felsite formed just before Bushveld Complex intrusion, but lie stratigraphically above it (Hill et al., 1996). The subjacent Dullstroom Basalt Formation and Hekpoort Andesite are used to determine the age of Pretoria Group sedimentary rocks. Calculated Pb-Pb and Rb-Sr isochron ages for these two volcanic

formations all fall around the preferred age of 2224 ± 21 Ma, taken from a Rb-Sr whole rock isochron age from the Hekpoort Andesite (Walraven et al., 1990).

The intrusion of the Bushveld Complex occurred at ~ 2060 Ma, as the Rustenburg Layered Suite was emplaced between the Transvaal sedimentary rock and the Rooiberg Felsite (Walraven et al., 1990; Buick et al., 2001). The Bushveld Complex was intruded in stages of multiple magma injections. The stages are recognized by five compositional zones: the Marginal, Lower, Critical, Main, and Upper Zones. These zones are distinguished by different mafic to ultramafic compositions. During crystallization of each stage, the magma fractionated to form layers of variable mafic compositions (Cawthorn and Walraven, 1998). Subsequent felsic intrusions of the Lebowa Granite Suite overlie the Rustenburg Layered Suite (see Figure 1a). This granite is also found as plutons intruding the mafic rock of the Eastern Lobe (Hill et al., 1996). Much of the granite has been disturbed by open system behavior, but a minimum preferred age of $2049 +69/-75$ Ma for the Lebowa Granite Suite is resolved from separate intrusions with similar Pb-Pb isochron ages (Walraven et al., 1990). The complicated history of Bushveld Complex crystallization and cooling is not completely understood.

Figure 4: Sedimentary lithologies

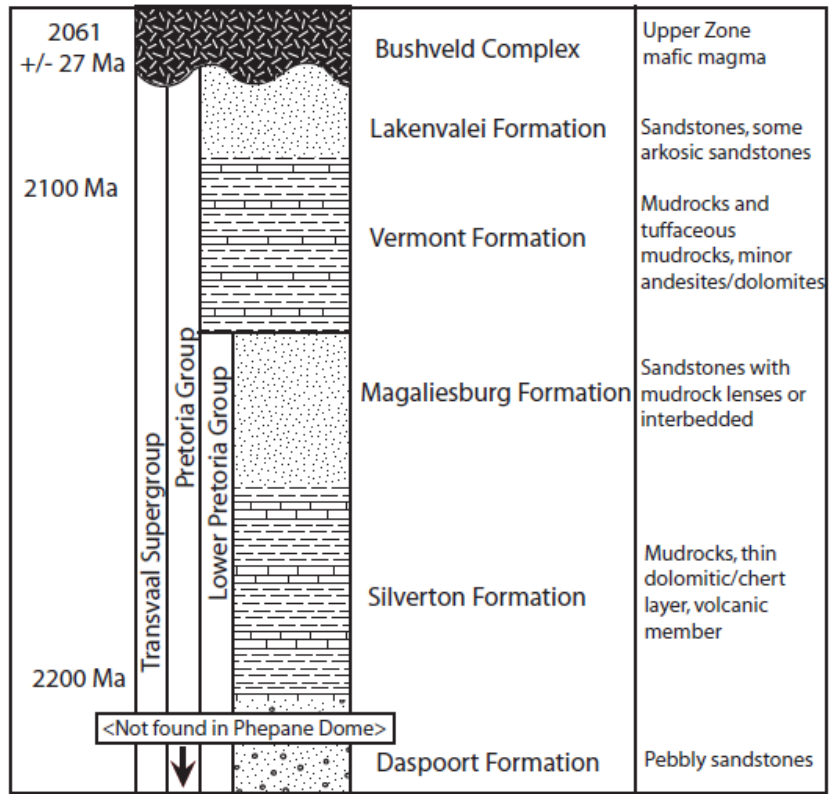


Figure 4: Stratigraphy of the sedimentary rock that the Bushveld intruded (after Eriksson et al. 2001). Rb-Sr whole rock isochrons provide time constraints for both the intrusion age of the Bushveld Complex (2061 ± 27 Ma) and the sedimentation of these layers over the Hekpoort Andesite, which formed at 2224 ± 21 Ma (from Walraven et al., 1990).

3.2: Contact aureole of the Bushveld Complex

The contact metamorphosed rock in the aureole of the Bushveld Complex consists mostly of Pretoria Group sedimentary rock, and only the small Northern extension of the Bushveld Complex intrudes the basement Archean Granite (Clarke et al., 2005). Moving southward in the Eastern Lobe, the aureole is comprised of progressively younger sedimentary rock of the Transvaal Supergroup (Figure 1b). It is thickest in the northern part of the Eastern Lobe, extending 5 km down into the underlying sedimentary rock (Uken and Watkeys, 1997; Clarke et al., 2005). It is thought that the thickness of the aureole directly relates to the occurrence of pericline folding and domes of meta-sedimentary rock within the Eastern Lobe (Clarke et al., 2005). The water released from the sedimentary rocks farthest away in the aureole caused anatexis in the overlying suprasolidus rock closest to the contact (Harris et al., 2003; Johnson et al., 2003). Partial melting of the sedimentary rock combined with the finger-like intrusion style of the Lower Zone created nucleation points for diapirism, e.g. the Phepane Dome, and caused folding of the partially melted sedimentary rocks, e.g. the Steelpoort and Derde Gelid periclinal folds at the Burgersfort Bulge (Clarke et al., 2005) (See Figure 1b).

Located on the edge of the Eastern Lobe, the Burgersfort Bulge is mafic rock of the Bushveld Complex surrounded by domal upper Pretoria Group aureole rocks (Clarke et al., 2005). Harris et al. (2001) describe the mineralogical changes in the meta-sedimentary rocks with distance from the contact at the Burgersfort Bulge. There, the outermost rocks of the aureole are 3.5 km from the contact, and the appearance of biotite and andalusite indicates that a metamorphic temperature of

~500°C was reached. The innermost rocks of the aureole are hornfels containing sillimanite, schist, and migmatite, indicating temperatures greater than 700°C were reached. Within a few meters of the contact, there is evidence that local fluid infiltration caused melting in the Lakenvalei and Magaliesberg Formations at the grain and outcrop scale (Harris et al., 2001). Granite veins and sheets are assumed to be the extracted melt from the sandstone formations, and leucosomes within the migmatized Silverton Formation are shown to be derived from partial melt of the pelitic rock (Johnson et al., 2003). There is also evidence for a large hydrothermal system generated by metamorphic fluids in the aureole at the Burgersfort Bulge, shown by post magmatic hydrothermal veins (Schiffries and Rye, 1990).

3.3: Phepane Dome

Within the Eastern Lobe of the Bushveld Complex, the eroded Phepane Dome forms a topographic bowl-like structure of meta-sedimentary rocks (Figure 5). These rocks have been correlated to the Pretoria Group formations of the Transvaal Supergroup. As the center of the Phepane Dome is approached, the Lakenvalei, Vermont, Magaliesburg, and Silverton formations are found (Johnson et al., 2004). The outer quartzite of the Lakenvalei is directly in contact with the Bushveld Complex igneous rocks. On the western side of the Phepane Dome, the Lakenvalei is in contact with Upper Zone mafic rocks, while the Lakenvalei on the eastern and southern sides is in contact with more felsic rocks, likely of the Lebowa Granite Suite. The timing of the felsic magmatism compared to the mafic magmatism at the Phepane Dome is uncertain. Continuing towards the center of the Phepane Dome, the Vermont Formation consists of meta-pelitic rock with calc-silicate layers. The top of

the Phepane Dome bowl-like ridge is the resistant Magaliesburg quartzite, with the less resistant Silverton pelitic hornfels in the middle of the bowl.

Figure 5: Phepane Dome lithologies

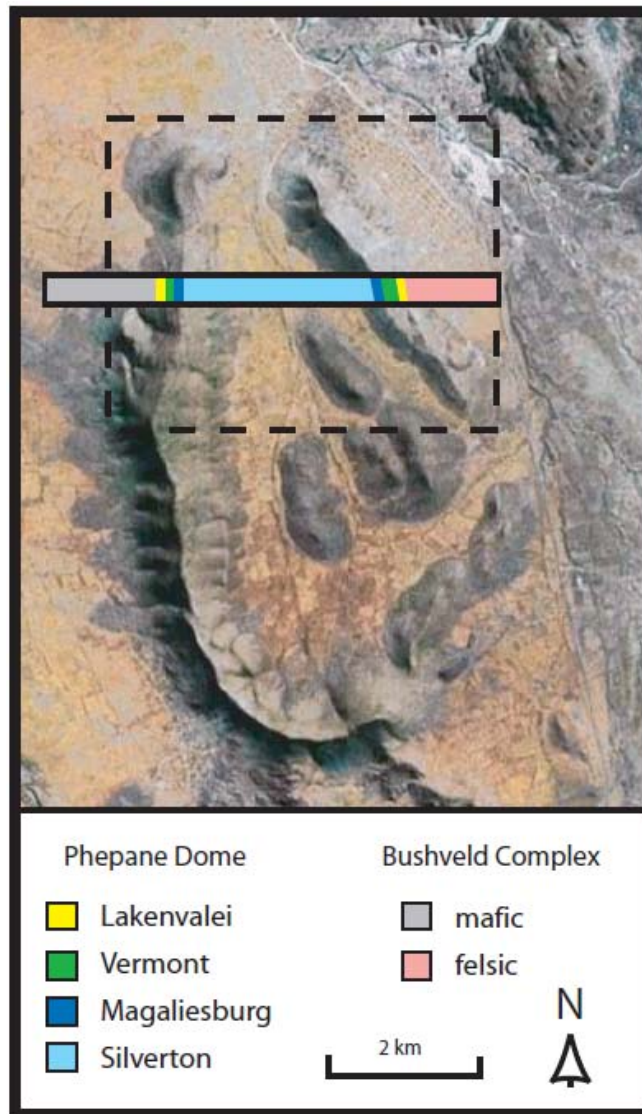


Figure 5: Google Earth image of the Phepane Dome showing topography as well as the rock types found across the Dome.

3.4: Diapirism of the Phepane Dome

Several features of domes in the Eastern Lobe point to formation as diapirs of underlying sedimentary rock that rose into the cooling Bushveld mafic magma (Uken and Watkeys, 1997) (Figure 6). First, gravity data show mafic magma exists beneath the sedimentary rocks of the Marble Hall structure in the southern region of the Eastern Lobe, leading to the conclusion of a possible diapiric origin by Molyneux and Klinkert (1989). Gravity data also suggest the presence of mafic rock under the Malope Dome, indicating that this dome and other domes of the Eastern Lobe such as the Driekop (Derde Gelid) and Phepane also formed as diapirs. This is supported by structural data from the Malope Dome that show an outward dip of 30°, too shallow to indicate a simple dome formation as well as explain the gravity data (Molyneux and Klinkert, 1989). Later authors investigated the structural features of the Phepane Dome, such as close to vertical alignment of curtain folds and lineations in the Phepane core compared to shallow alignments in the outer layers that indicate bulbous formation as a diapir (Uken and Watkeys, 1997; Johnson et al., 2004). In addition, the mineral assemblage of the meta-sedimentary rocks in the core of the Phepane Dome show that partial melting occurred within the dome at temperatures greater than 700°C. The formation of both spinel and cordierite indicate a metamorphic temperature of 720°C, and compositional analysis of the assemblage spinel symplectite, cordierite symplectite, matrix and leucosome cordierite and K-feldspar, biotite, and andalusite resulted in a temperature of $730 \pm 110^\circ\text{C}$ (Johnson et al., 2004). In addition, the preserved spinel and cordierite symplectites replacing andalusite in the core of the Phepane Dome is suggestive of decompression during the

thermal peak as the diapir rose into the Bushveld Complex magma (Johnson et al., 2004).

Figure 6: The Phepane diapir: a 3-D schematic from Gerya et al. (2004)

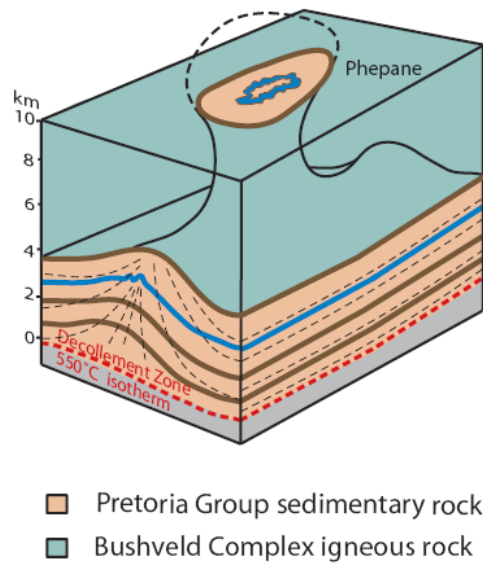


Figure 6: Schematic of the Phepane Dome modified from Gerya et al. (2004). Dashed line at top shows the extent of diapir before surface exposure and erosion. Top of the cube is the level found at the surface today. The Decollement Zone is the hypothesized region of temperature high enough to permit detachment (550°C) and dotted black lines in sedimentary rock show foliation.

Chapter 4: Analytical Methods

4.1: Sampling methodology

Samples were collected in four transects across the contact between the Phepane Dome and the Bushveld Complex; two each on the eastern and western sides (Figure 7). East Transect 06 is located 420 m southeast of East Transect 07, and both Transects cross the Vermont Formation and Lakenvalei quartzite into felsic igneous rock. East Transect 06 is 200 m long with samples taken every 5 to 15 meters, and East Transect 07 is 250 m long with samples every 15 to 40 meters. The western transects cross the Vermont Formation and the Lakenvalei quartzite into mafic igneous rock. The West Large Scale Transect starts with one sample in the Magaliesburg Formation before crossing the Vermont Formation, and has a total distance of 550 m with samples taken every 15 to 20 meters. Approximately 800 m to the north, the West Small Scale Transect is 115 m long with samples collected every 5 to 15 m. The locations of all samples were recorded as GPS coordinates at the time of sampling, while the smaller distances between igneous samples of the East Transect 06 and the West Small Scale Transect were also recorded using measuring tape perpendicular to the quartzite-igneous rock contact.

Samples were also collected from the Pretoria Group in the outer aureole of the Eastern Lobe (Figure 8). Four samples were collected from the Lakenvalei Formation, and one sample was taken from the Vermont Formation. Locations were marked on a geologic map and the GPS coordinates were taken at the sampling site.

Figure 7: Transects taken at the Phepane Dome

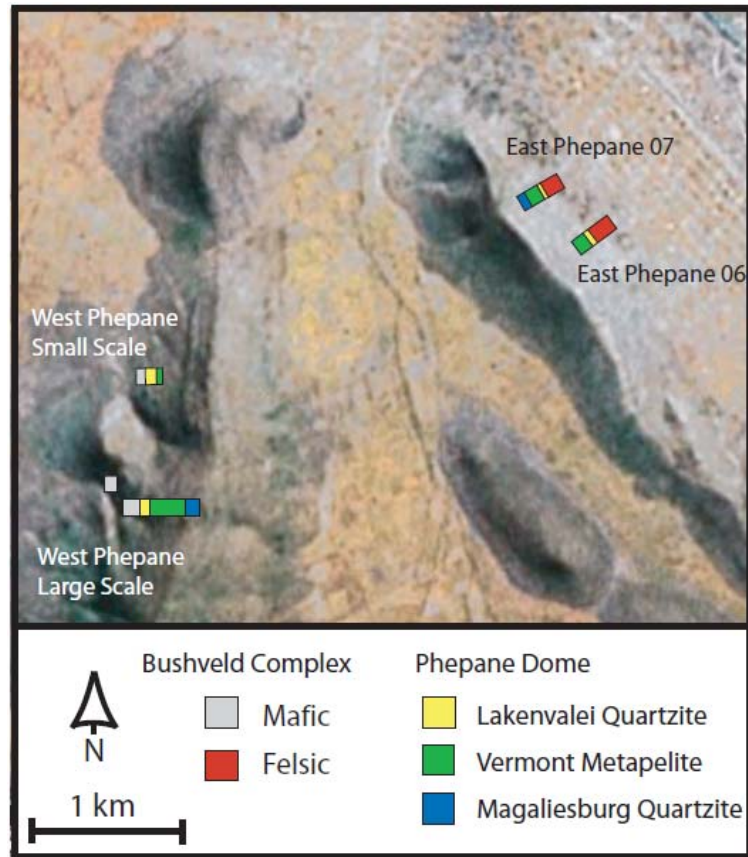


Figure 7: The location of the four sample Transects taken from the East and West sides of the Phepane Dome. On the West, the igneous BC rock is mafic, while on the East, it is felsic igneous rock.

Figure 8: Sedimentary samples from the Transvaal Supergroup

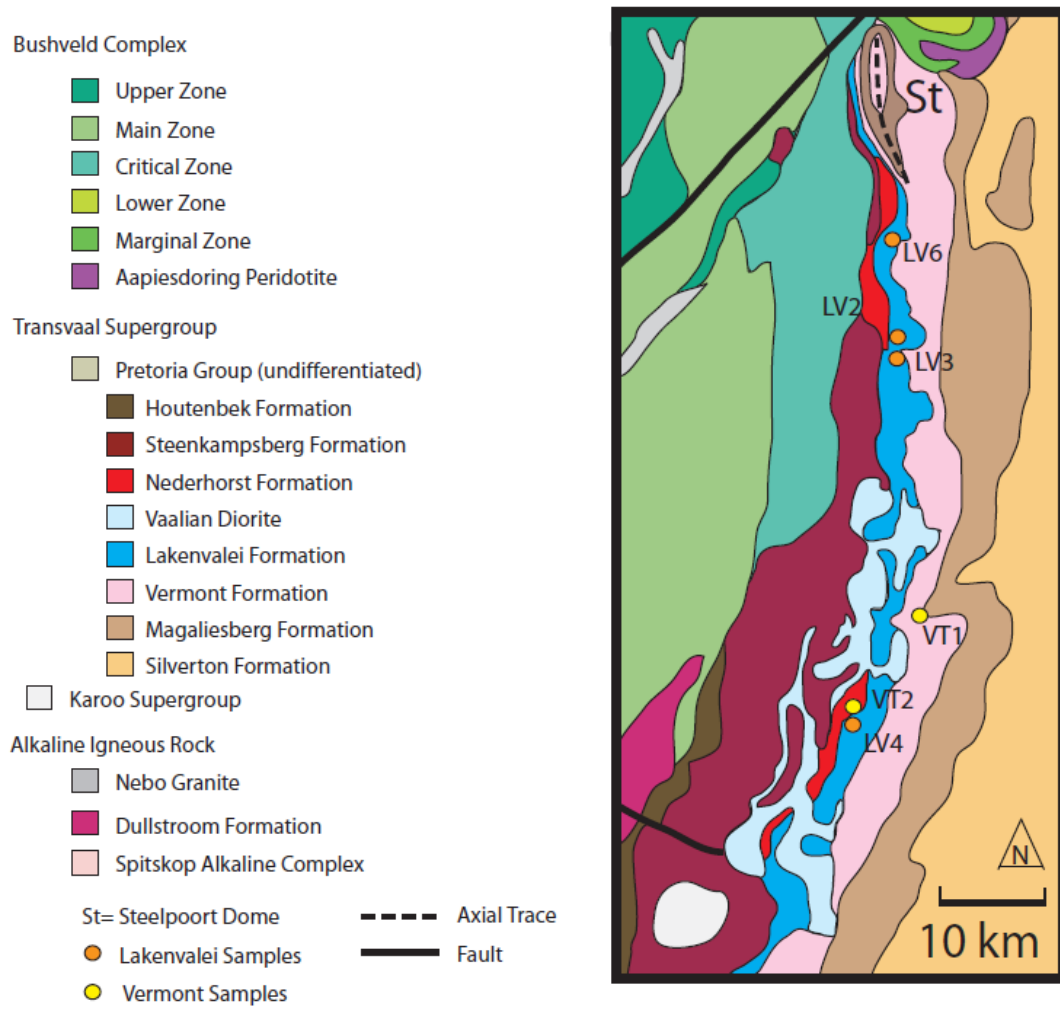


Figure 8: The location of the sedimentary samples taken from the aureole of the Bushveld Complex. Map is a closer view of Figure 1b.

4.2: Sample characterization technique

To determine the mineralogic compositions of these rocks, modal abundances of minerals in representative samples were determined by point counting of thin sections from each rock type on the JXA-8900 Electron Probe Microanalyzer (EPMA) at the University of Maryland. Backscatter electron imaging was used with an energy dispersive X-ray spectrometer to identify each phase. For each sample, ~2000 points were counted in a grid of 0.5 mm spacing. The two sigma percent error

for each phase is calculated using the equation $2\sigma = 2\left(\frac{\sqrt{p(100-p)}}{n}\right)$ from Van der

Plas and Tobi (1965), taking into account the modal abundance of the phase (p; in %) and the total number of points counted (n). While the dominant phases in each rock maintain two sigma errors less than 10%, the error increases for phases that make up less than 15% of the rock. However, it was determined that increasing the amount of points counted would not decrease this error dramatically (Van der Plas and Tobi, 1965).

The modal abundance of minerals from two samples of the Lakenvalei Quartzite were measured; one from the West, mafic side of the Phepane Dome (P07-28) and one from the East, felsic side (P07-19). One felsic sample (P06-2) and two mafic samples (P07-32, P07-6) were also measured. The two mafic samples were selected because they had significantly different grain sizes. The measurement of modal abundances would thus determine if these are different rock types.

Major element compositions of minerals from each rock type were obtained using the JXA-8900 EPMA at the University of Maryland. Feldspar, muscovite,

chlorite, hornblende, clinopyroxene, and orthopyroxene were analyzed using a current of ~20 nA with an accelerating voltage of 15 keV and a 10 μ m spot size. The weight percent of each element was calculated from raw intensities using a ZAF correction. Standards were run at the beginning and end of an analytical day for normalization. The percent error for each element in each phase can be found in Table 2b.

Samples from the Lakenvalei Quartzite were also analyzed by cathodoluminescence (CL) imaging at the Smithsonian Institute Department of Mineral Sciences. The two samples mentioned above (P06-19 and P07-28) as well as samples near and far from the contact were imaged under CL to determine the extent of possible hydrothermal alteration. Using CL reveals annealed micro-cracks and fractures in quartz that are not optically visible (Valley and Graham, 1996). The CL system utilizes an ELM 3R Luminoscope with a 17 kV electron beam and 500 μ A current, connected to an optical microscope. Pictures were taken using the program MagnaFIRE with an Olympus camera that allows for an extended exposure time to acquire the low luminescence of quartz.

4.3: Dihedral angle analyses

The measurement of dihedral angles in thin sections from all transects was used for recognizing the former presence of melt in the rocks of the Phepane Dome. This method was used by Harris et al. (2003) in the outer aureole of the Bushveld Complex Eastern Lobe. Harris et al. (2003) measured more than 25 dihedral angles at quartz-quartz-feldspar grain junctions in thin sections of the Lakenvalei and Magaliesburg Quartzites. Feldspar angles of 105-110 $^{\circ}$ are representative of solid state equilibrium between phases (Vernon, 1968), while angles less than this are

associated with partial melt and subsequent crystallization of the feldspar between two solid quartz grains (Holness, 1998) (see Figure 9). While the optical measurement of thin sections only records 2-D angles, and not the true 3-D dihedral angle, the median of >25 measured 2-D angles in one thin section is within 1° of the 3-D angle. However, if more than one peak is observed, then there is more than one 3-D dihedral angle in the rock (Harris et al., 2003). To verify this accuracy, the 3-D dihedral angles of two samples were measured using a universal stage and compared to the results from the 2-D measurements.

Harris et al. (2003) observed a two peaked distribution in quartzite thin sections: one peak of angles in the ~90° range, and one peak of angles in the 105-110° range. They concluded that this bimodal distribution of angles they observed corresponds to a solid state equilibrium dihedral angle and a lower, melted feldspar dihedral angle. This represents heterogeneous melting of feldspars at the grain scale in their rocks. This method was applied to six quartzites near the contact of the Bushveld Complex to determine the extent of melting.

Figure 9: Example dihedral angles

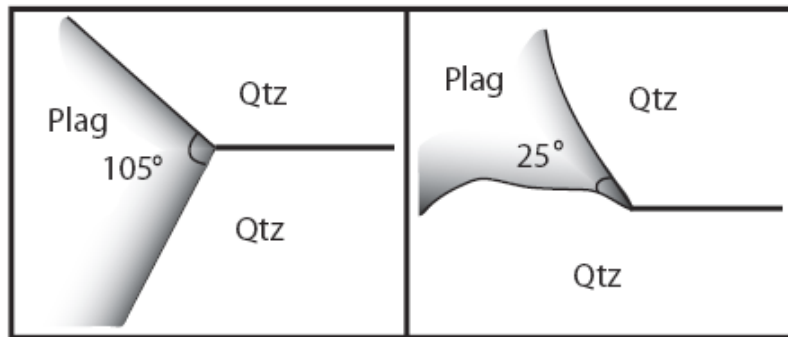


Figure 9: Example dihedral angles. **(left)** greater angle solid feldspar between two solid quartz grains associated with solid state equilibrium **(right)** cusped low angle melted feldspar between two solid quartz grains associated with partial melt.

4.4: Oxygen isotope measurement technique

Samples from two transects were measured for oxygen isotopic composition using quartz and feldspar mineral separates and whole rock powders. A binocular microscope was used to pick quartz from each felsic and quartzite sample and plagioclase from each mafic sample. The quartz samples were rinsed in concentrated HF for 30 seconds to ensure purity. The feldspar grains were crushed to powder and analyzed using X-ray diffraction at the University of Maryland X-ray Crystallographic Center to ensure purity. Samples were then measured for oxygen isotopic composition at the University of Wisconsin-Madison Stable Isotope Laboratory. For each sample, between 1 and 2 mg of material was converted to CO₂ using laser fluorination for analysis on a dual inlet five collector Finnigan MAT 251 mass spectrometer. Results are reported as $\delta^{18}\text{O}$ relative to SMOW.

$$\delta^{18}O = \left(\frac{\left(\frac{^{18}O}{^{16}O} \right)_{sample}}{\left(\frac{^{18}O}{^{16}O} \right)_{SMOW}} - 1 \right) \times 1000 \quad (6)$$

The external error is quantified by measurement of the Gore Mountain Garnet standard (UWG-2) at the beginning of each set of analyses. Sample results are normalized to the accepted value for UWG-2 ($\delta^{18}O = 5.8\%$, Valley et al., 1995). Five analyses of UWG-2 before the measurement of quartz mineral separates gave a value of $5.6 \pm 0.16\%$, and seven analyses of UWG-2 before the measurement of two plagioclase powders (P07-32 and P07-34) and all whole rock powders gave $5.8 \pm 0.10\%$ (errors are 2σ). The other plagioclase powders (P07-31 and P07-33) were analyzed after seven analyses of UWG-2 giving a $\delta^{18}O$ of $5.7 \pm 0.10\%$.

4.5: Lithium isotopic and compositional measurement technique

Lithium concentrations and isotopic compositions of each sample were measured using whole rock powders. Each sample was cut to find the freshest piece, and then $\sim 1 \text{ cm}^3$ was powdered in the Mixer Mill 8000 using a tungsten carbide container in the Geochemistry Labs at the University of Maryland. In 15 mL teflon beakers, these powders were dissolved using step additions of concentrated acid with drying down steps in between. Dissolution and dry-down occur at hot plate temperatures of less than 100°C . Hydrofluoric acid, nitric acid, an aqua-regia step using nitric and hydrochloric acid, and hydrochloric acid are added over five days. Using a method similar to Moriguti and Nakamura (1998), the resultant solution is passed through three cation exchange columns in order to separate Li for analysis. Finally, the samples were analyzed using the Nu Plasma Multi Collector-Inductively

Coupled Plasma-Mass Spectrometer (MC-ICP-MS) at the University of Maryland according to the method described in Teng et al. (2004). Results are reported as $\delta^7\text{Li}$ relative to the standard L-SVEC.

$$\delta^7\text{Li} = \left(\frac{\left(\frac{{}^7\text{Li}}{{}^6\text{Li}} \right)_{\text{sample}}}{\left(\frac{{}^7\text{Li}}{{}^6\text{Li}} \right)_{\text{LSVEC}}} - 1 \right) \times 1000 \quad (5)$$

Long term reproducibility of Li isotopic measurements is within $\pm 1\%$ (2σ) as determined by Teng et al. (2004), and verified through analysis of Li standards UMD-1 (+54.7‰) and IRMM-016 (-0.1‰) during each analytical run. The average $\delta^7\text{Li}$ value for all measurements of UMD-1 is $54.6 \pm 0.9\%$ and for IRMM-016 it is $0.3 \pm 1.4\%$. Measured ${}^7\text{Li}$ voltages for samples are compared to the 50 ppb L-SVEC ${}^7\text{Li}$ voltage to determine the concentration of Li in solution and then adjusted for the mass of each sample powder dissolved. This results in values for Li concentration with 2σ uncertainties of $< \pm 10\%$ (Teng et al., 2006b). In addition, two basalt standards (BHV0-1 and BHV0-2) were dissolved and processed through the cation exchange columns. The reported $\delta^7\text{Li}$ of value for BHV0-1 is 4.5‰ with a Li concentration of 4.9 ppm (Govindaraju, 1995). For eight MC-ICP-MS analyses of BHV0-2 by Jeffcoate et al. (2004), an average $\delta^7\text{Li}$ value of $4.7 \pm 0.22\%$ and an average concentration of 4.8 ± 0.25 ppm were reported. Measurements of these standards resulted in $\delta^7\text{Li}$ values of 3.6‰ and 4.0‰ and Li concentrations of 4.4 ppm and 5.7 ppm for BHV0-1 and BHV0-2 respectively.

To measure the Li concentration of each mineral within a rock, laser ablation of thin sections from the Lakenvalei quartzite, felsic Bushveld and mafic Bushveld

was employed. The same minerals in samples measured by EPMA were ablated with a Nd:YAG laser connected to an Element 2 Single Collector-ICP-MS at the University of Maryland. Each mineral was ablated with a 40 to 175 μm spot size, depending on the size of the mineral and the amount of Li in the mineral. Where possible, multiple spots in a mineral were measured. Ablation occurred for 90 seconds after an initial 30 seconds of background measurement. To correct for ablation yield, the Li concentrations were normalized to an internal standard ^{29}Si that was previously measured by EPMA as SiO_2 . The Li concentrations were calculated from two analyses of an external standard NIST610 ($\text{SiO}_2 = 70 \text{ wt.}\%$) before and two more analyses of NIST610 after 18 sample spots using the program LAMTRACE. The analysis of standard BCR-2g (see Table 5b for values) before sample measurement was used to assess accuracy, and the percent error was taken from the standard deviation of the four NIST610 standard analyses (2σ of 0.3% to 1.4% for all analyses except sample P06-14: 2.3%).

Chapter 5: Results

5.1: Petrology

Modal abundances of the four different rock localities (East Phepane Lakenvalei Quartzite, West Phepane Lakenvalei Quartzite, Felsic Bushveld Complex, Mafic Bushveld Complex) are presented in Table 1. The two quartzite samples from the East and West side of the Phepane Dome show similar proportions with $83.0 \pm 1.62\%$ quartz, $8.97 \pm 1.23\%$ K-feldspar, and $5.30 \pm 0.97\%$ plagioclase on the East side, and $87.3 \pm 1.44\%$ quartz, $8.89 \pm 1.23\%$ K-feldspar, and $3.39 \pm 0.78\%$ plagioclase on the West side. There is more muscovite and chlorite on the East side, while the West side contains a small amount of calcite ($0.09 \pm 0.13\%$) not found on the East side.

The Bushveld Complex felsic igneous rock on the East side of the Phepane Dome is granite, with $20.9 \pm 1.74\%$ quartz, $31.8 \pm 2.00\%$ K-feldspar, $32.2 \pm 2.00\%$ plagioclase, and $13.3 \pm 1.46\%$ hornblende. There is a small amount of biotite ($1.43 \pm 0.51\%$) and trace amounts of Fe-Ti oxides and phosphates. For the mafic rock on the West side of the Phepane Dome, the volume percentages of minerals in two samples were measured. Both samples were determined to be gabbro, mostly comprised of plagioclase (sample P07-6: $64.54 \pm 0.79\%$ plag and sample P07-32: $78.73 \pm 0.35\%$ plag). The latter sample (P07-32) contains more felsic minerals (specifically $8.55 \pm 1.19\%$ quartz compared to the $0.56 \pm 0.31\%$ quartz in P07-6), and thus was determined to be a quartz gabbro. This sample also contains less hornblende and clinopyroxene, while the other sample contains orthopyroxene not found in P07-32. Both samples are approximately 20 m from the contact in their respective transects.

The major element abundances in the dominant minerals of each rock type are shown in Table 2a. On the East side of the Phepane Dome, the Lakenvalei Quartzite is comprised of K-feldspar, albite, muscovite, and Fe-rich chlorite ($Mg/(Mg+Fe)=0.40$). The felsic Bushveld Complex rock has perthitic K-feldspar, oligoclase (Ab87) with a small amount of albite, and Ca and Fe-rich hornblende ($Mg/(Mg+Fe)=0.03$). On the West side of the Phepane Dome, the Lakenvalei Quartzite is similar to the East side but contains Mg-rich chlorite ($Mg/(Mg+Fe)=0.60$). Similarly, the hornblende differs from the felsic rock because it is Ca and Mg-rich ($Mg/(Mg+Fe)=0.68$). The pyroxenes are enstatite (En61) and Mg-rich augite ($Mg/(Mg+Fe)=0.72$). The plagioclase of the mafic Bushveld rock is mostly labradorite (An67), with trace amounts of K-feldspar and albite in the more felsic sample (P07-32).

Table 1: Mineral modes of representative rock types

Sample	P06-19	P07-28	P06-2	P07-32	P07-6
Type	Lakenvalei Quartzite	Lakenvalei Quartzite	Bushveld Granite	Bushveld Gabbro	Bushveld Gabbro
	East	West	East	West	West
Quartz	83.0**	87.3	20.9	8.55	0.56
K-feldspar	8.97	8.89	31.8	1.64	0.17
Plagioclase	5.30	3.39	32.2	78.7	64.5
Hornblende	0	0	13.3	7.20	23.9
Clinopyroxene	0	0	0	0.68	3.77
Orthopyroxene	0	0	0	0	5.57
Muscovite	2.56	0.38	0	0.05	0.17
Biotite	0	0	1.4	tr	0
Chlorite	0.19	0.05	0	2.00	1.16
Calcite	0	0.09	0	0.59	0
Zircon	tr*	tr	tr	tr	0
Apatite	tr	tr	0.05	0.55	0
Monazite	tr	0	0.05	0	0
Ilmenite	0	0	0.05	tr	0.13
Magnetite	0	0	0.14	0	tr
Titanite	0	0	0	tr	0
Rutile	0	tr	tr	0	0
Halite	tr	tr	tr	0	0
Sylvite	tr	tr	tr	0	0
Total points	2152	2126	2174	2200	2335

* tr= trace

** Numbers are volume percentages

Table 2a: Major element compositions (wt%)

Phase Sample	K-Feldspar														Plagioclase	
	†7-28	7-28	7-28	7-28	7-28	6-19	6-19	6-2*	6-2*	6-2	6-2	6-14	6-14	7-32	7-28	7-28
SiO ₂	63.59	64.01	63.50	63.59	63.16	64.07	63.52	64.88	64.75	63.62	63.23	64.32	64.25	63.13	66.80	67.76
TiO ₂	0.01	0.01	0	0.01	0	0	0	0.01	0.01	0.01	0	0	0	0	0	0
Al ₂ O ₃	18.88	19.10	18.94	19.02	18.24	18.80	18.92	19.66	19.06	18.49	18.39	18.22	18.36	18.05	19.97	20.07
FeO	0	0.03	0	0	0	0	0.41	0.07	0.06	0.06	0.08	0.07	0.07	0.04	0	0.02
MnO	0.01	0	0	0.01	0.03	0	0.01	0.02	0.03	0	0.01	0.01	0	0.04	0.02	0.01
MgO	0.01	0	0.01	0.01	0	0	0.16	0.01	0.01	0	0	0	0.01	0	0.02	0.02
CaO	0	0.03	0.00	0.02	0.03	0	0.00	0.21	0.16	0.02	0.04	0.04	0.06	0.96	0.42	0.09
Na ₂ O	0.17	0.18	0.91	0.32	0.52	0.19	0.20	5.56	5.01	0.33	1.17	0.88	0.86	0.26	11.41	11.82
K ₂ O	16.06	16.32	15.47	16.07	16.38	16.42	15.99	8.45	9.38	15.81	15.40	16.38	16.36	16.37	0.04	0.06
Total	98.73	99.67	98.83	99.04	98.37	99.49	99.22	98.87	98.45	98.33	98.32	99.92	99.96	98.84	98.68	99.84
X _{Ab}	0.016	0.017	0.082	0.015	0.056	0.017	0.018	0.489	0.444	0.031	0.103	0.075	0.074	0.022	0.978	0.993
X _{An}	0.001	0.001	0	0.001	0.009	0	0	0.010	0.008	0.001	0.002	0.002	0.003	0.046	0.020	0.004
X _{Or}	0.984	0.982	0.918	0.984	0.952	0.983	0.982	0.501	0.548	0.968	0.895	0.923	0.924	0.931	0.003	0.003

Phase Sample	Plagioclase														
	6-19	6-19	6-19	6-2	6-2	6-2	6-14	6-14	7-32	7-32	7-32	7-32	7-32	7-6	7-6
SiO ₂	67.50	68.37	67.84	66.00	65.33	62.98	66.13	64.46	51.80	51.55	50.81	50.57	52.53	49.52	50.15
TiO ₂	0	0	0	0	0.01	0.01	0	0	0	0.01	0	0	0	0	0
Al ₂ O ₃	20.15	20.27	20.28	20.79	21.61	22.74	20.71	21.56	31.17	31.46	30.86	30.67	29.34	31.95	31.59
FeO	0.02	0.03	0.01	0.09	0.07	0.20	0.11	0.11	0.08	0.11	0.08	0.01	0.07	0.08	0.06
MnO	0.02	0.02	0.01	0.01	0	0.01	0.02	0	0	0.01	0	0	0.02	0.01	0
MgO	0.02	0.02	0.02	0	0.02	0.01	0.01	0.01	0.02	0.04	0.01	0.04	0	0	0
CaO	0.14	0.14	0.07	1.97	1.86	2.52	1.79	2.66	13.27	13.58	14.60	13.27	12.95	16.03	15.50
Na ₂ O	11.69	11.84	11.88	10.36	10.31	9.32	10.67	9.81	3.83	3.69	3.73	4.18	3.92	3.03	3.33
K ₂ O	0.09	0.08	0.06	0.51	0.23	1.10	0.30	0.51	0.11	0.20	0.10	0.08	1.39	0.10	0.09
Total	99.63	100.8	100.2	99.71	99.44	98.90	99.71	99.14	100.3	100.6	100.2	98.81	100.2	100.7	100.7
X _{Ab}	0.989	0.989	0.994	0.879	0.897	0.815	0.900	0.844	0.341	0.326	0.315	0.361	0.327	0.278	0.254
X _{An}	0.007	0.007	0.003	0.092	0.090	0.122	0.083	0.127	0.651	0.662	0.680	0.634	0.596	0.717	0.741
X _{Or}	0.005	0.004	0.003	0.028	0.013	0.063	0.016	0.029	0.008	0.011	0.005	0.004	0.076	0.005	0.005

Table 2a (continued): major element compositions (wt%)

Phase Chlorite						Phase Muscovite						
Sample	7-28	6-19	6-19	6-19	7-32	Sample	7-28	7-28	7-28	6-19	6-19	6-19
SiO ₂	26.37	25.16	28.15	28.38	27.33	SiO ₂	45.10	45.77	46.14	46.61	47.09	47.15
TiO ₂	0.04	0.92	0.00	0.00	0.03	TiO ₂	0.14	0.04	0.03	0.06	0.16	0.03
Al ₂ O ₃	21.45	22.59	22.10	21.50	20.83	Al ₂ O ₃	34.94	38.07	36.67	35.42	35.07	35.41
FeO	20.84	33.64	23.23	23.74	18.28	FeO	1.23	0.35	1.29	1.42	1.66	1.57
MnO	0.27	0.23	0.37	0.46	0.31	MnO	0.01	0.01	0.01	0.03	0.01	0.01
MgO	17.59	8.27	9.74	11.24	20.15	MgO	0.83	0.03	0.05	1.00	1.16	0.88
CaO	0.01	0.04	0.10	0.08	0.02	CaO	0.01	0.02	0.01	0.04	0.03	0.01
Na ₂ O	0.02	0.01	0.02	0.04	0.03	Na ₂ O	0.35	0.23	0.27	0.49	0.43	0.37
K ₂ O	0.03	0.11	0.20	0.64	0.01	K ₂ O	10.86	10.38	10.82	9.85	10.12	10.72
Total	86.63	90.98	83.90	86.07	86.99	Total	93.45	94.90	95.29	94.91	95.72	96.15
Mg												
(Mg+Fe)	0.601	0.305	0.428	0.458	0.663							

Phase Hornblende (Hbl) and Pyroxenes (Opx, Cpx)															
Sample	6-2	6-2	6-2	6-14	6-14	7-32	7-32	7-32	7-32	7-6	7-6	7-6	7-6	7-6	
	Hbl	Opx	Opx	Cpx											
SiO ₂	39.62	38.81	39.12	38.58	39.30	51.74	52.14	51.58	51.14	51.05	52.01	52.38	51.82	54.58	51.88
TiO ₂	1.76	1.82	1.81	2.05	1.85	0.76	0.65	0.54	0.70	0.67	0.47	0.40	0.18	0.03	0.38
Al ₂ O ₃	9.11	9.23	9.50	9.34	9.28	4.60	4.36	3.98	4.55	4.68	3.94	3.54	1.24	0.52	1.99
FeO	34.29	33.96	34.19	33.83	34.21	12.79	13.07	12.93	13.18	13.07	13.10	12.87	24.02	22.09	10.07
MnO	0.49	0.49	0.56	0.48	0.48	0.21	0.25	0.25	0.24	0.20	0.36	0.22	0.50	0.55	0.27
MgO	0.48	0.54	0.47	0.47	0.50	15.85	16.15	15.10	14.86	15.19	15.15	15.52	21.81	19.35	14.50
CaO	10.06	10.05	10.10	10.68	10.22	11.83	11.63	12.29	11.92	11.71	11.45	11.66	1.58	1.41	20.40
Na ₂ O	2.14	2.10	2.13	2.18	2.15	0.53	0.52	0.41	0.56	0.58	0.43	0.44	0.02	0.04	0.29
K ₂ O	1.43	1.49	1.68	1.57	1.51	0.29	0.27	0.26	0.29	0.26	0.20	0.17	0.01	0.01	0.08
Total	99.38	98.50	99.57	99.18	99.51	98.59	99.04	97.34	97.45	97.41	97.12	97.21	101.19	98.57	99.85
Mg															
(Mg+Fe)	0.025	0.028	0.024	0.024	0.026	0.688	0.688	0.673	0.670	0.674	0.673	0.683	0.630	0.618	0.720

Table 2b: Percent error of weight %

Phase	Kfs	Ab	Pl	Chl	Ms	Hbl	Opx	Cpx
SiO ₂	0.29%	0.29%	0.34%	0.49%	0.37%	0.39%	0.33%	0.33%
TiO ₂	-	-	-	-	-	0.94%	4.90%	2.20%
Al ₂ O ₃	0.38%	0.36%	0.29%	0.55%	0.28%	0.61%	2.70%	1.20%
FeO	30.00%	70.00%	50.00%	0.73%	4.32%	0.78%	1.00%	1.40%
MnO	-	-	-	8.90%	80.00%	6.70%	6.80%	12.00%
MgO	-	-	-	0.95%	2.16%	3.80%	0.43%	0.52%
CaO	92.00%	0.95%	0.33%	10.00%	23.00%	0.39%	1.10%	0.30%
Na ₂ O	9.00%	0.71%	1.30%	35.00%	3.25%	2.00%	-	5.00%
K ₂ O	0.31%	2.15%	7.60%	3.30%	0.42%	1.00%	-	5.90%

Table 2: (a) Major element compositions in oxide weight percent. Mineral abbreviations are after Kretz (1983). † All samples start with P0. * Measured perthitic feldspar as an average of 5 points taken across the grain. **(b)** The representative percent error of each oxide for each mineral phase calculated from counting statistics.

5.2: Evidence for melt

Thin section analysis of six Lakenvalei quartzites shows that melt was present during the formation of the Phepane diapir. Thin sections from both sides of the Phepane Dome exhibit cusped feldspar grains that Harris et al. (2003) equated to feldspar as a melt phase between two solid quartz grains, as well as equant grains associated with unmelted feldspar (Figure 10). This is reflected in the measured quartz-quartz-feldspar dihedral angles (Figure 11). Two thin sections (P06-18 and P07-26) show two obvious peaks in the angle measurements, with a peak in the lower range at $\sim 50^\circ$ indicative of partial melting and a peak at $\sim 105^\circ$ indicative of solid state equilibrium. The dihedral angles measured in thin sections from samples closest to the contact (P06-15 and P07-30) are more scattered. However, the large range in angles does not appear to center around $105\text{-}110^\circ$, indicating that these samples have a population of lower dihedral angles and must have experienced partial melting. This is true for sample P06-19 as well, which was measured using both the 2-D angle method and the 3-D angle universal stage method. The results of measurements with the universal stage revealed an abundance of low angles with a peak at $\sim 40^\circ$, indicating that the 2-D measurement method has spread these angles over $20\text{-}90^\circ$. In addition, measurements of angles in P06-18 using both the 2-D method and the universal stage show the same two-peaked distribution (Figure 11). Thus, the 2-D method is suitable for discerning whether there is a population of cusped lower angles and/or a population of high angles indicative of unmelted feldspars. This is the case for the sample farthest from the contact (P07-1; 46m) that appears to have a peak only in the $105\text{-}110^\circ$ range. This sample has a small amount

of cusped grains, seen as the population in the 30-50° range. These cusped grains indicate that this sample experienced partial melting, likely to a lesser extent than the other samples. Thus, the meta-sedimentary rocks of the Phepane diapir were partially melted at the grain-scale during formation.

Figure 10: Dihedral angles in thin section

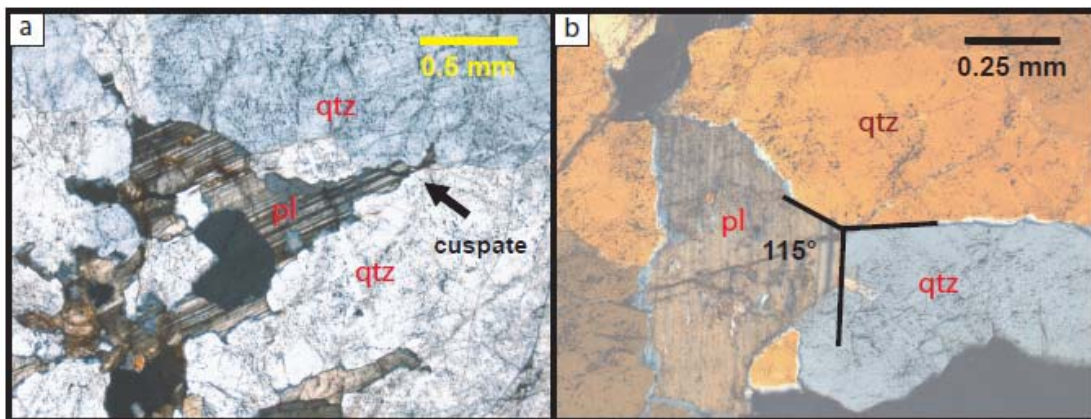


Figure 10: (left) Photo in crossed polarized light of melt texture with cusped plagioclase and (right) photo of an equilibrium plagioclase with a dihedral angle of 115 degrees. Note: the orange interference colors of both quartz and plagioclase are the result of a thicker thin section. qtz= quartz, pl= plagioclase

Figure 11: Histograms of dihedral angle measurements

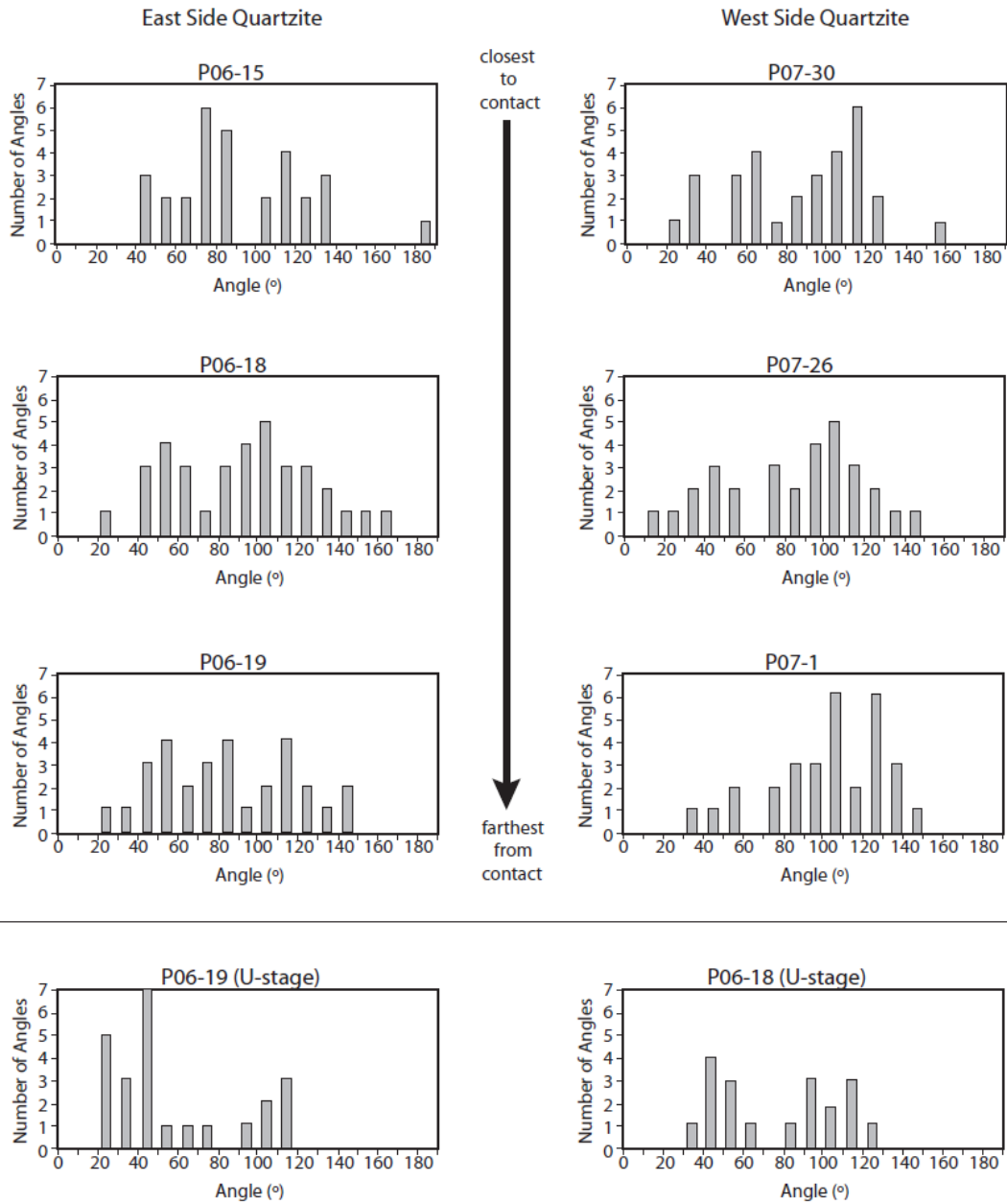


Figure 11: Histograms of dihedral angle measurements. A bimodal distribution (**top**) 2-D angle measurements for samples from the East (left) and West (right) side of the Phepane Dome. The samples in the top row (P05-15 and P07-30) are within 2 m of the contact, the next two (P06-18 and P07-26) are ~10 m from the contact, and the third row has a sample at 13 m from the contact (P06-19) and 50 m from the contact (P07-1). (**bottom**) 3-D angle measurements using a universal stage.

5.3: Evidence for aqueous fluid

In addition to partial melting, there is also evidence that these rocks experienced a fluid infiltration stage. A large amount of fluid inclusions can be seen in the quartz and feldspar grains of the Lakenvalei. Thin section analysis of sample P06-16 shows that these inclusions concentrate along fractures that cut across multiple quartz grains. This indicates that the fluid inclusions are secondary to crystal growth, forming due to the presence of fluid at the time of fracture (Roedder, 1984). Figures 12a and 12b show the similar orientation of fractures in the quartzite, including one fracture that cuts three quartz grains. At a higher magnification, fluid inclusions are seen along the fracture that cuts across a quartz grain boundary (Figure 12c and 12d). This evidence for aqueous fluid is supported by the slight alteration of the mafic Bushveld rock and the Lakenvalei Quartzite. Thin sections from the mafic igneous rock show varying degrees of slight alteration of plagioclase to sericite and pyroxene to fine-grained chlorite, and biotite replaced by chlorite is visible in the Lakenvalei.

To determine the relative timing and extent of crystallization and fluid infiltration, cathodoluminescence (CL) of quartz can be used. Differences in luminosity and CL color have been ascribed to recrystallization events such as low temperature quartz precipitation or cementation, metamorphism, and fluid infiltration. This is because recrystallization changes the trace element abundance and defects in the crystal lattice of the quartz, two properties thought to be activators of luminescence (Götze et al., 2001). Thus, examination under CL can show if the quartz from the Lakenvalei quartzite in the Phepane Dome has retained a sedimentary

signature, has been partially or completely recrystallized due to the contact metamorphism, or if there has been extensive recrystallization due to a late stage fluid infiltration.

Figure 12: Fluid inclusions in quartz

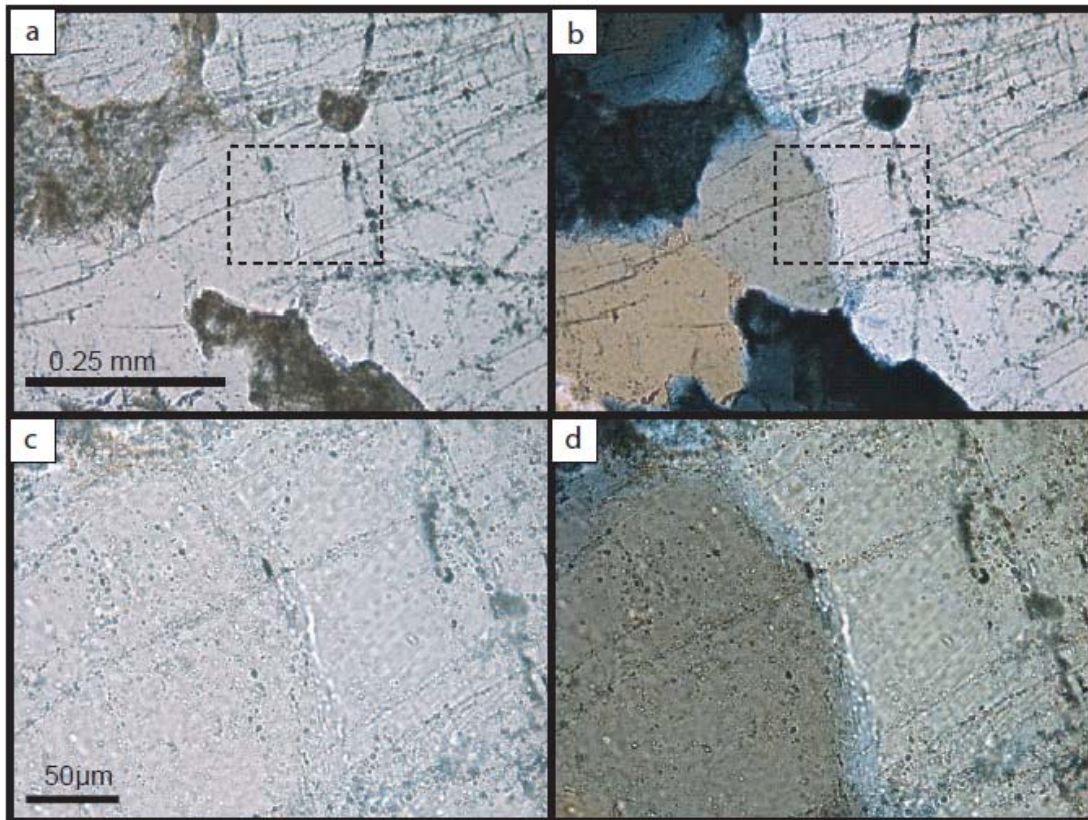


Figure 12: Fluid inclusions in the Lakenvalei quartzite P06-16. Left is plane polarized light (PPL) and right is cross polarized light (XPL). **(a)** 20x magnification showing fractures cutting across quartz grains. **(b)** XPL of same field of view as (a). **(c)** 50x mag. showing inclusions along a fracture that cross cuts two quartz grains. **(d)** XPL of same field of view as (c).

To identify the sedimentary signature of the Lakevlei protoliths, sample LV4 from the Lakenvlei sandstone was imaged (Figure 13a). This sample has mostly non-luminescing detrital quartz grains, with occasional heterogeneous blue luminescing detrital grains. Bright red luminescing authigenic quartz is seen between detrital grains and along some grain boundaries, and a non-luminescent cement is visible. The mixture of detrital grains and low or red luminescent cement is common for sedimentary rocks (Götze et al., 2001). In contrast, quartz grains from the Lakenvlei Quartzite generally luminesce bright blue (Figure 13, 14, 15: regions labeled B), showing no evidence of the sedimentary signature. Bright blue luminescence is thought to be related to recrystallization at high temperature. Sprunt et al. (1978) found that quartz from contact metamorphic rocks in the Bergell Alps luminesced the brightest blue of metamorphic rocks, while quartz in lower temperature greenschist and amphibolite metamorphic rocks had significant red luminescence. They also determined that metamorphism homogenizes the luminescence. This agrees with a study by Boggs et al. (2002) that found volcanic, plutonic, and contact metamorphic quartz all luminesced bright blue and associated this with crystallization or recrystallization at high temperature. More recent studies (e.g., Muller et al., 2003; Rusk et al., 2008) have examined the trace element abundance in quartz compared to CL zoning, hypothesizing that Ti is responsible for the bright blue luminescence, since Ti preferentially substitutes for Si in quartz at higher temperatures and Ti is abundant in magmatic settings. It is reasonable that the Lakenvlei quartzite would luminesce bright blue, since temperatures high enough for partial melting were reached during Bushveld Complex intrusion and diapirism. The

lack of a preserved sedimentary signature suggests complete recrystallization and homogenization of the quartz during metamorphism.

The textures of luminescence within a sample can reveal growth or late stage fluid infiltration events not visible with optical microscopy (e.g., Valley and Graham, 1996; Penniston-Dorland, 2001). Five textures are identified in Lakenvalei samples: the bright blue luminescence described above, a darker luminescent blue at random orientations within grains, a similar darker blue luminescence along grain boundaries, brown to non-luminescent quartz along regions with high fluid inclusion density, and non-luminescent quartz along visible fractures. The bright blue luminescence has already been interpreted as recrystallization at high temperature during contact metamorphism, and is found mostly in the interiors of quartz grains. The darker blue luminescence seen within grains usually occurs in random orientations, forming multiple regions of smaller bright blue luminescence within one quartz grain (Figure 15). This texture is obvious in sample P07-14 (Figure 15c), 10 m from the contact on the West side of the Phepane Dome. As seen in Figure 15c, fluid inclusions follow the curved region of darker luminescent blue that surrounds a region of bright blue. Since this assemblage of fluid inclusions is not linear, it is unlikely that the fluid inclusions formed in response to a fracture-healing event. Instead, the inclusions were likely a pore fluid that was trapped, indicating that the bright blue is an original quartz grain and the darker blue is an overgrowth during recrystallization in the presence of fluid.

The third texture is a similar darker blue luminescence along grain boundaries of bright blue luminescent quartz. This is especially visible in sample P06-19, 13 m

from the contact in the East Phepane (Figure 14), but also appears in sample P07-14 (Figure 15c) of the West Phepane. Because of the similarity of this feature to the darker luminescence found within quartz grains of P07-14, it is likely that these are related overgrowth events. In P06-19 (Figure 14), the darker blue luminescence comprises an entire quartz grain. This is much more common closer to the contact in the East Phepane, where the bright blue luminescence is reduced to small shapes surrounded by expanses of the darker blue luminescence (e.g., samples P06-16: Figure 13c, 13g; P06-15: Figure 15a). Because the fluid inclusion density also increases in samples closer to the contact, it is likely that the darker luminescence is related to recrystallization at grain edges in the presence of much more fluid than in samples that show mostly the bright blue luminescence with darker blue luminescence along grain boundaries.

The non-luminescent quartz has been recognized in association with two separate textures: associated with abundant fluid inclusions, and along fractures with little or no fluid inclusions. The first texture appears in samples from both sides of the Phepane Dome (Figure 13c and Figure 15 all). It occurs within grains, at grain boundaries or even linearly following a fracture. Most appearances are small relative to the grain or fractures that they coincide with. The second non-luminescent texture is only found along fractures on the East side (Figure 13e, 13g). In P06-19, the non-luminescent quartz appears along a fracture that cuts both feldspars and quartz. In P06-16, the non-luminescent quartz appears as fluid inclusion-free healed fracture. These fractures must have occurred late, because they are associated with visible

fracturing and have relatively few or no fluid inclusions. However, there are few appearances of this texture.

The colors and textures of CL are indicative of three different stages of metamorphism and fluid infiltration. The first is related to the bright blue luminescence and probably occurred as the Lakenvalei sandstone partially melted and metamorphosed. The second stage is the darker blue luminescence that was shown to be a recrystallization of smaller quartz grains into the large grains visible today. This is likely related to contact metamorphism as well, and could have occurred as a fluid was released during crystallization of the magmas. This is reasonable on the East side, since the samples closer to the contact show more of the darker blue luminescence correlating to a greater fluid inclusion density. In addition, quartz grains adjacent to mica and feldspar aggregates usually only show the darker blue luminescence, implying that the fluid is related to the visible alteration and formation of chlorite in the Lakenvalei Quartzite. This conclusion is supported by the compositions of the chlorite on either side of the Phepane Dome. Chlorite is Fe-rich on the felsic side, correlating to the Fe-rich hornblende in the felsic rock. On the West side, chlorite and hornblende in the mafic rock as well as chlorite in the Lakenvalei are all Mg-rich. Thus, the chlorite most likely formed due to fluid derived from the crystallizing magmas at this slightly lower temperature and darker blue luminescence stage. The same process of Fe and Mg transport could also explain the presence of calcite in the Lakenvalei Quartzite of the West Phepane and the lack of calcite in the Lakenvalei Quartzite of the East Phepane. However, the chlorite compositions only reflect measurements from two samples, so more analyses should

be made to confirm this. The final non-luminescent stage is not as widespread as the other stages, indicating small amounts of fluid infiltrated. The fracturing must have occurred after complete crystallization, since fractures cross cut both feldspars and quartz.

Figure 13: CL images of Lakenvalei Sandstone and Lakenvalei Quartzite

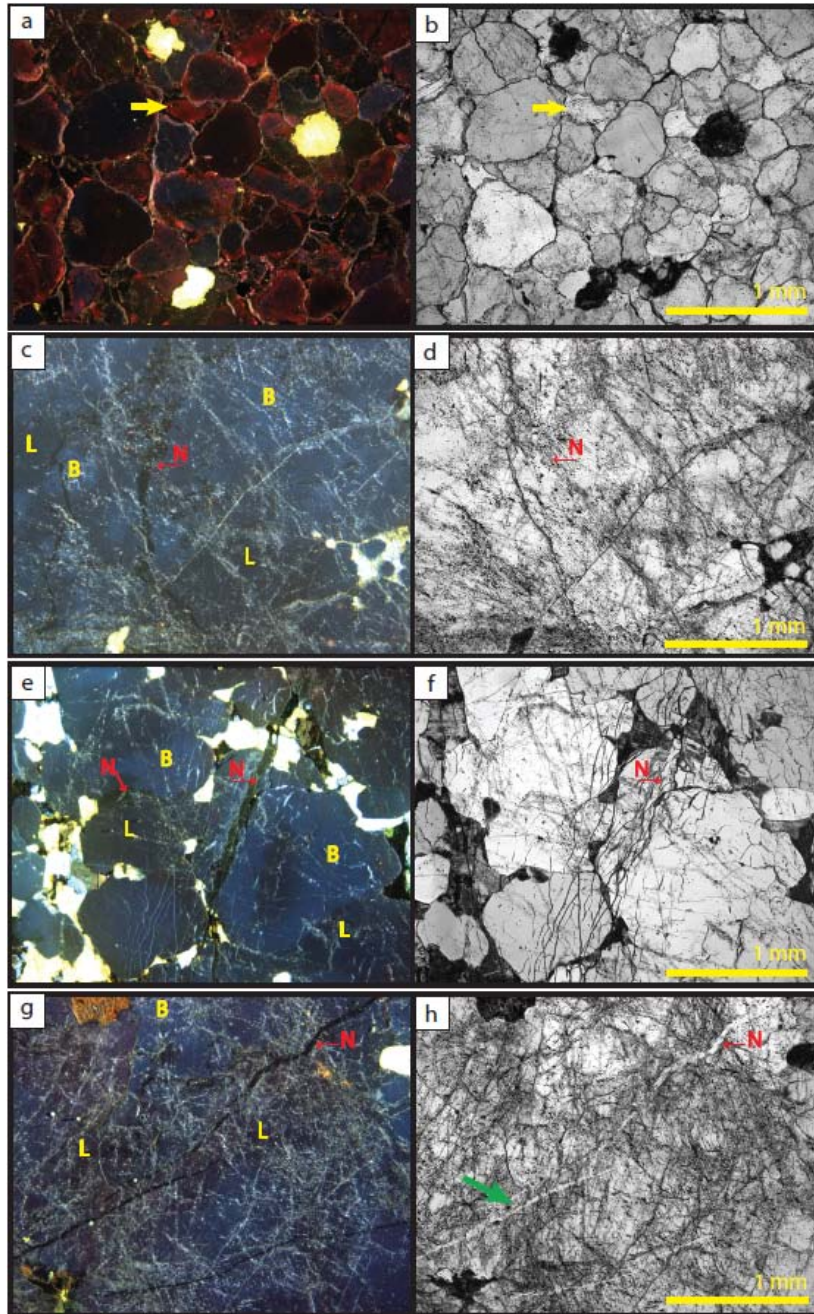


Figure 13: CL images on left, plane polarized light (PPL) on right. **(a)** Image of LV4, Lakenvalei Sandstone. Yellow arrow points to red luminescent authigenic quartz surrounded by non-luminescent cement. Three feldspar grains show yellow luminescence. **(c)** P06-16: note textures of bright blue luminescence (B), darker blue luminescence (L), and non-luminescent (N) quartz. The non-luminescent quartz is not visibly different in PPL. **(e)** P06-19: non-luminescent fracture cutting feldspar and quartz. Fracturing is visible in PPL, but extent of recrystallization is not. **(g)** P06-16: non-luminescent quartz in fluid inclusion-free fractures (green and red arrows in (h)).

Figure 14: CL images of P06-19

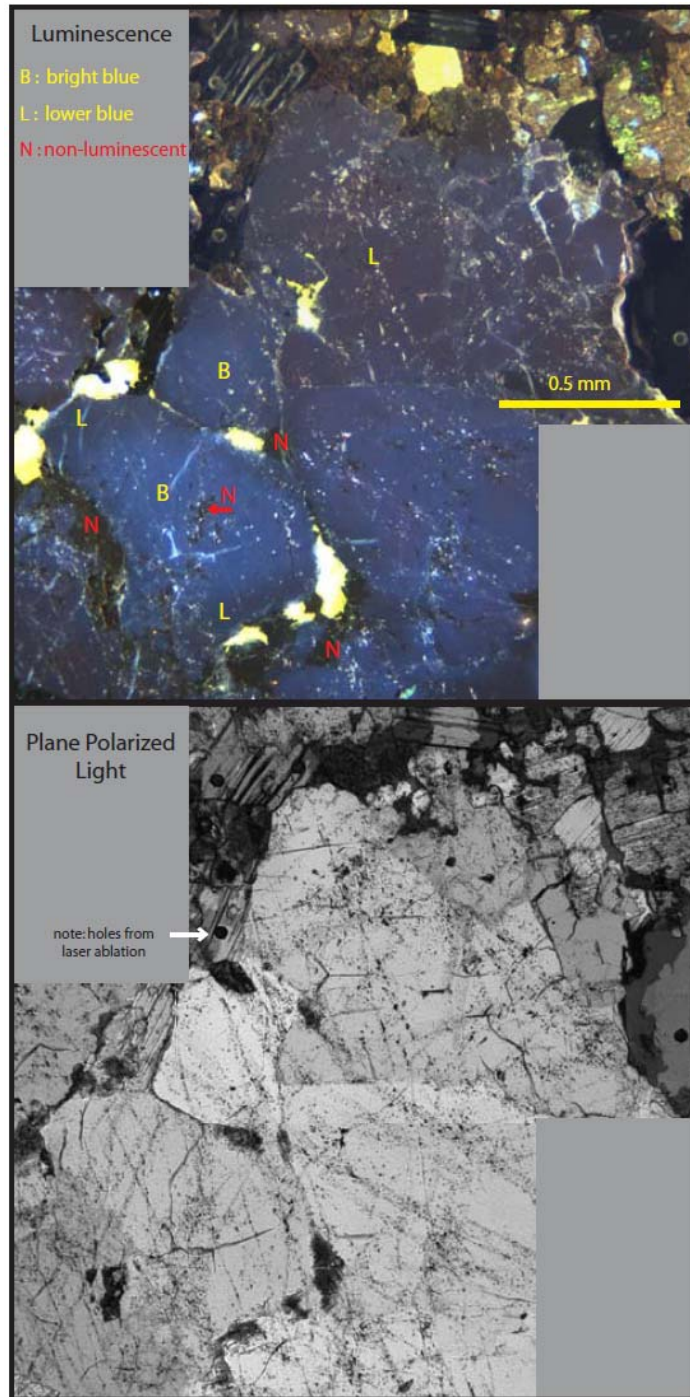


Figure 14: (top) Two images of P06-19 fit together to show relationship of bright blue luminescent quartz in grain interiors, darker blue luminescence along grain boundaries and comprising all of top quartz grain, and non-luminescent quartz between quartz grains. **(bottom)** Same fields of view in PPL.

Figure 15: CL images illustrating blue luminescent textures

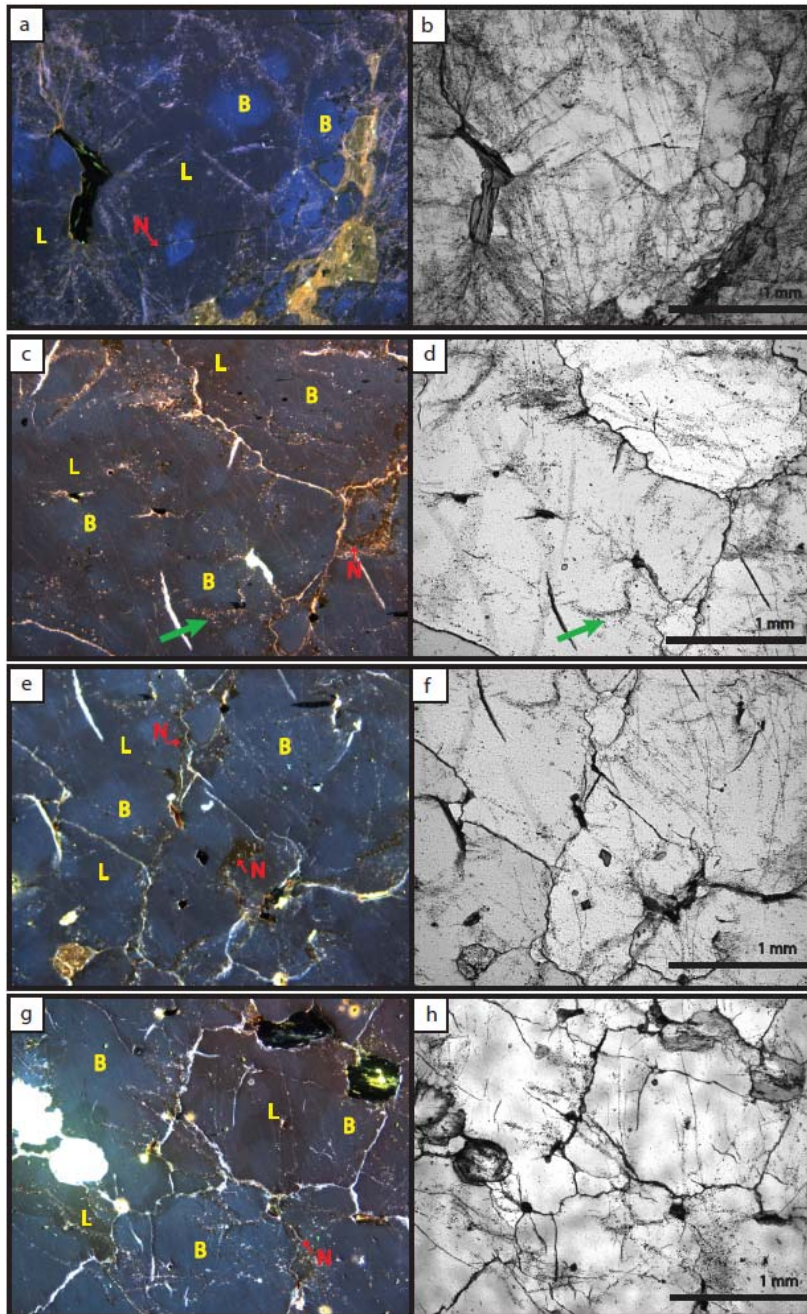


Figure 15: CL images on left, corresponding PPL on right. **(a)** P06-15: bright blue luminescence is reduced to small regions. This photo has been blue enhanced due to prolonged CL exposure on this sample, causing a shift of luminescence to red. **(c)** P07-14: showing bright blue regions surrounded by darker blue luminescence within one large quartz grain. Note fluid inclusions at bottom (green arrow) that coincide with the darker blue luminescent overgrowth. This photo has been slightly blue enhanced. **(e)** P07-14: bright blue regions within one quartz grain, and non-luminescent quartz that follows a fracture (top N) and that is within a bright blue quartz grain (bottom N). This photo was taken early, so no blue enhancement needed. **(g)** P07-1: sample is 50 m from the contact. Darker blue luminescence is reduced, but still found within quartz grains. Bright green-white is feldspar.

5.4: Oxygen isotopic compositions

The oxygen isotopic compositions of samples from each rock type are shown in Table 3. The average $\delta^{18}\text{O}$ of the Lakenvalei quartz is $11.21\pm 0.37\text{‰}$ on the East side and $10.87\pm 0.60\text{‰}$ on the West side (all ranges are 2 standard deviations). Quartz from the felsic Bushveld Complex igneous rock is $7.33\pm 0.81\text{‰}$. On the West side, the feldspar and whole rock powders of the mafic Bushveld Complex igneous rock yielded similar results for ranges of $8.13\pm 0.57\text{‰}$ and $7.60\pm 1.24\text{‰}$ respectively. When plotted with distance, there does not appear to be any systematic variation across the contact of either Transect (Figure 16). Both rock types are homogenous, with constant $\delta^{18}\text{O}$ as the contact is approached

For the West Small Scale Transect, to better compare the $\delta^{18}\text{O}$ of quartz from the Lakenvalei Quartzite with the $\delta^{18}\text{O}$ values of plagioclase in the gabbro, the oxygen isotope composition of fictive quartz in equilibrium with the mafic Bushveld Complex rock can be calculated from the measured plagioclase values using the fractionation factors for quartz-anorthite and quartz-albite from Clayton and Kieffer (1991) and using mass balance to calculate the fractionation for quartz-labradorite. At metamorphic temperatures of $\sim 500^\circ\text{C}$, the $\delta^{18}\text{O}$ values of fictive quartz in the mafic rock are around 11‰ (see Figure 16). For likely temperatures in the Phepane Dome (750°C ; Johnson et al., 2004), the fictive quartz would be $\sim 9.5\text{‰}$. At magmatic temperatures ($>1150^\circ\text{C}$), the fictive quartz would be $<1\text{‰}$ greater than the plagioclase values. At just under magmatic temperatures, representing exchange during cooling of the crystallized magma (900°C), the fictive quartz in the gabbro is intermediate between these values. This temperature is used in the model of

Bushveld Complex cooling and crystallization as the solidus temperature at which the Bushveld Complex magma would be completely crystallized (Cawthorn and Walraven, 1998). It also represents the temperature of “freezing in” of the diapir, as determined by the model of the formation of the Phepane diapir (Gerya et al., 2004). Assuming that there was no hydrothermal alteration, and that the addition of the cooler Phepane diapir rock would aid in a locally rapid cooling of the Bushveld magma, the preferred $\delta^{18}\text{O}$ values for quartz are the calculated values for cooling after crystallization. In this scenario, there is subsolidus exchange between the fictive quartz and the plagioclase, but exchange is halted as the system cooled quickly due to the influence of the cooler Phepane diapir. Thus, the minerals would record a higher temperature fractionation compared to slowly cooled systems (e.g., Giletti, 1989). Using a temperature of 900°C is supported by the calculated temperature of the Upper Zone magma using the $\delta^{18}\text{O}$ fractionation between plagioclase and pyroxene. Schiffries and Rye (1989) found two Upper Zone samples to preserve temperatures of 960°C and 1040°C in their $\delta^{18}\text{O}$ systematics. Samples measured by Harris et al. (2005) for Upper Zone rocks show a similar range in inferred temperatures.

Previous measurements of rocks from the Bushveld Complex and surrounding sedimentary rock are similar to the results found in this study. Harris et al. (2003) measured quartz mineral separates from the Lakenvalei and Magaliesburg Quartzites in the outer aureole of the Eastern Lobe and found a range of $\delta^{18}\text{O}$ values with an average of $11.8 \pm 0.5\%$. The one quartz mineral separate from the Lakenvalei Quartzite measured by Schiffries and Rye (1989) is similar at $11.06 \pm 0.2\%$ (error is 2σ). The Lakenvalei Quartzite results from both sides of the Phepane Dome fall

within these values. Previous measurements of plagioclase from the Upper Zone rock of the Eastern Lobe are also within error of the plagioclase measured in this study. Harris et al. (2005) measured sixteen plagioclase separates, giving an average of $7.5 \pm 1.2\%$. Schiffries and Rye (1989) measured only four plagioclase separates and found a confined range of $7.6 \pm 0.3\%$. Both studies calculated the parental magma $\delta^{18}\text{O}$ ($\sim 7.2\%$) and found it to be $\sim 1.5\%$ higher than a normal mantle melt ($\sim 5.7\%$). They interpreted the slightly higher $\delta^{18}\text{O}$ values to be due to crustal contamination of the Bushveld Complex magma. They also used the pyroxene-plagioclase $\delta^{18}\text{O}$ fractionation to show that the rocks preserved their magmatic values, precluding any effects of hydrothermal alteration on the oxygen isotopic compositions.

Table 3: Oxygen isotopic compositions

Sample	Rock Type	$\delta^{18}\text{O}$ (‰)	Material	Distance (m)
East Transect 2006				
P06-1	Felsic igneous	6.93	quartz	108
P06-2	Felsic igneous	7.92	quartz	89
P06-6	Felsic igneous	7.09	quartz	50
P06-8	Felsic igneous	7.37	quartz	30
P06-9	Felsic igneous	7.33	quartz	17
P06-14	Felsic igneous	6.90	quartz	4.3
P06-13	Felsic igneous	7.80	quartz	1.5
P06-15	Lakenvalei Quartzite	10.85	quartz	2.4
P06-15	Lakenvalei Quartzite	11.05	quartz	2.4
P06-16	Lakenvalei Quartzite	11.34	quartz	7.1
P06-18	Lakenvalei Quartzite	11.27	quartz	9.0
P06-18*	Lakenvalei Quartzite	11.41	quartz	9.0
P06-19	Lakenvalei Quartzite	11.21	quartz	13
West Small Scale				
P07-27	Lakenvalei Quartzite	11.05	quartz	42
P07-27	Lakenvalei Quartzite	10.83	quartz	42
P07-28A	Lakenvalei Quartzite	11.30	quartz	48
P07-28A*	Lakenvalei Quartzite	11.09	quartz	48
P07-28B	Lakenvalei Quartzite	11.08	quartz	48
P07-28B*	Lakenvalei Quartzite	11.06	quartz	48
P07-29	Lakenvalei Quartzite	10.40	quartz	19
P07-30A	Lakenvalei Quartzite	10.59	quartz	0.7
P07-30A*	Lakenvalei Quartzite	10.47	quartz	0.7
P07-30B	Lakenvalei Quartzite	10.57	quartz	0.7
P07-31	Mafic Igneous	8.27	whole rock	0.9
P07-31*	Mafic Igneous	8.12	whole rock	0.9
P07-31A	Mafic Igneous	8.54	plagioclase	0.9
P07-31B	Mafic Igneous	8.59	plagioclase	0.9
P07-32	Mafic Igneous	7.90	whole rock	19
P07-32	Mafic Igneous	8.08	whole rock	19
P07-32	Mafic Igneous	7.89	plagioclase	19
P07-32	Mafic Igneous	7.95	plagioclase	19
P07-33A	Mafic Igneous	7.39	whole rock	26
P07-33A*	Mafic Igneous	7.39	whole rock	26
P07-33A	Mafic Igneous	8.04	plagioclase	26
P07-34	Mafic Igneous	7.05	whole rock	33
P07-34*	Mafic Igneous	6.60	whole rock	33
P07-34	Mafic Igneous	8.02	plagioclase	33

Table 3: $\delta^{18}\text{O}$ measurements of mineral separates (quartz) and powders of whole rock and plagioclase mineral separates. * Repeat analyses of the same sample.

Figure 16: Oxygen isotopic compositions for the two measured transects

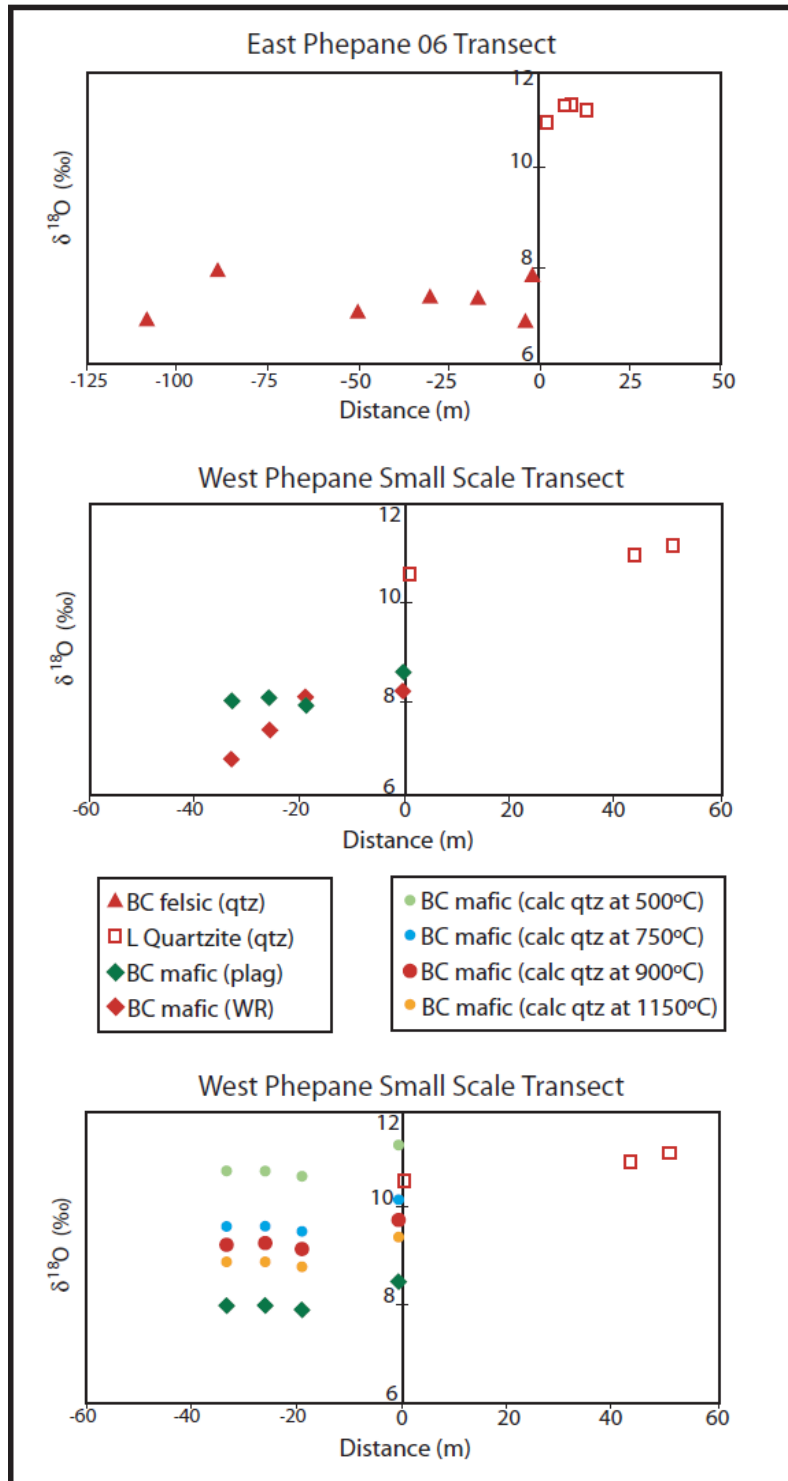


Figure 16: O isotopic compositions. Error is less than or equal to the size of the symbol. **(top)** Compositions are plotted with distance from the contact (at $x=0$) for the East Phepane 06 Transect and the West Phepane Small Scale Transect. **(bottom)** Calculated $\delta^{18}\text{O}$ of quartz (qtz) that would be in equilibrium with the measured $\delta^{18}\text{O}$ of the plagioclase at temperatures from 500°C to 1100°C..

5.5: Lithium concentrations

Results of the Li whole rock concentrations are reported in Table 4a-b. The felsic Bushveld Complex has the lowest concentration of Li, with a relatively constrained range of 5.0 ± 3.3 ppm. This differs from the mafic Bushveld Complex rock, which is more varied in concentration. Concentrations of most mafic samples are close to 40 ppm, but samples can be as low as 10 ppm. These lowest concentrations do not appear to be related to Li diffusion or exchange with the Lakenvalei, since these samples are not closest to the contact (see Figure 17a-b for plots of the four transects). However, the Lakenvalei Quartzite does have a lower Li concentration than the mafic rock, with a range of 13.8 ± 4.8 ppm on the West side. On the East side, the range in concentration of the Lakenvalei is 12.5 ± 9.0 ppm. It is apparent that the East side is much more heterogeneous than the West side, even though it is smaller in width. The Vermont Metapelite has the greatest Li concentrations, usually in the range of 70 to 100 ppm. The sample on the East side with a lower concentration of 44 ppm is within 1 m of the contact with the Lakenvalei; however, there may be internal heterogeneity with the Vermont Metapelite, as sample P06-14 on the West side has an even lower concentration of 14 ppm. This is possibly due to preservation of the initial heterogeneity in the protolith Vermont Shale. Lastly, two analyses of the Magaliesburg Quartzite resulted in a Li concentration of 13 and 8.8 ppm.

Measurements of the sedimentary protolith concentrations (Table 4c) correlate with their respective meta-sedimentary concentrations in the Phepane Dome. Four analyses of the Lakenvalei sandstone gave concentrations of 2.3, 8.3, 9.1 and 13.3

ppm. These values are slightly lower, but only the sample with a concentration of 2.3 ppm falls outside the range of the Lakenvalei Quartzite. The one analysis of the Vermont Shale resulted in a concentration of 142 ppm, consistent with the higher concentrations found in the Vermont Metapelite.

One explanation of the differences in whole rock Li concentrations could be the relative concentrations of Li in minerals and the abundances of these minerals in the rock. Table 5a shows the results of the laser ablation analysis of each mineral. The minerals with the greatest amount of Li are the micas and the pyroxenes. The feldspars generally do not contain much Li. In the felsic rock, the K-feldspar has less than 0.37 ppm Li, while plagioclase has between 1 and 25 ppm. The amount of Li is also variable in the hornblende, which has concentrations between 2.5 and 17 ppm. There does not appear to be any correlation between the amount of Li measured and mineral orientation, fracturing, or zoning of the plagioclase and hornblende. In keeping with the hypothesis above, the low whole rock concentrations of the felsic rock could reflect the abundance of K-feldspar. However, in the minerals measured by laser ablation in the Lakenvalei Quartzite, the micas have the highest concentrations of Li and comprise no more than 3% of the rock. Muscovite was found to have concentrations in the range of 50 ppm, while the chlorite has between 200 and 400 ppm. The feldspars again do not contain as much Li, suggesting that the micas control the whole rock concentrations. However, sample P06-19, with 2.56% muscovite and 0.19% chlorite, has a whole rock concentration of 14 ppm, while P07-28, with only 0.38% muscovite and 0.05% chlorite, has a greater concentration of 17ppm. This indicates that the micas do not control the lithium budget of the

Lakenvalei Quartzites. It is likely that the quartz, which was not measured by laser ablation, dominates the Li budget. Mass balance shows that quartz should have at least ~12 ppm Li in sample P06-19 and at least ~17 ppm Li in sample P07-28. Quartz is able to take in Li and other 1+ cations as a charge balance when Al substitutes for Si (Götze et al., 2001). Another consideration is the abundant fluid inclusions in the Quartzite. The fluid inclusion composition has been shown to influence the Li budget of pegmatite quartz grains (Teng et al., 2006b).

Because the Li concentrations of the Lakenvalei Quartzite are dominated by the quartz or the fluid inclusions within the quartz, it is difficult to correlate the unmetamorphosed Lakenvalei Sandstones to the Lakenvalei Quartzite in the Phepane Dome. The three sedimentary samples that were taken closest to the Bushveld Complex (LV2, LV3, and LV6) have concentrations within the range of the Li concentration of the Lakenvalei Quartzite but are slightly lower. All sedimentary and metamorphic samples contain similar mineral assemblages of quartz, feldspar, muscovite and chlorite, with the exception of LV2 that has schorl. A trend of decreasing feldspar abundance with increasing Li concentration was noticed (see Figure 18), possibly due to the extremely low concentrations of Li in feldspar. The abundance of feldspar is based on visual observations of thin sections using a petrographic microscope and is compared to the measured whole rock Li concentrations. The higher Li concentrations in the Lakenvalei Quartzite of the Phepane Dome could be related to the lower abundances of feldspar of these samples. It is also important to consider the very low Li concentration of the fourth Lakenvalei Sandstone sample (LV4: 2.3 ppm). This sample was taken more than 35 km away

from the other three samples, while samples LV2 and LV3 that are within 3 km of each other have very similar Li concentrations (8.3 and 9.1 ppm). This shows that there is variability within the Lakenvalei Sandstone at the 10's of km scale. Because the Phepane Dome is 60 km away from these samples, it is possible that the Lakenvalei started with a higher Li concentration than these Lakenvalei Sandstone samples that were measured.

When investigating the Li budget of the mafic Bushveld Complex rock, two samples were chosen for laser ablation; P07-32, which contains more felsic minerals, and P07-6 that contains pyroxene. The distribution of Li in the more felsic sample correlates with the Lakenvalei and felsic rock Li budgets reported above. In this sample (P07-32), the chlorite is enriched in Li at ~350 ppm, while the hornblende contains between 4 and 13 ppm. The plagioclase has a low concentration of ~2 ppm. In the more mafic sample, the hornblende is variable (3.6 to 17 ppm), but has the same range as the hornblende in the felsic sample, and the pyroxenes are more enriched with concentrations between 15 and 33 ppm. If the whole rock concentrations are solely based on mineral abundances, sample P07-6 should have a greater whole rock concentration than P07-32, since P07-6 contains more pyroxene. Although this is the case, closer examination reveals that the plagioclase in P07-6 is also enriched in Li compared to the plagioclase in the more felsic sample, and even every other plagioclase measured. This is curious, because the hornblendes have similar Li concentration. Nevertheless, it cannot be concluded that the Li whole rock concentrations mirror the mineral distribution of the mafic rocks, because the plagioclase is also Li enriched in the sample of greater whole rock concentration.

Table 4a: Li isotopic compositions and concentrations of the East Phepane

Sample	Rock Type	$\delta^7\text{Li}$ (‰)	Li (ppm)	Distance (m)
East Phepane 06				
P06-1	Felsic igneous	5.6	2.5	108
P06-1*	Felsic igneous	5.7	3.7	108
P06-2	Felsic igneous	3.6	4.5	89
P06-2**	Felsic igneous	4.9	3.7	89
P06-3	Felsic igneous	4.7	4.4	79
P06-8	Felsic igneous	2.5	4.7	30
P06-9	Felsic igneous	6.2	2.7	17
P06-14	Felsic igneous	5.4	4.5	4.3
P06-14**	Felsic igneous	5.4	4.5	4.3
P06-13	Felsic igneous	3.0	6.5	1.5
P06-15	Lakenvalei Quartzite	18.8	17	2.4
P06-16	Lakenvalei Quartzite	21.8	12	7.1
P06-16*	Lakenvalei Quartzite	21.2	11	7.1
P06-18	Lakenvalei Quartzite	18.6	21	9.0
P06-18**	Lakenvalei Quartzite	20.1	13	9.0
P06-19	Lakenvalei Quartzite	21.2	14	13
P06-20	Vermont Metapelite	2.1	37	13
P06-20**	Vermont Metapelite	4.7	84	80
East Phepane 07				
P07-49	Felsic igneous	8.6	5.7	67
P07-59	Felsic igneous	2.3	7.0	39
P07-58	Felsic igneous	5.1	6.4	27
P07-52	Felsic igneous	7.6	3.8	8.2
P07-53	Felsic igneous	12.7	7.8	4.9
P07-50	Lakenvalei Quartzite	3.2	4.7	0.1
P07-51	Lakenvalei Quartzite	35	12	3.5
P07-55	Vermont Metapelite	7.2	44	3.6
P07-56	Vermont Metapelite	3.0	105	34
P07-54	Vermont Metapelite	8.1	94	69
P07-57	Magaliesburg Quartzite	22.1	13	149

* Same sample stock solution, run through exchange columns again

** Same sample, redissolved and run through exchange columns again

Table 4b: Li isotopic compositions and concentrations of the West Phepane

Sample	Rock Type	$\delta^7\text{Li}$ (‰)	Li (ppm)	Distance (m)
West Phepane Large transect				
P07-12	Mafic igneous	-0.2	19	241
P07-11	Mafic igneous	6.0	43	124
P07-9	Mafic igneous	1.9	28	75
P07-8	Mafic igneous	3.4	40	60
P07-7	Mafic igneous	6.2	39	35
P07-6	Mafic igneous	6.1	42	20
P07-15	Mafic igneous	6.0	24	2.6
P07-14	Lakenvalei Quartzite	17.5	15	10
P07-1	Lakenvalei Quartzite	10.6	13	50
P07-3	Lakenvalei Quartzite	9.6	16	52
P07-5	Vermont Metapelite	-7.4	91	54
P07-16	Vermont Metapelite	6.7	71	71
P07-18	Vermont Metapelite	4.0	14	98
P07-23	Vermont Metapelite	4.1	70	264
P07-24	Vermont Metapelite	5.0	67	303
P07-25	Magaliesburg Quartzite	25.5	8.8	372
West Phepane Small Scale				
P07-33a	Mafic igneous	3.6	12	26
P07-33b	Mafic igneous	2.1	10	26
P07-33b**	Mafic igneous	2.3	14	26
P07-32	Mafic igneous	5.0	22	19
P07-32**	Mafic igneous	6.1	27	19
P07-31	Mafic igneous	3.4	19	0.8
P07-31**	Mafic igneous	2.7	24	0.8
P07-30	Lakenvalei Quartzite	9.0	10	0.6
P07-30**	Lakenvalei Quartzite	8.1	16	0.6
P07-29	Lakenvalei Quartzite	9.6	13	19
P07-26	Lakenvalei Quartzite	16.2	9.9	43
P07-28	Lakenvalei Quartzite	19.3	17	51

* Same sample stock solution, run through exchange columns again

** Same sample, redissolved and run through exchange columns again

Table 4c: Li isotopic compositions and concentrations of Transvaal sedimentary rock

Sample	Rock Type	$\delta^7\text{Li}$ (‰)	Li (ppm)	
Sedimentary Samples				
LV2	Lakenvalei Sandstone	21.7	9.1	
LV3	Lakenvalei Sandstone	12.4	8.3	
LV4	Lakenvalei Sandstone	9.8	2.3	
LV6	Lakenvalei Sandstone	13.3	17	
VT1a	Vermont Shale	0.3	142	
BHV0-1*	Basalt standard	3.6	4.4	
BHV0-2*	Basalt standard	4.0	5.7	

* Standards dissolved and run through columns

Table 5a: Individual mineral Li concentrations

Lakenvalei Quartzite Li (ppm)			
	average	min	max
P07-28			
Kfs	2.6	0.6	4.1
Pl	2.0	1.4	3.0
Ms	4.1	2.0	7.0
Chl	209	116	252
P06-19			
Pl	5	2.3	8.8
Ms	37	14	58
Chl	295	203	355
Bushveld Complex Felsic rock			
	Li (ppm)	min	max
P06-14			
Kfs	<0.37		0.37
Pl	13	1.2	25
Hbl	5.0	2.5	9.0
P06-2			
Kfs	2.8	<0.6	2.8
Pl	10.6	3.2	20
Hbl	8.8	4.0	17
Bushveld Complex Mafic rock			
	Li (ppm)	min	max
P07-6			
Pl	32	28	36
Hbl	7.9	3.5	17
Cpx	30	27	33
Opx	18	14	27
P07-32			
Kfs	<3.1		3.1
Pl	1.4	0.1	2.6
Hbl	8.8	4	13.2
Chl	353	329	377

Table 5b: Laser Ablation Standards

	Li (ppm) measured	sample
BCR-2g	10.4	L Quartzite
	9.1	BC felsic
	10.1	BC mafic
BCR-2g	10.0	literature
NIST 610	484.6	literature

Table 5: (a) Lithium concentrations of minerals in samples from the Lakenvalei Quartzite and the felsic and mafic Bushveld Complex rock measured by LA-ICP-MS. The average concentration is from analyses of 2 to 6 spots in the mineral. Mineral abbreviations after Kretz (1983) Min= minimum Li concentration measured in mineral; Max= maximum Li concentration measured in mineral. **(b)** Li concentration measurements of standard BCR-2g and reported Li concentrations for BCR-2g and external standard NIST 610 (used in LAMTRACE calculation).

Figure 17a: Lithium concentrations of the East Phepane

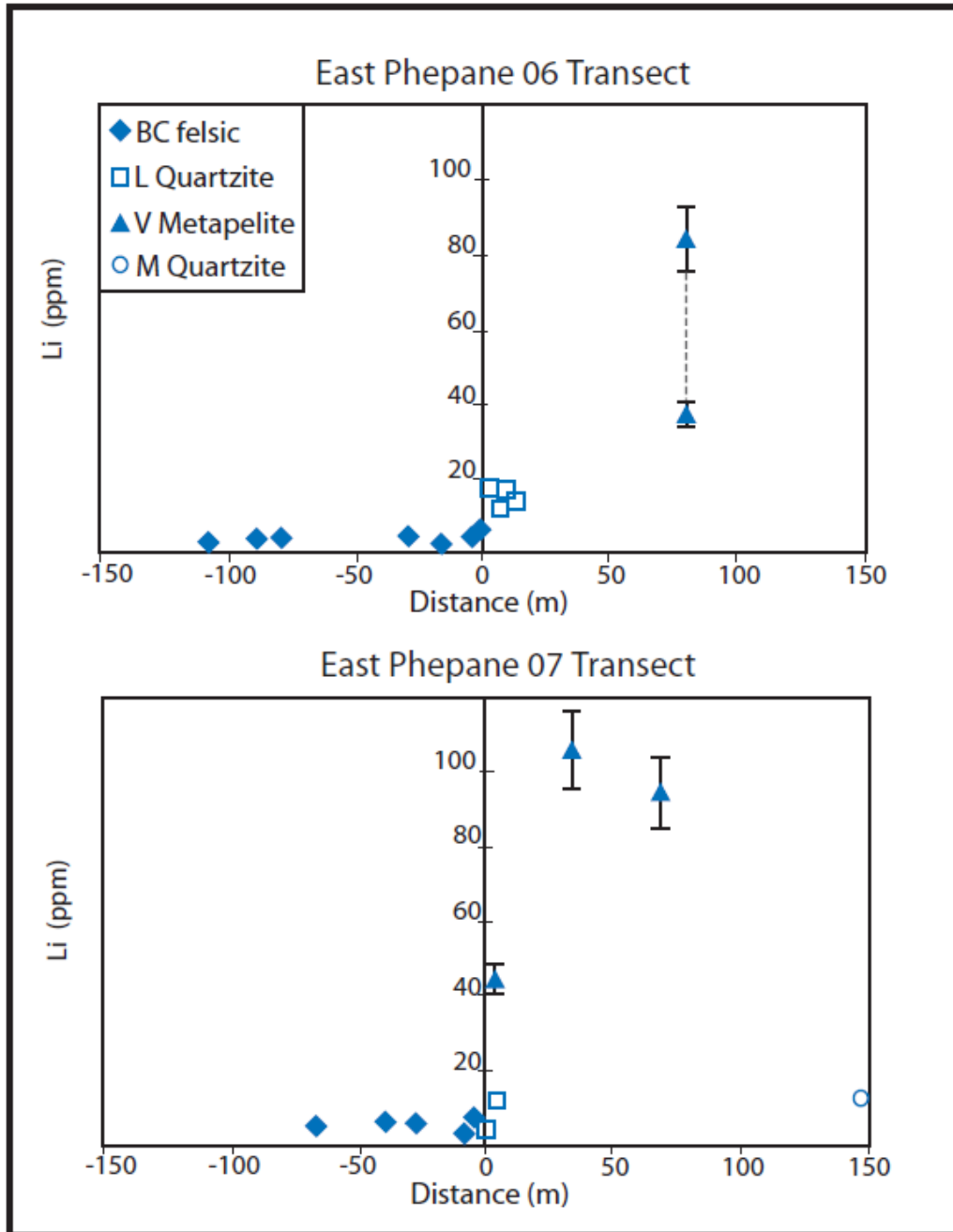


Figure 17a: Li concentrations of the Bushveld Complex felsic rock (left) and Lakenvalei Quartzite (right) in the East Phepane Transects (contact at $x=0$). If no error bars are shown on data point, error is less than or equal to the size of the symbol. Points are averages of multiple concentration measurements if possible, excluding the one Vermont Metapelite sample measured in the East Phepane 06 Transect, since this sample has an extremely large range (the two measured concentrations of this sample are connected by dotted line).

Figure 17b: Lithium concentrations of the West Phepane

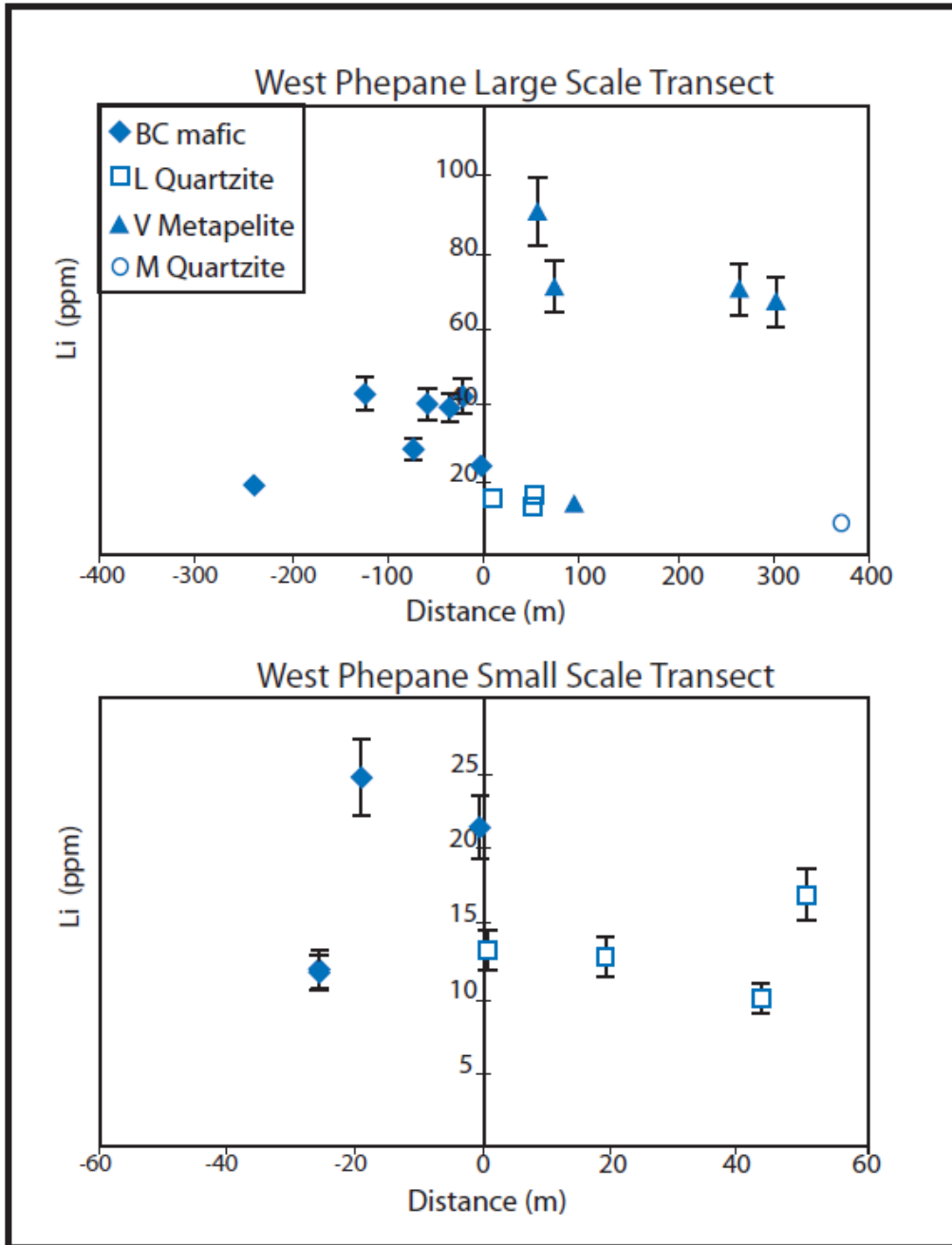


Figure 17b: Li concentrations of the Bushveld Complex mafic rock (left) and Lakenvlei Quartzite (right) in the West Phepane Transects (contact at x=0). If no error bars are shown on data point, error is less than or equal to the size of the symbol. Points are averages of multiple concentration measurements if possible.

Figure 18: Feldspar abundance compared to Li whole rock concentration

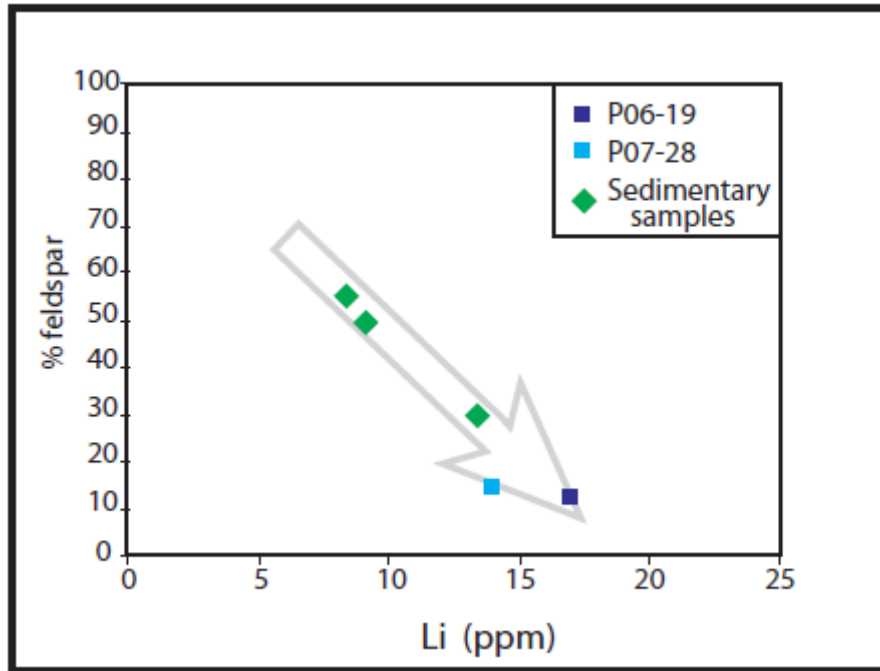


Figure 18: Lithium whole rock concentrations of sedimentary samples from the Lakenvalei Sandstone and two samples of Lakenvalei Quartzite. Feldspar abundance (%) was estimated from visual observations using a petrographic microscope. The lower abundances of feldspar in the Quartzite may explain the higher Li concentrations of the Lakenvalei Quartzite compared to the Lakenvalei Sandstone.

5.6: Lithium isotopic compositions

The $\delta^7\text{Li}$ values in each rock type are variable, resulting in large ranges (see Table 4a-c for compositions and Figure 19a-c for plots of $\delta^7\text{Li}$ with distance in each transect). The felsic rock has an average $\delta^7\text{Li}$ value $5.7\pm 5.8\text{‰}$ (all ranges are 2 standard deviations), the Vermont Metapelite has an average of $5.0\pm 4.0\text{‰}$, and the mafic rock has a slightly lower average value at $3.9\pm 4.1\text{‰}$. The Lakenvalei Quartzite is generally around $20\pm 17\text{‰}$ on the East side and $14\pm 5.4\text{‰}$ on the West side. Because the ranges are large, each transect will be considered individually.

Starting with the East side, East Phepane 06 appears to have distinct $\delta^7\text{Li}$ values in each rock type. The felsic rock shows greater variability in $\delta^7\text{Li}$ as the contact is approached, but the Lakenvalei does not show a strong distance dependent variation. The one Vermont Metapelite sample of this transect was measured twice and resulted in values outside the range of uncertainty for each measurement (represented by large error bars in Figure 19a). The East Phepane 07 Transect exhibits more variation in the felsic rock and the Lakenvalei has a much larger $\delta^7\text{Li}$ range. Like the 06 Transect, the Vermont Metapelite and felsic rock have similar $\delta^7\text{Li}$ values. However, the $\delta^7\text{Li}$ measurements of the Lakenvalei Quartzite in the East Phepane 07 Transect are different than the Lakenvalei $\delta^7\text{Li}$ values measured in all other traverses. These two values are the isotopically lightest and heaviest values measured for the Lakenvalei Quartzite. The Quartzite layer in this transect is also significantly thinner than the Lakenvalei Quartzite in the other traverses. In the East Phepane 06 Transect, the Lakenvalei Quartzite is at least 13 m thick, while it is 50 m thick in both traverses on the West side of the Phepane Dome. However, in the East Phepane 07 Transect, the Lakenvalei is less than 3.6 m thick. Because the two East Phepane 07 samples are therefore close to the contact with the Vermont Metapelite, the $\delta^7\text{Li}$ values could be skewed by exchange with the Li-rich metapelite. Therefore, these values are not considered in the East Phepane Li diffusion model. Because these are the only Lakenvalei Quartzite data points close to the contact in the East Phepane 07 Transect, the two East Transects are combined in the modeling. Considering the East Transects together, it can be concluded that the felsic rock and Vermont Metapelite have similar $\delta^7\text{Li}$ values (felsic $\delta^7\text{Li}$ range: 2.3-8.6‰; Vermont

$\delta^7\text{Li}$ range: 3.0-8.1‰), and the Lakenvalei quartzite has heavier $\delta^7\text{Li}$ values (average of 20‰) (see Figure 19b).

The West Phepane Transects can also be generalized as having mafic rock and Vermont Metapelite $\delta^7\text{Li}$ values that are similar, while the Lakenvalei $\delta^7\text{Li}$ values are higher. However, the transects do not show identical trends in $\delta^7\text{Li}$ values with respect to distance from the contact. The $\delta^7\text{Li}$ of the mafic rock shows a range from -0.2 to 6.2‰ in the Large Scale Transect, while the three samples from the Small Scale Transect range from 2.1 to 5.6‰. The main difference between the West Transects is the Lakenvalei layer, which is 50 m thick in both Transects. The $\delta^7\text{Li}$ values increase with distance from the contact in the Small Scale Transect, but decrease with distance in the Large Scale Transect. This difference could be due to error in the distance measurements, since the West Large Scale Transect was the only Transect where measuring tape could not be used in the field, or complications with another metasedimentary structure found on the West side of the Phepane Dome. The West Phepane Large Scale Transect was sampled close to this structure. The structure is not connected to the Phepane Dome at current outcrop exposure, as there is mafic rock between metasedimentary outcrops. It is comprised of quartzite, although it is unclear whether it can be associated with Magaliesburg or Lakenvalei Formations. It is possible that this structure is another, smaller diapir associated with the diapirism of the Phepane, but more study is needed to determine this. In any case, this structure indicates that the West Large Scale Transect is likely not a simple perpendicular traverse across the Phepane-Bushveld contact. It is possible that exchange could have occurred between this structure, the Phepane Dome

metasedimentary rock, and the mafic Bushveld rock. The Vermont Metapelite was not measured in the Small Scale Transect, but the $\delta^7\text{Li}$ values measured in the Large Scale Transect are similar to the Vermont Metapelite in the East Phepane.

The $\delta^7\text{Li}$ values of the four protolith Lakenvalei Sandstone samples are 9.8‰, 12.4‰, 13.3‰ and 21.7‰. As with concentrations, these values are all within the range of Lakenvalei Quartzite $\delta^7\text{Li}$ compositions. The Vermont Shale is 0.3‰, lower than most Metapelite samples. However, this is only one sample and cannot be extrapolated to the entire Vermont Shale $\delta^7\text{Li}$ composition.

Figure 19a: Lithium isotopic compositions of the East Phepane

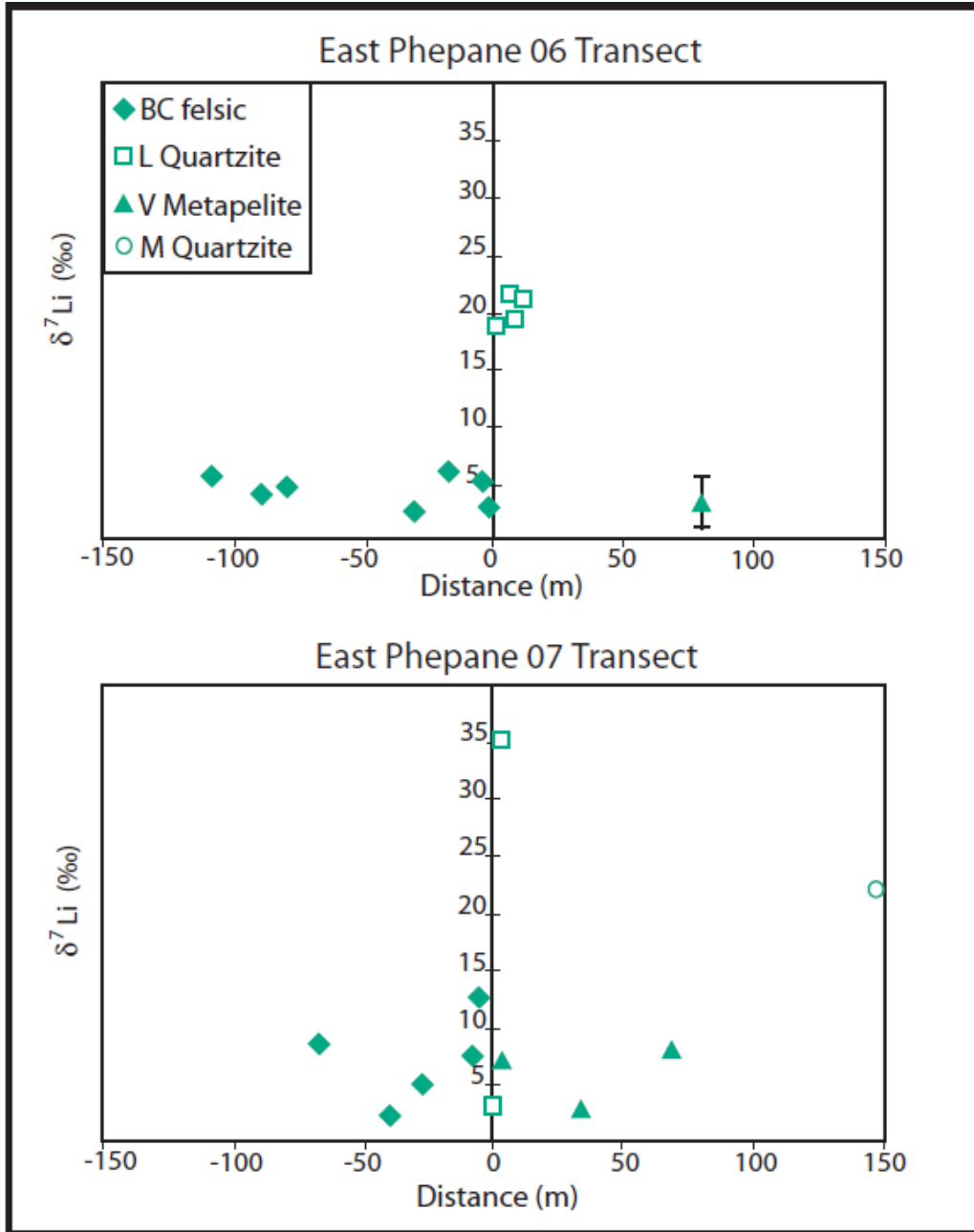


Figure 19a: Li isotopic compositions of the Bushveld Complex felsic rock (left) and Lakenvalei Quartzite (right) in the East Phepane Transects (contact at $x=0$). If no error bars are shown on data point, error is less than or equal to the size of the symbol. Points are averages of multiple measurements if possible.

Figure 19b: Lithium compositions of the East Phepane 06 and 07 Transects

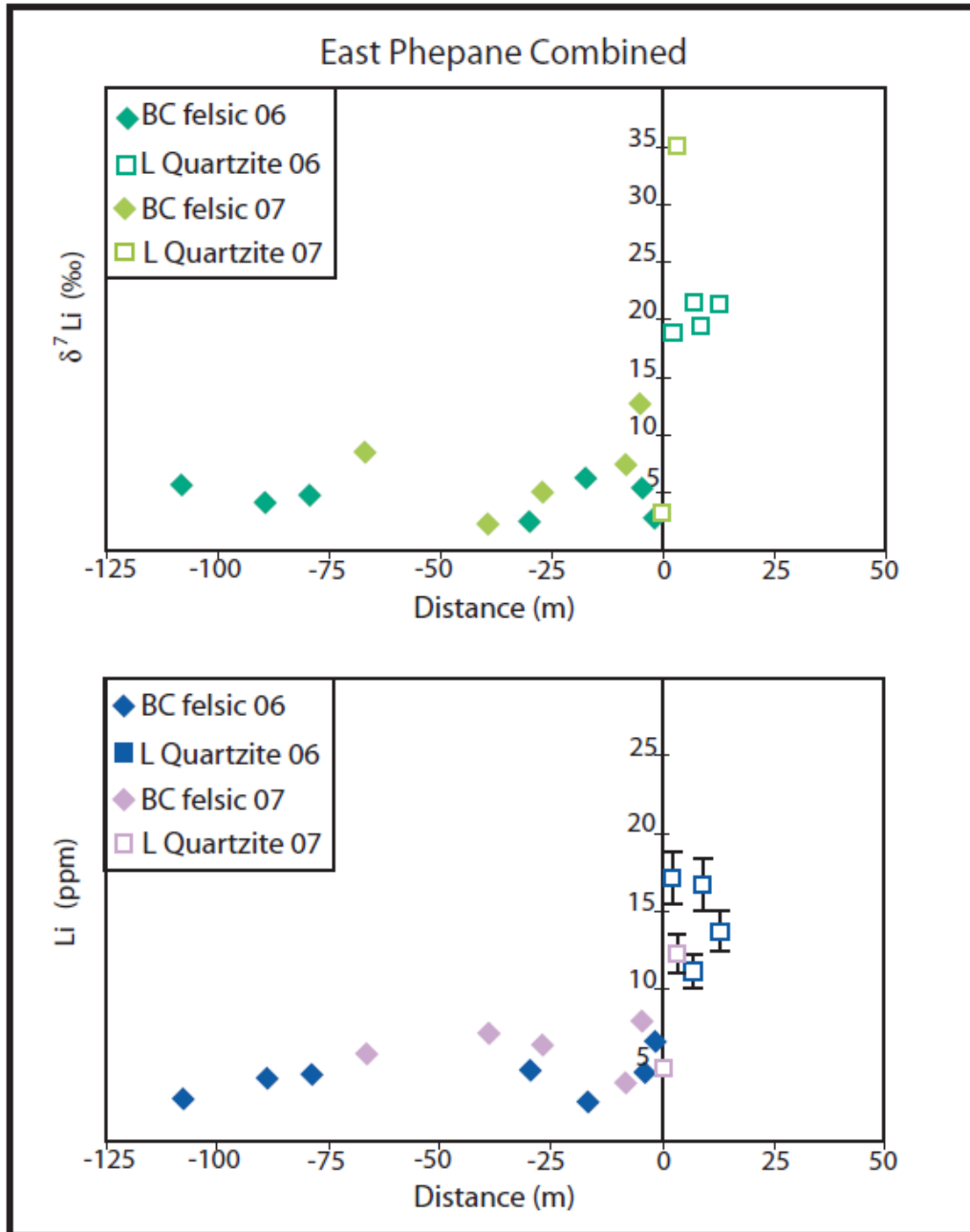


Figure 19b: Li concentrations and isotopic compositions of the Bushveld Complex felsic rock (left) and Lakenvalei Quartzite (right) in the East Phepane Transects (contact at $x=0$). If no error bars are shown on data point, error is less than or equal to the size of the symbol. Points are averages of multiple concentration measurements if possible.

Figure 19c: Lithium isotopic compositions of the West Phepane

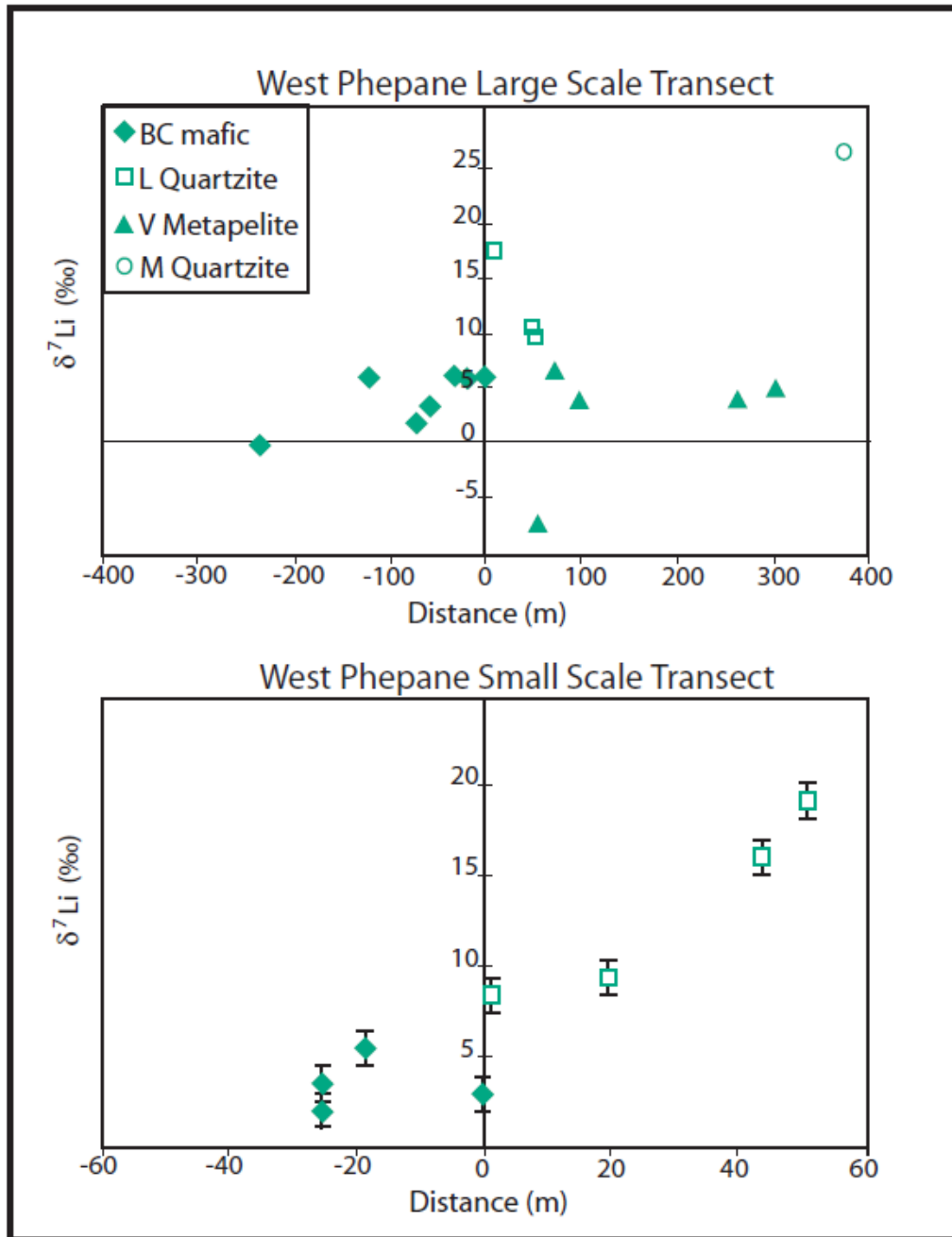


Figure 19c: Li isotopic compositions of the Bushveld Complex mafic rock (left) and Lakenvalei Quartzite (right) in the West Phepane Transects (contact at $x=0$). If no error bars are shown on data point, error is less than or equal to the size of the symbol. Points are averages of multiple measurements if possible

Chapter 6: Discussion and Modeling

6.1: Oxygen compositions

The homogenous but distinct oxygen isotopic compositions of the Lakenvalei Quartzite and the Bushveld Complex igneous rock preclude extensive interaction between these rocks. While it is likely that there was limited oxygen isotopic exchange at the contact, there does not seem to be large scale communication between the rocks. The slightly ^{18}O enriched mafic Bushveld Complex rock compared to other mantle derived rocks could suggest interaction with upper crustal rocks, but previous studies have interpreted the heavy $\delta^{18}\text{O}$ values throughout the entire Complex as the product of crustal contamination in a subsurface staging magma chamber (Schiffries and Rye, 1989; Harris et al., 2005). Moreover, the marked difference between the metasedimentary and felsic oxygen isotopic compositions indicates that the felsic magmatism was indeed part of a late stage Bushveld Complex intrusion and not melt derived from the sedimentary aureole rocks. Only the two samples taken at ~ 2 m from either side of the contact on the East side of the Phepane Dome and the two samples taken at < 1 m from either side of the contact on the West side of the Phepane Dome show possible oxygen isotopic exchange (see Figure 16), but this could be due to the natural variability within each rock type as shown by the slight variations in $\delta^{18}\text{O}$ composition of samples farther from the contact on the East side. Thus, there is no apparent large scale interaction between the Bushveld Complex igneous rocks and the meta-sedimentary rocks of the

Phepane Dome, suggesting that exchange between these rocks was limited or even nonexistent.

The correlation of oxygen isotopic compositions from this study to previous studies also supports the limited interaction of these rocks. Two studies have analyzed plagioclase from the Upper Zone of the Bushveld Complex ($7.6\pm 0.3\text{‰}$, Schiffries and Rye, 1989; $7.5\pm 1.2\text{‰}$, Harris et al., 2003). These studies interpreted the oxygen isotope compositions as unaltered by a secondary fluid, since the fractionation between pyroxene and plagioclase $\delta^{18}\text{O}$ values resulted in the calculation of magmatic temperatures ($\sim 1000^\circ\text{C}$). Because the plagioclase from this study has a $\delta^{18}\text{O}$ range ($8.13\pm 0.57\text{‰}$) within error of the values measured in these studies, it is likely that the mafic Bushveld Complex rocks in this study are also unaltered. Other evidence for minimal secondary alteration is the similar $\delta^{18}\text{O}$ quartz values from unmetamorphosed sedimentary rock and aureole meta-sedimentary rock. Harris et al. (2003) hypothesized that this similarity implies that magmatic fluid could not have interacted with the sedimentary rocks.

The lack of significant secondary alteration suggests that a diffusive profile in $\delta^{18}\text{O}$ compositions across the contact of the Bushveld Complex and Phepane Dome would be preserved. However, $\delta^{18}\text{O}$ compositions are relatively constant within each lithologic unit, suggesting that there was only small scale oxygen isotopic exchange across the lithologic contacts, or that quartz has not recorded any of the oxygen isotopic exchange. The latter case is improbable because it has already been shown that the rocks were at high enough temperatures to partially melt, and the CL images show extensive recrystallization during contact metamorphism. These both imply

that local equilibrium between the intergranular medium and the mineral is maintained due to the high temperature and the amount of recrystallization. Therefore, the mechanism of isotopic exchange between the quartz and the intergranular medium during contact metamorphism is likely dissolution-precipitation and not diffusion of oxygen into the quartz grains. Dissolution-precipitation is relatively instantaneous and would record the across-contact ^{18}O exchange in the quartz, while diffusion of oxygen into quartz would be too slow to record isotopic changes in the intergranular medium even at high temperatures (10^{-20} m²/s at 800°C, Gilletti and Yund, 1984). However, this slow diffusivity of oxygen in quartz indicates that the potential diffusive profile produced during contact metamorphism would be preserved, as quartz would not be reset by post-magmatic exchange during cooling.

6.2: Lithium compositions

The Li concentrations and isotopic compositions of each rock type are consistent with measurements of similar lithologies from previous studies. Teng et al. (2004) found shales to have a range of $\delta^7\text{Li}$ values from -3.2 to 3.9‰, and concentrations of 28 to 109 ppm, comparable to the single measurement of unmetamorphosed Vermont Shale in this study, which has a $\delta^7\text{Li}$ of 0.3‰ and a slightly higher concentration of 142 ppm. The metamorphosed Vermont Metapelite is also similar to the shale range of concentrations (~65 ppm), but is enriched in ^7Li (~5‰) relative to the shale value in this study and previous measurements of shale $\delta^7\text{Li}$ values. Unmetamorphosed Lakenvalei Sandstones have even heavier $\delta^7\text{Li}$ values (9.8 to 21.7‰), which is reasonable because sands are usually enriched in ^7Li relative to clay minerals (Chan et al., 2004). In the Phepane Dome, the

metamorphosed Lakenvalei Quartzite has similar $\delta^7\text{Li}$ values to the sandstone protolith, but a greater Li concentration. The Lakenvalei Sandstone has an average concentration of 8.2 ppm, while the average concentration of the Lakenvalei Quartzite is 13 ppm. The Lakenvalei Quartzite average $\delta^7\text{Li}$ of $\sim 20\text{‰}$ and average concentration are consistent with a previous measurement of quartzite from South Greenland which has a $\delta^7\text{Li}$ value of 19.1‰ and a concentration of 10.3 ppm (Marks et al., 2007). Thus, the measured $\delta^7\text{Li}$ values and concentrations of the Transvaal sedimentary rock and Phepane Dome meta-sedimentary rock are within the expected range for each respective lithology.

The $\delta^7\text{Li}$ compositions of granites have been shown to correlate to their source composition; S-type granites (-1.4 to 2.1‰) are generally lighter than I-type granites (1.9 to 8.0‰) (Bryant et al., 2004; Tomascak, 2004). Teng et al. (2004) also looked at a variety of I- and S-type granites and measured a small range in $\delta^7\text{Li}$ values (-2.5 to 2.7‰), while concentrations ranged from 16 to 187 ppm, depending on the source of the granite. Marks et al. (2007) measured I-type country rock granites from the Ilimaussaq Complex in Greenland. Samples of these I-type granitoids were taken far from the contact of the Ilimaussaq intrusion in order to characterize the actual granite composition, measured as 5 to 13 ppm and 0.4 to 6.3‰ . A recent study by Teng et al. (in press) compared the Li isotopic compositions and concentrations of A-type granites to I- and S-type granites. A-type granites are thought to be derived from partial melt of the lower crust or from differentiation of a crustal contaminated magma from the mantle. This study found that A-type granites from China have $\delta^7\text{Li}$ compositions of -1.8 to 6.9‰ , similar to both I- and S-type granites, while Li

concentrations for A-type granites (2.8 to 80 ppm) are similar to I-type granites and slightly lower than S-type granites. The low Li concentration of the Bushveld Complex felsic rock (5 ppm) correlates with these A-type granites, and the slight enrichment in ^7Li (felsic average = 5.6‰) is likely due to the source composition.

The Bushveld Complex mafic rock can have ten times as much Li as the felsic rock, which is unusual considering that more differentiation will concentrate the moderately incompatible Li. Marks et al. (2007) tracked the change in Li composition with increasing differentiation in the Ilimaussaq Complex. They saw an increase in Li whole rock concentration from the least differentiated augite syenite (7 to 25 ppm) to the most differentiated lujavrites (150 to 750 ppm). Therefore, it is strange that these high concentrations are in the mafic Bushveld Complex rock and not the felsic Bushveld rock. It could imply that the mafic and felsic rock have different sources. This is supported by the differing oxygen isotopic compositions of the felsic and mafic rocks as well, because quartz from the felsic rock is $\sim 7.3\text{‰}$ while the mafic rock has fictive quartz values that must be greater than the measured plagioclase values ($\delta^{18}\text{O} = \sim 8.1\text{‰}$) and are likely $\sim 9.2\text{‰}$. Isotopic compositions have been shown to remain constant during differentiation (Marks et al., 2007; Teng et al., in press) and therefore do not support or preclude a different source for the mafic and felsic Bushveld Complex rock. The isotopic composition of the mafic rock is consistent with the average of the deep continental crust (2.5‰; Teng et al., 2008) and measurements of MORB (1.5 to 5.6‰; Tomascak et al., 2008).

Teng et al. (in press) noted that mafic enclaves within A-type granites have Li concentrations ranging from 32 to 179 ppm, significantly greater than the host

granitic rocks. They attributed this difference to the compatible behavior of Li when mafic minerals such as hornblende and biotite crystallized, compared to the incompatible behavior of Li during feldspar and quartz crystallization. They also noted that the mafic enclaves likely represent mixing between mantle and crustal melts. Therefore, the crustal contamination of the Bushveld Complex magma, as well as the compatible behavior of Li during mafic mineral crystallization, could explain the greater concentration of the Bushveld Complex mafic rock relative to the felsic rock.

The amount of crustal contamination in the Bushveld Complex has been estimated from the greater $\delta^{18}\text{O}$ values of the mafic rock relative to the mantle derived rock with varying results. Schiffries and Rye (1989) estimated 10 to 30% crustal contamination based on $\delta^{18}\text{O}$ compositions of the mantle and upper crustal contaminants such as shales and granitic rocks, while Harris et al. (2003) determined crustal contamination could be as much as 30 to 40% using $\delta^{18}\text{O}$ compositions of the lower to middle crust. Mass balance of the Li compositions of the mantle and crustal rocks can also be investigated to explain the Li enriched mafic rock. The mantle is estimated to have between 1.6 to 1.8 ppm (Ottolini et al., 2004), while the deep continental crust was found to have an average Li concentration of 8 ppm (Teng et al., 2008). The average MORB concentration is 5 to 6 ppm, (Tomascak, 2004). Assuming that the mafic rock started with the lowest mantle concentration (1.6 ppm) and taking the 10% crustal contamination calculated by Schiffries and Rye (1989), mass balance shows that the crustal concentration of the contaminants would have to be 386 ppm. While this high concentration is found in pegmatites, it is not reasonable

that there would be pegmatites of the volume needed to contaminate the Bushveld Complex staging chamber. However, crustal contamination of 30% would indicate crustal concentrations of 130 ppm, which is possible for upper crustal rock (shale). Using the 40% contamination of Harris et al. (2003), the Li concentration of the mid to lower continental crust would have to be 98 ppm, which seems unreasonable since xenoliths of the lower continental crust were determined to range from 0.5 to 21 ppm and Archean metamorphic terranes representative of the middle continental crust ranged from 5 to 33 ppm (Teng et al., 2008). Even if the mafic rock started at the highest Li concentration measurement for deep continental crust concentration of 21 ppm, 40% crustal contamination would need rocks of 69 ppm, which also indicates shale or granite as the contaminant. Thus, the high Li concentration of the Bushveld Complex mafic rock suggests that mixing with a Li rich melt occurred, and the Li rich melt was most likely derived from upper crustal rocks. This would indicate that the staging magma chamber is not as deep in the crust as concluded by Harris et al. (2003), or the mafic magma was contaminated as it ascended through the continental crust as hypothesized by Schiffries and Rye (1989).

6.3: Lithium fractionation

The processes of Li fractionation, both concentration and isotopic, have recently been given much attention and study. These include weathering (Pistiner and Henderson, 2003; Teng et al., 2004; Rudnick et al., 2004; Kisakurek et al., 2004), disequilibrium fluid infiltration (Paquin and Altherr, 2002; Parkinson et al., 2007), metamorphic dehydration (Zack et al., 2003; Marschall et al., 2007; Teng et al., 2007), and diffusion of Li in contact metamorphic settings (Teng et al., 2006a; Marks

et al., 2007). Each of these processes is possible in the Phepane Dome-Bushveld Complex setting. Recent weathering has revealed the circular ridge of the Phepane Dome at the level of current exposure, metamorphic dehydration is probable within the metasedimentary rocks at the initiation of Phepane Dome formation, disequilibrium fluid infiltration could have occurred after Phepane Dome formation, and diffusion is possible during formation of the Phepane Dome. Each of these processes will be considered as a possible mechanism to explain the measured Li compositions.

The outcrops that samples were collected from must experience erosion to become exposed at the surface, where there is then the potential for chemical weathering. Precautions were taken during sampling to find the least weathered samples in the field. During sample preparation, the freshest part of the sample was isolated by cutting off the obviously weathered edges. However, there is still the potential for chemical weathering to have affected some of the measurements. Exposure of the outcrop to chemical weathering strips the ${}^7\text{Li}$ from the rock, since ${}^7\text{Li}$ prefers the fluid phase (Rudnick et al., 2004; Teng et al., 2004). Thus, seeing a lower concentration and lighter isotopic value than expected would indicate weathering. This trend is not apparent (Figure 20), as the lithologies have internally constant $\delta^7\text{Li}$ values with variable concentration. Lighter $\delta^7\text{Li}$ values are not accompanied by lower Li concentrations, so it is unlikely that weathering has affected any of the measurements.

Figure 20: Li concentration vs. Li isotopic composition

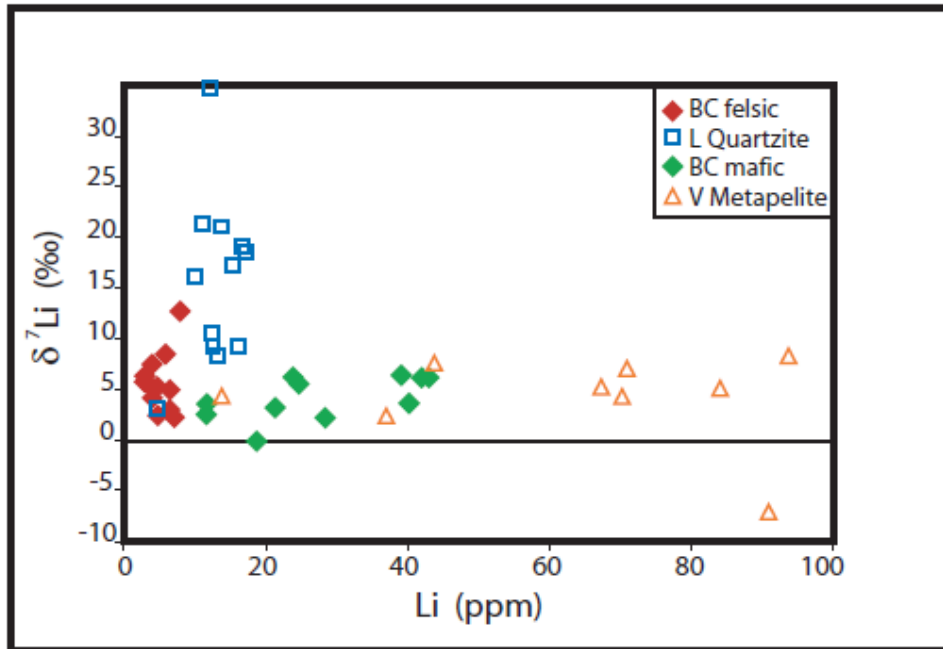


Figure 20: [Li] vs. $\delta^7\text{Li}$: There is no perceptible trend of [Li] reduction coinciding with isotopically lighter values. Each rock type is constant in $\delta^7\text{Li}$, while varying in [Li]. Only the Lakenvalei Quartzite has a large range of $\delta^7\text{Li}$ values. BC=Bushveld Complex, L=Lakenvalei, V=Vermont

Metamorphic dehydration is likely to have occurred in the sedimentary rocks as they were heated and partially melted during formation of the Phepane Dome. The sedimentary rocks were heated to temperatures greater than 750°C (Johnson et al., 2004). Marschall et al. (2007) showed that high temperature dehydration (400° to 670°C) can cause 42% Li loss and $\delta^7\text{Li}$ decrease of <3‰. This could explain the decrease in Vermont Metapelite (~65 ppm) concentration compared to the one Vermont Shale measurement (142 ppm). However, the metapelite does not preserve the isotopic signature of dehydration. When dehydration occurs, ^7Li is preferentially taken into the fluid relative to most minerals, which would cause lighter $\delta^7\text{Li}$ values in the Vermont metamorphic equivalent. Yet, the metapelite is isotopically heavier

than the protolith Vermont Shale and average shales around the world by 5‰. This means that before dehydration, the Vermont Shale would have to be between 5‰ and 8‰ to explain the average metapelite $\delta^7\text{Li}$. Although there is only one shale sample from the protolith Vermont Formation (0.3‰), it is unlikely that the rest of the shale started as heavy as 8‰. Shales contain an abundance of Li-rich clay minerals, which is exemplified by the high whole rock Li concentrations of shale. Clay minerals are the result of chemical weathering and are enriched in ^6Li during the low temperature weathering process, leading to isotopically light $\delta^7\text{Li}$ compositions (Rudnick et al., 2004; Wunder et al., 2006). The lighter Vermont Shale measurement (0.3‰) is therefore more likely to be representative of the initial Li composition, suggesting that metamorphic dehydration did not play an important role in defining the compositions of the Phepane Dome. So while it is likely that dehydration occurred during the formation of the Phepane Dome, this process does not explain the composition of the rocks we see today, and cannot be the dominant process in the Phepane Dome system.

The infiltration of a disequilibrium fluid can alter the Li composition of rocks through exchange of Li in the fluid and Li within the minerals. Previous studies of this mechanism have focused on metasomatism of subduction zone rocks by a Li-rich melt or fluid (Paquin and Altherr, 2002; Parkinson et al., 2007). In the Bushveld Complex, sources of fluid infiltration include the crystallization of mafic magma, crystallization of the felsic magma, or the dehydrating sedimentary rock. It is possible for these fluids to be out of equilibrium with one or more parts of the Phepane Dome-Bushveld Complex lithologies. Fluid from sedimentary dehydration

has already been discounted, but magmatic fluids, which would likely have the same composition as the source magma (Teng et al., 2007), are a possibility. The infiltration of the fluid produced by these magmas into the Phepane Dome and into crystallized regions of Bushveld Complex igneous rock could explain some of the observed Li compositions, and will be discussed in section 6.5.

The diffusion of Li through an intergranular medium is plausible for the partially melted and hydrous system of the Phepane Dome. Teng et al. (2006) determined that Li diffused through a magmatic fluid from the Tin Mountain pegmatite into country rock, and Marks et al. (2007) hypothesized that diffusion occurred through a Li-rich fluid from the Ilimaussaq intrusion of greater Li concentration into granitic country rock. Since Li diffusion is driven by a gradient in chemical potential, which is related to the concentration gradient, it is likely that there would be diffusion of Li from the Vermont Metapelite into the Lakenvalei Quartzite, and the Lakenvalei into the felsic Bushveld Complex rock. The contact of the mafic Bushveld Complex rock with the Phepane Dome is more complicated, because the mafic rock has a higher Li concentration than the Lakenvalei. Diffusion of Li into the Lakenvalei could occur at both the Vermont Metapelite and the mafic Bushveld Complex contacts. Nevertheless, diffusion is a valid mechanism for systematic Li decrease and increase in $\delta^7\text{Li}$ value, or Li gain and $\delta^7\text{Li}$ decrease, close to the contact (Marks et al., 2007). The diffusion of Li between the Phepane Dome and Bushveld Complex and models of this process will be discussed in section 6.5.

6.4: Oxygen models

For both transects, $\delta^{18}\text{O}$ compositions are relatively constant within a given lithologic unit, suggesting that limited oxygen isotopic exchange occurred across the lithologic contacts. Neither transect has enough data points at the contact that show the systematic across-contact variation in oxygen isotopic composition that defines a diffusive profile. However, profiles of limited isotopic exchange at the contact can be used to determine a maximum duration of diffusion. These profiles are constrained by the compositions of the two samples taken closest to the contact on either side. Starting with the East Phepane Transect 06 model, the initial oxygen isotopic compositions are taken from the average of the samples farthest from the contact. The best fit to the data is shown in Figure 21a, resulting in the solution to the model equation of $\sqrt{D_e t K_e^{-1}} = 1.1$ m. The best fit for this model and all models in this study is determined using the statistical χ^2 test (from Bevington and Robinson, 1992). Because the desired result of this model is the maximum duration of diffusion, the greatest possible diffusive distance that can still fit the data is also considered, as this will produce a greater time estimate. The greatest diffusive distance is $\sqrt{D_e t K_e^{-1}} = 1.4$ m (Figure 21c). This also tests the sensitivity of the model; however, the smallest diffusive distance cannot be determined because of the lack of data points at the contact that show a good diffusive profile across the contact.

The D_e for oxygen diffusion through melt is calculated ($D_e=10^{-16}$ m²/s) using the experimentally derived D for oxygen in silicate melt at low temperatures (800°C; $D=6 \times 10^{-14}$ m²/s, Oishi et al., 1975), the estimated porosity for melt ($\phi=0.01$), and the estimated tortuosity of the system ($\tau=1$). The diffusivity of O at 800°C was used

because the felsic melt would have a lower solidus temperature than the mafic magma, and the temperature of the partially melted core of the Phepane Dome was determined to be $>750^{\circ}\text{C}$ (Johnson et al., 2004). However, it should be noted that partial melt of the Phepane rock at these lower temperatures was likely fluid assisted, and therefore the experimentally determined diffusivity of O through rhyolite in the presence of water is likely a better proxy for the system ($9 \times 10^{-13} \text{ m}^2/\text{s}$ at 800°C , Behrens et al., 2007). The much slower diffusivity of O through an anhydrous melt will result in a maximum possible time estimate, while the effective diffusivity of O through a hydrous melt ($D_e = 10^{-15} \text{ m}^2/\text{s}$) may provide a more realistic time estimate. The porosity during the partial melt was estimated from the abundance of cusped plagioclase in the Lakenvalei Quartzite as a proxy for the amount of melt, and is probably a minimum constraint, which will also lead to a calculation of the maximum duration of diffusion. Lastly, the tortuosity is estimated as $\tau = 1$ for metamorphic rocks of these porosities (Cartwright and Valley, 1991).

To calculate the effective partition coefficient, the values for densities of the melt (ρ_f) and rock (ρ_s) need to be quantified. Gerya et al. (2004) used values for densities of the solid and molten Bushveld Complex granitic rock (2700 kg/m^3 and 2400 kg/m^3 respectively), as well as the solid and molten quartzites (2650 kg/m^3 and 2450 kg/m^3 respectively) in their model of Phepane diapirism. Thus, the values for ρ_f and ρ_s used in this model are 2400 and 2700 kg/m^3 for the melt and solid respectively. Using the same estimated porosity (ϕ) and a partition coefficient (K_c) for O of 0.55 (Cartwright and Valley, 1992), gives a K_e of 0.62 . The resulting time estimate for O isotopic exchange through anhydrous melt using the best fit model is 39 Myrs , while

the maximum time estimate is 62 Myrs. Using the diffusivity of O through hydrous rhyolitic melt gives a time estimate of 2.6 Myrs for the best fit model and 4.6 Myrs for the maximum diffusive distance. These time estimates represent the maximum time that diffusion could have occurred through melt to create the best fit profile.

Because diffusion has likely also occurred through an aqueous fluid, the range of time estimates for diffusion through aqueous fluid can be calculated. Using the diffusivity of oxygen through aqueous fluid ($D_o=10^{-8}$ m²/s; Bickle and McKenzie, 1987) and a porosity of 10^{-5} (Baxter and DePaolo, 2002), the slowest effective diffusivity through aqueous fluid is calculated ($D_e=10^{-13}$ m²/s). The effective partition coefficient utilizes the same K_c , but is larger for solid-fluid partitioning because the density of the fluid is now lower (800 kg/m³; $K_e= 1.86$) compared to the density of the melt. These parameters result in a time estimate for the best fit model of diffusion through aqueous fluid of 730 kyrs. The maximum time constraint of 1.2 Myrs is calculated from the larger diffusive distance. The lower constraint on time can also be calculated for diffusion through fluid using a greater porosity (10^{-3}). Keeping the rest of the parameters the same, a shorter time constraint is calculated as 7 kyrs for the best fit model and 12 kyrs for the larger diffusion distance.

Modeling of the West Small Scale Transect requires the calculated compositions of fictive quartz in the mafic Bushveld Complex rock to better constrain the extent of across-contact oxygen isotopic exchange with the Lakenvalei Quartzite. The compositions of the fictive quartz are calculated at 900°C, which is the preferred temperature as discussed above, and initial compositions are taken from the average of samples farthest from the contact. The best fit model results in a diffusive distance

of $\sqrt{D_e t K_e^{-1}} = 0.91$ m (Figure 21b), while the maximum possible diffusive distance is 1.5 m (Figure 21c). The calculation of time from these model diffusive distances utilizes the same effective partition coefficients for rock-melt ($K_e = 0.62$) and rock-aqueous fluid ($K_e = 1.86$), as well as the effective diffusivities for diffusion through fluid ($D_e = 10^{-13}$ m²/s and $D_e = 10^{-11}$ m²/s) that were used in the East Phepane model. However, the effective diffusivity is recalculated for diffusion through mafic magma. The diffusivity of oxygen through basalt melt at 900°C is 9×10^{-13} m²/s (Wendlandt, 1991), and using the same estimated porosity ($\phi = 0.01$) gives an effective diffusivity of $D_e = 9 \times 10^{-15}$ m²/s. For O diffusion through melt, the best fit model results in a time estimate of 1.6 Myrs and the maximum diffusive distance results in a time estimate of 4.9 Myrs. For O diffusion through aqueous fluid, the slower effective diffusivity constrains the greater time estimates of 490 kyrs and 1.3 Myrs for the best fit and maximum diffusive distance models respectively, while the faster effective diffusivity constrains a lower time constraint of 5 kyrs and 13 kyrs for each respective model.

Because there is evidence for both partial melt and aqueous fluid in the Phepane Dome rocks, the maximum time that oxygen isotopic exchange occurred between the Phepane Dome and Bushveld Complex rock is likely to be between 510 kyrs and 4.9 Myrs. The maximum time estimate is constrained by the slow diffusivity of oxygen through felsic melt, and the lack of data points closer to the contact. The lower time constraint is much shorter, due to the unknown porosity of the rocks during diffusion. This lower constraint uses the maximum porosity in the presence of an aqueous fluid. Smaller porosities result in greater time estimates, as seen through the maximum time estimate that used the smallest porosity.

Figure 21a-b: Models of oxygen isotopic exchange

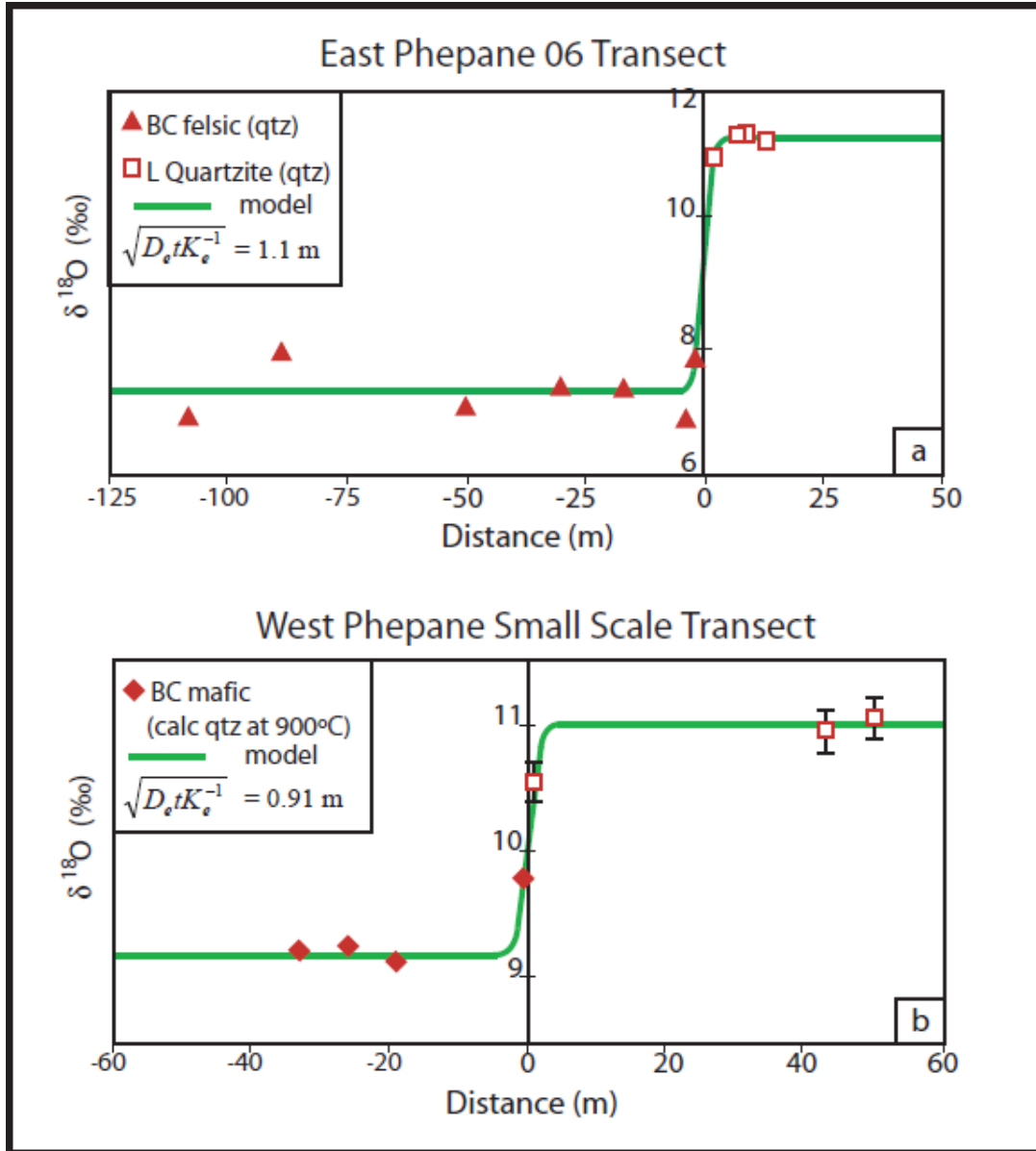


Figure 21: Models of oxygen isotopic exchange between the Bushveld Complex (BC) igneous rock (left) and the Lakenvalei (L) Quartzite (right), where $x=0$ is the contact. Note that each profile is constrained by the two samples on either side of the contact. **(a)** East Phepane model **(b)** West Phepane model. If no error bars are shown on data point, error is less than or equal to the size of the symbol.

Figure 21c: Maximum diffusive distance of oxygen isotope exchange model

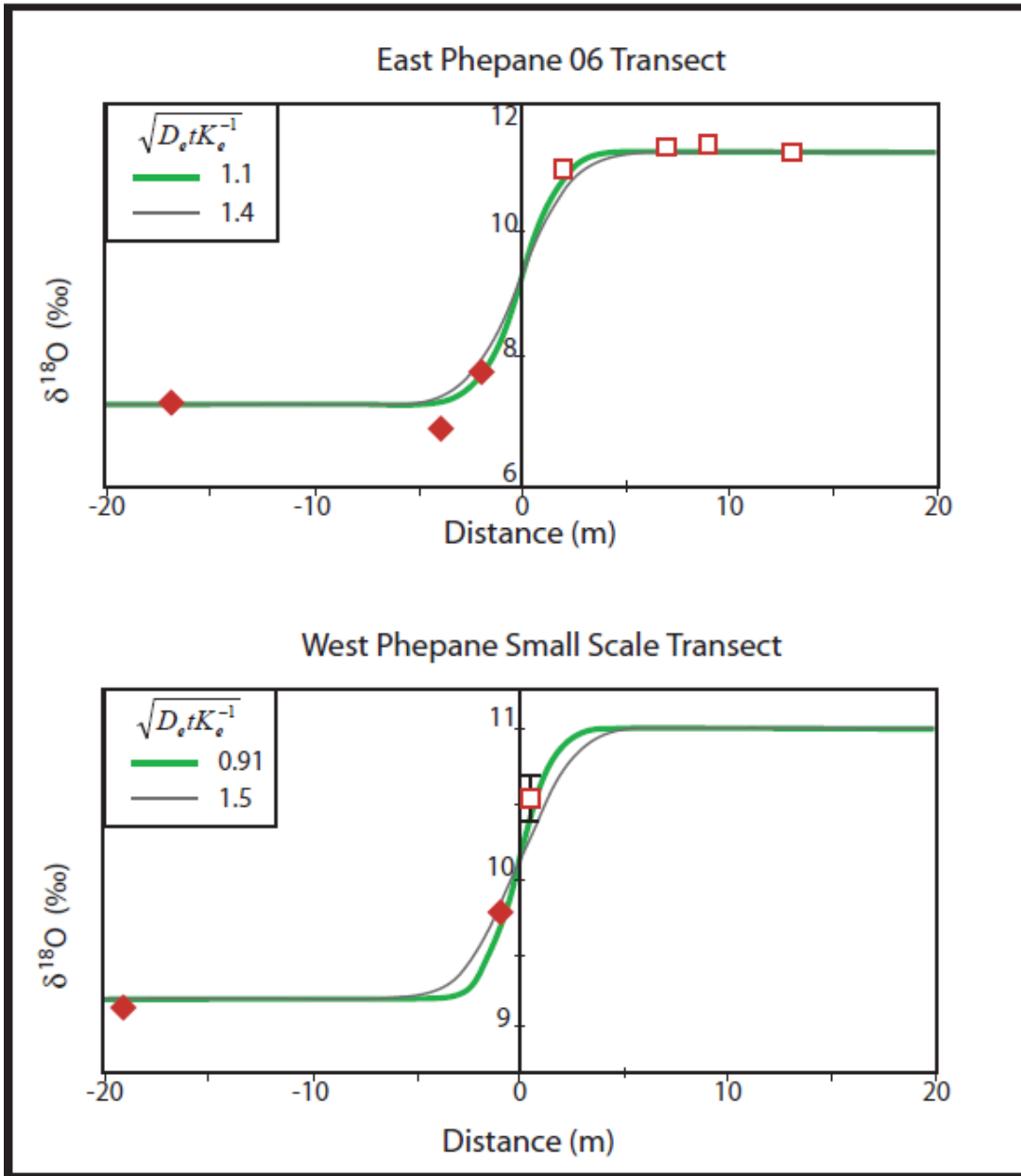


Figure 21c: Closer view of oxygen isotopic exchange models at the contact of the East Phepane 06 Transect (top) and the West Phepane Small Scale Transect (bottom). If no error bars are shown on data point, error is less than or equal to the size of the symbol. The best fit model is the green line, and the grey line is the maximum diffusive distance. The maximum diffusive distance is calculated from the model that just fits the two data points closest to the contact. A greater diffusive distance is not reasonable because it does not fit these two points.

6.5: Lithium models

The Li data is much more variable than the oxygen data, especially close to the contact in the East Transects. Most of the variability is likely due to diffusive exchange between the Phepane Dome and Bushveld Complex. However, in the East Phepane Transects and the West Small Scale Transects, there are three $\delta^7\text{Li}$ values of Bushveld Complex igneous rock at the contact that do not follow the trend of the rest of the data (P06-13, P06-14, and P07-31). These values are all isotopically lighter but show similar Li concentrations to the rest of the samples. One possible explanation for this is contact parallel flow of an isotopically light fluid within the igneous rock. Fluid infiltration was discussed as a possible way to fractionate Li through exchange of the minerals with the fluid. Because of the low partition coefficient of Li between rock and fluid (0.1, Brenan et al., 1998), the infiltrating fluid should reduce the Li concentration in the rock. Since the Li concentrations have not changed, it is possible that a Li-rich fluid altered these samples. Isotopic exchange between the metasedimentary rock and the fluid would shift the $\delta^7\text{Li}$ values depending on the mineral content. Wunder et al. (2006, 2007) determined that ^7Li preferentially fractionates into the fluid for fluid-mica and fluid-pyroxene exchange. Thus, these samples could have exchanged with a Li-rich fluid that was channelized by or restricted to the contact, and are therefore excluded from modeling of the Li isotopic composition and concentration profiles. Because the oxygen data do not show alteration at the contact, it is likely that this fluid infiltrated at a lower temperature (<500°C), after the quartz had closed to oxygen isotopic exchange.

Diffusion profiles were fit to the Li isotopic compositions and concentrations of the East Phepane Transects (Figure 22a). The models do not include the Vermont Metapelite, in order to simplify the model and allow for easier comparison to the oxygen model. Initial Li isotopic compositions and concentrations of the felsic Bushveld Complex rock and the Lakenvalei Quartzite were taken from the average composition of samples farthest from the contact; the Li compositions of the protolith Lakenvalei Sandstone were not used because of the uncertain variation in Li composition and the unknown influence of the fluid inclusions in the quartz as discussed above. The best fit model solution to equation (2) is $\sqrt{D_e t K_e^{-1}} = 14.1$ m, one order of magnitude greater than the oxygen model. Again, to attain a maximum duration of diffusion and to examine the sensitivity of the model, the smallest and largest diffusive distances that will still fit the data are determined to be 11.0 m and 20.1 m respectively. The β value used in this model is 0.17, which is the value that best fits the data (see Figure 22b). This value is consistent with previously determined β values. It is greater than the β values used by Teng et al. (2006) for Li diffusion through a magmatic fluid (0.12 to 0.15), but less than the β value determined by Richter et al. (2003) for Li diffusion through melt (0.215). To calculate the resultant duration of diffusion (t) for this model, the diffusion of Li through a melt phase and an aqueous fluid phase will be considered.

First, for diffusion through melt, the effective diffusivity and effective partition coefficient must be constrained. The diffusivity of Li in a rhyolitic melt was experimentally determined by Richter et al. (2003) to be almost three orders of magnitude larger than other major components of the melt. This gives a diffusivity of

Li in silicate melt at 800°C of $\sim 10^{-10}$ m²/s based on the diffusivity of O through silicate melt. Using the same porosity and tortuosity as the oxygen model, the effective diffusivity is calculated as $D_e = 10^{-12}$ m²/s. The same density parameters of the Phepane Dome and Bushveld Complex rocks are used in the calculation of the effective partition coefficient, but the K_c of Li must be quantified. There is one available experimental value of a solid-melt partition coefficient from Brenan et al. (1998). This value is used (0.1), but qualified with the caveat that it is for cpx-melt and not the compositions or minerals of this transect. Using these values, the effective partition coefficient is $K_e = 0.12$. Solving the best fit model equation for (t) results in a time estimate of 760 kyrs, while the range in time estimates calculated from the minimum and maximum diffusive distances is 470 kyrs to 1.5 Myrs. These constraints assume that diffusion occurs only through the partial melt, and represent the minimum and maximum amount of time needed to produce the Li data.

The duration of diffusion through an aqueous fluid can also be calculated using available constraints on the diffusivity of Li through fluid and the Li solid-fluid partition coefficient. The diffusivity of Li through pure water at 25°C has been determined as $\sim 10^{-9}$ m²/s (Li and Gregory, 1974). This is an extreme minimum diffusivity, since the temperature is so low. In addition, Teng et al. (2006) point out that the diffusivity of Li through an intergranular aqueous fluid would have a different bonding environment, since Li would be coordinated differently than the Li coordination with water molecules. This possible difference in Li diffusivity has not been quantified. Richter et al. (2003) determined that Li diffused approximately two orders of magnitude faster than the other major element constituents of a basaltic

melt, but almost three orders of magnitude faster in a rhyolitic melt. To calculate the maximum duration of diffusion, a slower diffusivity ($10^{-6} \text{ m}^2/\text{s}$) is used, since this is two orders of magnitude larger than oxygen diffusion through fluid. Using the same porosity constraints described above for oxygen diffusion through aqueous fluid calculates an effective diffusivity of $10^{-11} \text{ m}^2/\text{s}$. The effective partition coefficient is increased due to the lower density of the fluid ($K_e = 0.34$). Solving the best fit model equation for (t) with these parameters results in a duration of 210 kyrs, while the smaller and larger diffusive distances constrain a range from 130 to 430 kyrs. Using the greater porosity with the same parameters yields a lower constraint on the time estimate of 2 kyrs, with a corresponding range of 1 to 4 kyrs.

The West side of the Phepane Dome is remarkable because the mafic rock is enriched in Li but isotopically lighter than the Lakenvalei Quartzite. This produces a different Li diffusion profile than the East Phepane. The Li source in this case is the mafic rock, which preferentially loses ^6Li close to the contact due to the faster diffusion of the lighter isotope. The mafic rock becomes heavier near the contact, while the Li-poor Lakenvalei Quartzite on the other side becomes lighter as it gains ^6Li . Because the Lakenvalei starts out heavier, the $\delta^7\text{Li}$ values decrease systematically as the contact is approached. This produces the opposite effect than what is seen in previously modeled Li diffusion profiles (Teng et al., 2006a; Marks et al., 2007), which all had the higher Li concentrations correlated with higher $\delta^7\text{Li}$ values. The best fit model to the West Phepane Small Scale Transect shows this effect (Figure 23). Using initial conditions taken from the average values for samples farthest from the contact, the solution to equation (2) results in $\sqrt{D_e t K_e^{-1}} = 14.2 \text{ m}$,

the same as the East Phepane model. The range in diffusive distances is smaller, with a maximum of 18.1 m and a minimum of 13.0 m.

To calculate the duration of diffusion for this model, the same constraints on the effective partition coefficient and porosity may be used. Because the West Transect contains mafic igneous rock, the diffusivity for Li through melt is likely different than the diffusivity used for the previous felsic model. The diffusivity of Li through basaltic melt was determined to be approximately two orders of magnitude greater than the major constituents of the melt (Richter et al., 2003). The diffusivity of oxygen through basaltic melt at 900°C was experimentally determined to be $9 \times 10^{-13} \text{ m}^2/\text{s}$ (Wendlandt, 1991). The D of oxygen at 900°C was chosen because the solidus used in the two previous studies that provide time constraints is 900°C, and using the slower diffusivity at a lower temperature will calculate the maximum duration of diffusion. Because the partial melt in the Lakenvalei Quartzite would be felsic, through which Li would diffuse almost three orders of magnitude faster than oxygen, a diffusivity of $10^{-10} \text{ m}^2/\text{s}$ was used (effective diffusivity of $10^{-12} \text{ m}^2/\text{s}$). This results in a best fit time estimate for Li diffusion through melt of 710 kyrs, and a range from 600 kyrs to 1.2 Myrs determined from the range in diffusive distances. The best fit model produces similar time estimates (220 kyrs) to the East Phepane model for diffusion through fluid, and a slightly more constrained range in time from the smaller range in diffusive distance (180 to 350 kyrs). The corresponding lower time constraints from Li diffusion through aqueous fluid are a best fit of 2 kyrs and a range from 2 to 4 kyrs (see Table 6 for time estimates).

It should be noted that applying these parameters and modeling to the data points at the contact that were hypothesized to be affected by contact parallel fluid flow produces time estimates that are too short to be realistic geologic timescales. For example, the time estimates from the model of Li diffusion through fluid is a range from 8 to 800 yrs, and diffusion through melt gives a time estimate of 200 yrs. Thus, it is reasonable to exclude these data points, as they do not produce sensible time estimates. In addition, the data from the West Phepane Large Scale Transect does not show a good fit to any diffusion profile. Using the solutions to the other Li models does not reproduce the profile of measured isotopic data, especially in the Lakenvalei Quartzite (Figure 24).

Table 6: Time estimates from Diffusion Models

Oxygen						
			$\sqrt{D_e t K_e^{-1}}$	1.1 m*	1.4 m [†]	
East Phepane		porosity	K_e	t (kyrs)	t (kyrs)	
D_{melt}	$9 \times 10^{-13} \text{ m}^2/\text{s}$	10^{-2}	0.62	2600	4200	
D_{fluid}	$10^{-8} \text{ m}^2/\text{s}$	10^{-3}	1.86	7	12	
D_{fluid}	$10^{-8} \text{ m}^2/\text{s}$	10^{-5}	1.86	730	1200	
			$\sqrt{D_e t K_e^{-1}}$	0.91 m*	1.5 m [†]	
West Phepane		porosity	K_e	t (kyrs)	t (kyrs)	
D_{melt}	$9 \times 10^{-13} \text{ m}^2/\text{s}$	10^{-2}	0.62	1600	4900	
D_{fluid}	$10^{-8} \text{ m}^2/\text{s}$	10^{-3}	1.86	5	13	
D_{fluid}	$10^{-8} \text{ m}^2/\text{s}$	10^{-5}	1.86	490	1300	
Lithium						
			$\sqrt{D_e t K_e^{-1}}$	14.1 m*	11.0 m ⁺	20.1 m [†]
East Phepane		porosity	K_e	t (kyrs)	t (kyrs)	t (kyrs)
D_{melt}	$10^{-10} \text{ m}^2/\text{s}$	10^{-2}	0.12	760	470	1500
D_{fluid}	$10^{-6} \text{ m}^2/\text{s}$	10^{-3}	0.34	2	1	4
D_{fluid}	$10^{-6} \text{ m}^2/\text{s}$	10^{-5}	0.34	210	130	430
			$\sqrt{D_e t K_e^{-1}}$	14.2 m*	13.0 m ⁺	18.1 m [†]
West Phepane		porosity	K_e	t (kyrs)	t (kyrs)	t (kyrs)
D_{melt}	$10^{-10} \text{ m}^2/\text{s}$	10^{-2}	0.12	710	600	1200
D_{fluid}	$10^{-6} \text{ m}^2/\text{s}$	10^{-3}	0.34	2	2	4
D_{fluid}	$10^{-6} \text{ m}^2/\text{s}$	10^{-5}	0.34	220	180	350

Table 6: Time estimates in thousands of years for the duration of diffusion between the Bushveld Complex and the Phepane Dome. The longer timescales of the oxygen models is due to the lack of data points closer to the contact. *Best fit diffusive distances. [†]Minimum diffusive distances. ⁺Maximum diffusive distances.

Figure 22a: Model of Li diffusion in the East Phepane

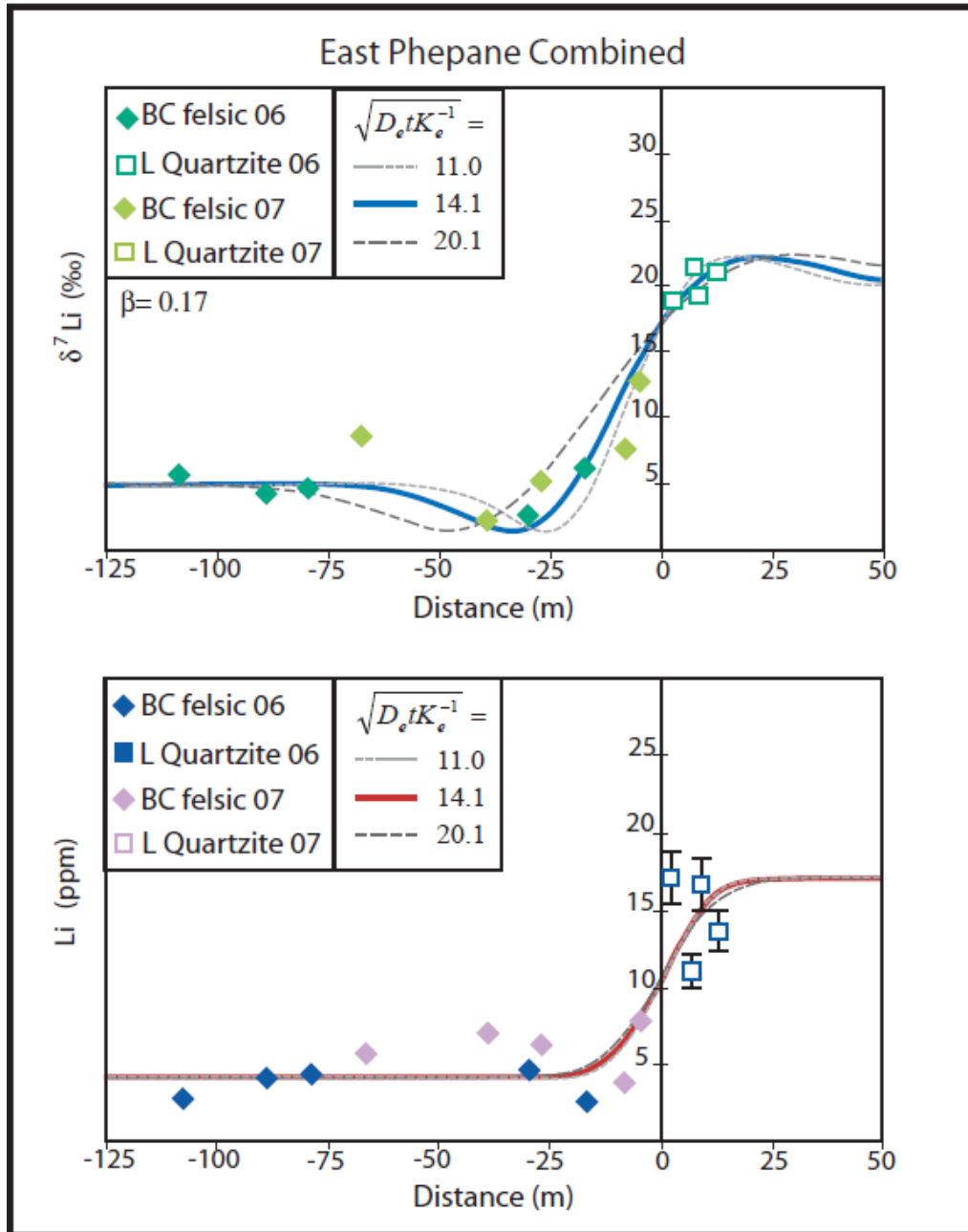


Figure 22a: Models of Li diffusion between the Lakenvalei (L) Quartzite (right) and the Bushveld Complex (BC) felsic rock (left) in the East Phepane, where $x=0$ is the contact: **(top)** Best fit $\delta^7\text{Li}$ model **(bottom)** The corresponding best fit [Li] model.

Figure 22b: Beta values of the East Phepane model

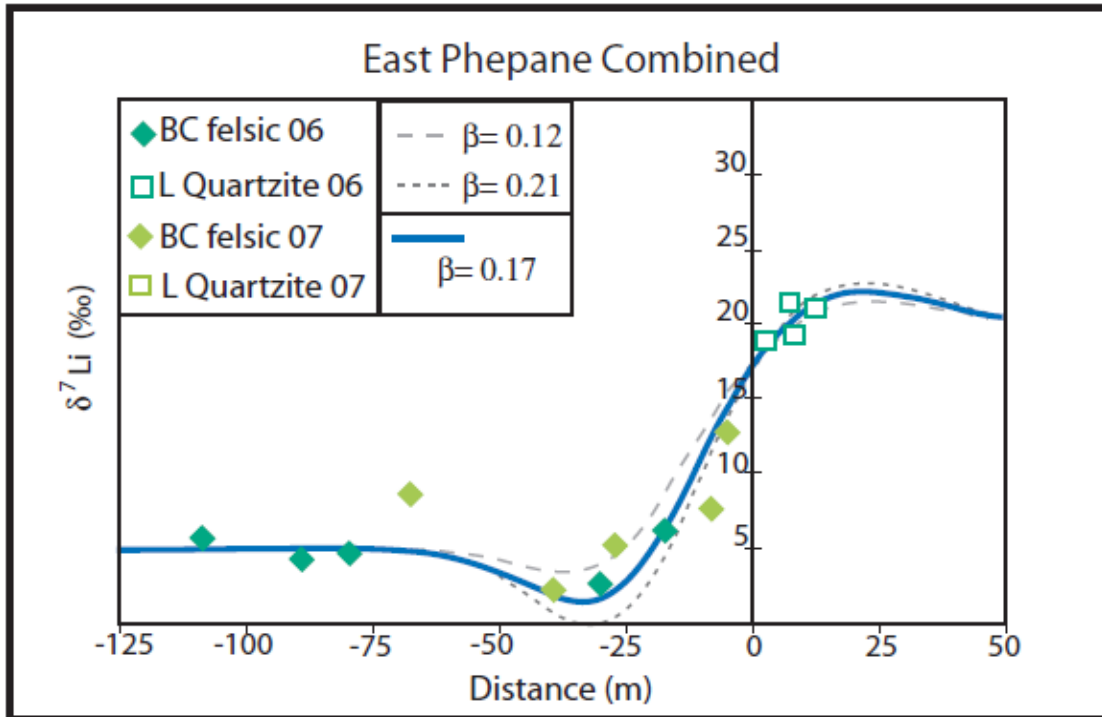


Figure 22b: Best fit model from Figure 22a ($\sqrt{D_e t K_e^{-1}} = 14.1$), shown with different β values (0.12 for diffusion through supercritical fluid from Teng et al., 2006; 0.21 for diffusion through melt from Richter et al., 2003).

Figure 23: Model of Li diffusion in the West Phepane Small Scale Transect

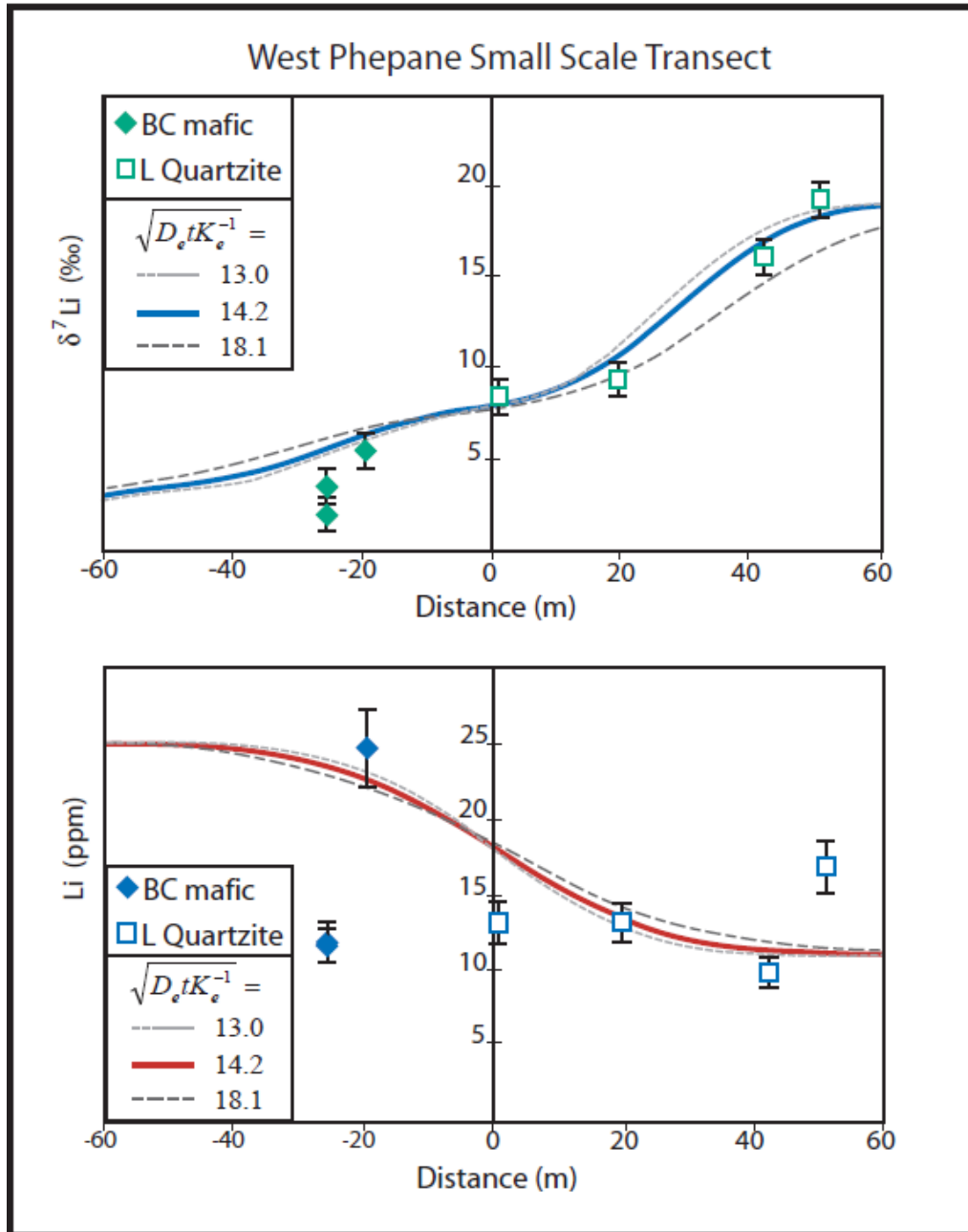


Figure 23: Models of Li diffusion between the Lakenvalei (L) Quartzite (right) and the Bushveld Complex (BC) mafic rock (left) in the West Phepane Small Scale Transect, where $x=0$ is the contact: **(top)** Best fit $\delta^7\text{Li}$ model: The difference in Li diffusion profile when compared to the East Phepane is explained by the greater initial concentration in the isotopically light mafic rock relative to the isotopically heavier Lakenvalei Quartzite. **(bottom)** The corresponding best fit [Li] model.

Figure 24: Model of Li diffusion in the West Phepane Large Scale Transect

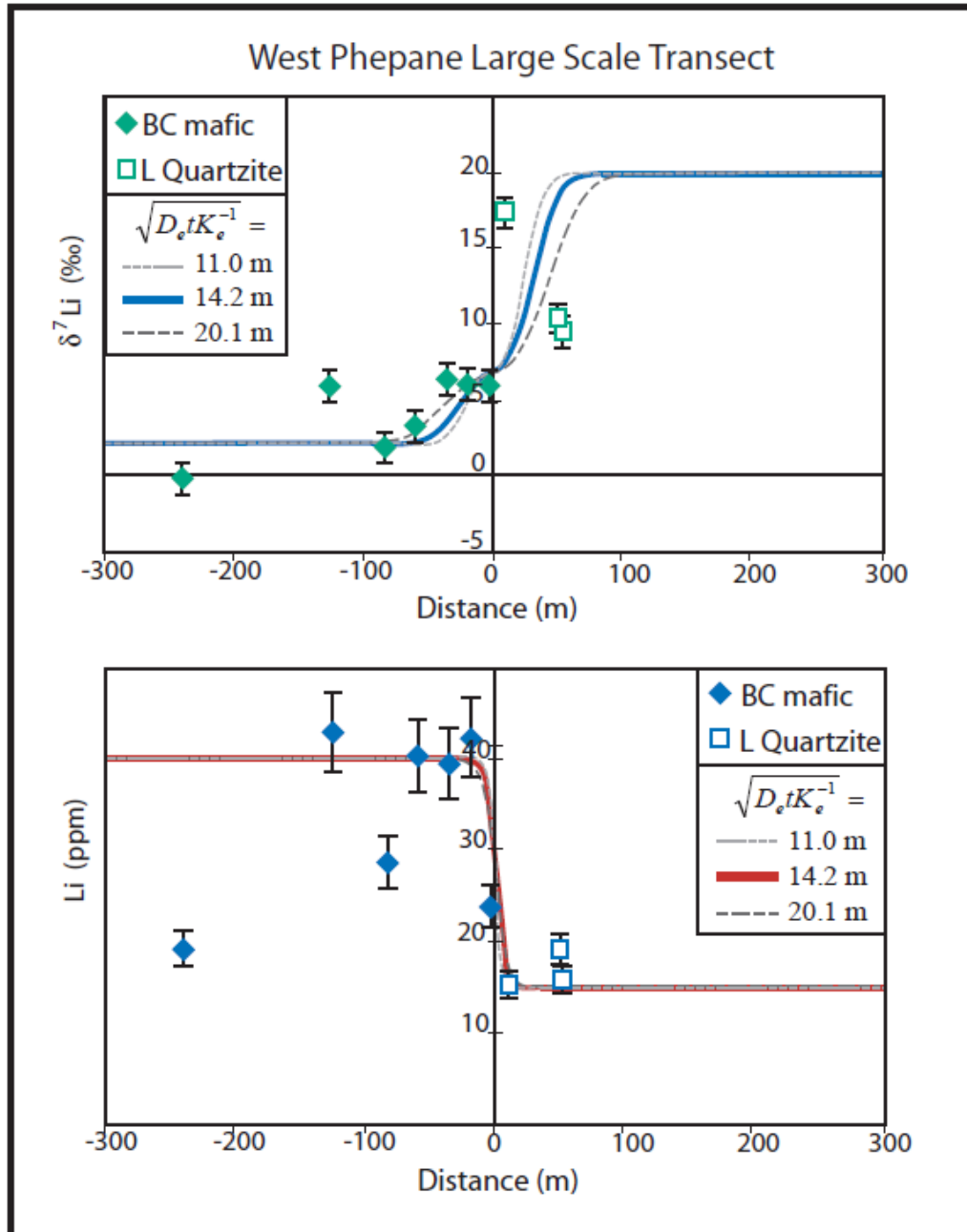


Figure 24: Models of Li diffusion between the Bushveld Complex (BC) mafic rock (left) and the Lakenvalei (L) Quartzite (right) in the West Phepane Large Scale Transect, where $x=0$ is the contact: **(top)** The $\delta^7\text{Li}$ model using the same parameters as the West Phepane Small Scale Transect model **(bottom)** The corresponding [Li] model. This model shows a better fit to most of the data compared to the $\delta^7\text{Li}$ model.

6.6: Li and O diffusion timescales

The model time estimates are representative of the amount of time that Li and O were able to exchange between the Bushveld Complex and the Phepane Dome, which is used as a proxy for the duration of Phepane Dome formation. This assumes that the duration of Phepane diapirism is related to the length of time these two systems can exchange. The start and end of this exchange are dependent on three factors that enable diffusion: the chemical potential (concentration) gradient, the temperature of the system, and the presence of an intergranular medium. Because a chemical potential gradient is related to the concentration gradient, and the Phepane Dome and Bushveld Complex have distinctly different Li concentrations and O isotopic compositions, it is likely that exchange between the two lithologies would occur. Therefore, the limiting factors that control the duration of isotopic exchange are the temperature and the presence of an intergranular medium.

First, the start of isotopic exchange in the Bushveld Complex-Phepane Dome system depends on when the Phepane Dome rock reaches temperatures greater than the closure temperatures for O and Li as the sedimentary rock is heated by the mafic magma. For oxygen, quartz mineral separates were measured, so this is the temperature that oxygen in quartz becomes available for exchange, ~500°C (Giletti, 1985). Lithium diffuses more quickly through minerals than oxygen (Parkinson et al., 2007), so it is likely that Li has a lower closure temperature in minerals compared to oxygen. This has been shown to be the case for Li diffusion through country rock of a pegmatite at temperatures of 350°C to 600°C (Teng et al., 2006a). This means that Li would likely start to exchange with an intergranular fluid and diffuse through

the Bushveld Complex-Phepane Dome system before oxygen. This can be also applied to the end of both Li and O diffusion in the system. Lithium would likely continue to exchange and diffuse after 500°C, when O is closed to quartz. This means that the Li system should record a longer time period of exchange. While this is not certain from the data, it is possible that the O system records a shorter timescale than the Li system. Even so, the temperatures attained by the Phepane Dome during diapirism must have been greater than 500°C, because diapirism is dependent on the underlying Transvaal sedimentary rock being partially melted. This indicates that from the temperature perspective, diffusive exchange would occur throughout the entire development of the Phepane diapir.

The presence of an intergranular medium is crucial for diffusion to be able to occur between the Bushveld Complex and the Phepane Dome, since volume diffusion is orders of magnitude slower. The first appearance of an intergranular medium in the Phepane rocks is likely a fluid related to the Bushveld intrusion. A dehydration fluid could have been released by the Transvaal sedimentary rock during heating from the magma intrusion, so it is possible that diffusion began before diapirism was initiated. However, even if there was no aqueous fluid for diffusion before diapirism, the partial melt of the sedimentary rock during diapirism would provide an intergranular medium for diffusion. If diffusion is confined to only the melt stage, it would cease as the system crystallized and the diapir was frozen in. It seems unlikely that diffusion would end after each rock type is completely crystallized, since there is evidence for a post-magmatic aqueous fluid. Therefore, diffusion would cease when the fluid left the system or when the temperature fell below the closure temperature of

the diffusant. The evidence for partial melt and for aqueous fluid indicates that there must have been at least a partial melt phase present during Phepane Dome diapirism, and that diffusion continued through an aqueous fluid after crystallization of the partial melt and the Bushveld magma. Therefore, an intergranular medium would also be present for a longer timescale than the formation of the Phepane Dome.

The final consideration of the duration of Li and O diffusion is what effect the diapirism would have on the crystallizing Bushveld magma at the contact. Because the Phepane diapir rises into the mafic magma, it is possible for the diapir to exchange with different magma than what is seen at the contact now. While this would affect the profile seen in the Bushveld rock, the Phepane rock would record the entire duration of exchange (e.g., the profile seen in the Lakenvalei Quartzite of the West Phepane Small Scale Transect). Because the Phepane metasedimentary rocks have retained the stratigraphy of the sedimentary protoliths, the Lakenvalei Quartzite was likely always at the contact exchanging with the Bushveld Complex throughout diapirism. In addition, the model by Gerya et al. (2004) of the Phepane diapir development suggests that some of the mafic magma could be entrained by the diapir as it rose (see Figure 2). If this is the case, diffusive exchange would occur between the same Lakenvalei Quartzite and Bushveld Complex igneous rock throughout diapirism of the Phepane Dome, and the Bushveld igneous rock sampled at the contact today would have also recorded the entire duration of exchange.

Chapter 7: Conclusions

7.1: The Phepane Dome-Bushveld Complex system

The $\delta^{18}\text{O}$ compositions, Li concentrations and $\delta^7\text{Li}$ compositions of the Lakenvalei Quartzite in the Phepane Dome and igneous rock of the Bushveld Complex indicate that there has been limited oxygen isotopic exchange but quantifiable Li diffusion between the Phepane Dome and Bushveld Complex. Across-contact oxygen isotopic exchange likely occurred over a scale of <2 m from either side of the contact, while isotopic exchange of Li (specifically ^6Li) reached distances of 50 m from the contact. Because there is evidence for the presence of both partial melt and aqueous fluid over the metamorphic history of the Lakenvalei Quartzite, it is probable that diffusional exchange occurred through one or both of these intergranular media. Measurements of quartz-quartz-feldspar dihedral angles in thin sections of the Lakenvalei Quartzite suggest that an interconnected partial melt occupied grain boundaries during metamorphism, and CL images show that recrystallization overgrowth of quartz occurred in the presence of fluid. The blue luminescence of the overgrowths indicates that recrystallization occurred at relatively high temperature, which is supported by the high temperatures attained by the Phepane Dome ($>750^\circ\text{C}$, Johnson et al., 2004). Therefore, both a melt phase and a fluid phase were present during contact metamorphism of the Phepane Dome. Because it cannot be determined if diffusional exchange occurred through only one phase, the modeling of O and Li isotopic diffusion takes into account both possible media.

7.2: Modeling of lithium and oxygen isotopic exchange

The O and Li isotopic exchange across the contact of the Phepane Dome and the Bushveld Complex igneous rock were modeled using a one-dimensional solution to Fick's second law of diffusion for the four localities. Each of these models was fit to the measured compositions of the traverses across the contact of the Lakenvale Quartzite and Bushveld Complex igneous rock. The measurements of oxygen isotopic compositions indicate that there was limited oxygen isotopic exchange. The extent of diffusion in the East Phepane 06 Transect is constrained by only the two points at ~2 m on either side of the contact, and the West Phepane Small Scale Transect is constrained by only the two data points at <1 m from either side of the contact. Although the two models agree with each other, sampling with closer spacing near the contact might provide a better constraint on the diffusive distance. For the oxygen compositions in this study, the best fit model determined a diffusive distance, $\sqrt{D_e t K_e^{-1}}$ of ~1.0 m.

Solutions to Fick's second law were also modeled for Li concentrations and isotopic compositions for three of the four transects. All three produced similar best fit solutions for $\sqrt{D_e t K_e^{-1}}$ of ~14.1 m, one order of magnitude greater than diffusive distance determined for oxygen isotopic exchange. This is reasonable because of the faster diffusivity of Li compared to O. The time for diffusion is likely the same for both isotopic systems, and the porosity used in the calculation of effective diffusivity is the same. Effective partition coefficients differ by a maximum of one order of magnitude, but the diffusivity of Li can be up to three orders of magnitude greater. The result is broader Li diffusion profiles spanning the contact when compared to the

more limited profile of oxygen isotopic exchange. The greater diffusive distance of Li relative to O indicates that the Li isotopic and compositional system is a better tool for modeling events of shorter timescales.

The similar calculated diffusive distances and the good fit of the models for the three Li profiles from both sides of the Phepane Dome suggest that both sides are recording the same contact metamorphism event, whether this is diffusion through the partially melted Lakenvalei Quartzite and crystallizing Bushveld Complex magma, diffusion through an aqueous fluid, or both. The poor fit of the fourth transect, the West Phepane Large Scale Transect, is possibly explained by the added isotopic exchange with a metasedimentary structure at the side of the Phepane Dome.

The East Phepane Transects show similar Li diffusion profile shapes as observed in previous studies of Li diffusion (Teng et al., 2006; Marks et al., 2007), but the West Phepane Small Scale Transect has a different profile shape. This is because the source of Li (the rock type with a greater concentration of Li) in this case is the isotopically lighter mafic rock. In the East Transects, the rock type with the greater Li concentration was isotopically heavier. Nevertheless, the agreement of the calculated diffusive distances from the East and West side of the Phepane Dome indicates that these diffusive profiles developed during the contact metamorphism of the Phepane Dome, and likely represent the duration of Phepane Dome formation.

7.3: Time estimates

The time estimates for O and Li isotopic exchange produced by these models have an extremely large range of 2 kyrs to 62 Myrs, representing the possible durations of isotopic exchange and diffusion required to produce the measured

compositional profiles. The models of oxygen isotopic exchange have the greatest time estimates, due to the slower diffusivity of O and also due to the limited amount of data points close to the contact. A distinct diffusive profile of $\delta^{18}\text{O}$ compositions across the contact was not observed in the available data, and the maximum time constraints are dependent on only the two data points closest to the contact.

Therefore, these models are not as reliable as the Li data that show a broader diffusive profile. It is also significant that the time estimates of the modeling of Li measurements do not support the longer timescales of the oxygen model, as the maximum possible diffusion duration is 1.5 Myrs for Li diffusion through felsic melt and the best fit models have a maximum of 760 kyrs. Because oxygen likely has a higher closure temperature than Li, the oxygen system should record a shorter timescale than Li, and not the greater time estimates seen. Therefore, preference for the duration of diffusive exchange is given to the time estimates determined by the Li models. Thus, the time constraints based on the best fit of the Li models produce a likely duration range of 2 kyrs to 760 kyrs for the formation of the Phepane Dome.

The goal of this study is to constrain the time of Phepane Dome formation using the diffusion of O and Li isotopes between the Bushveld Complex and the Phepane Dome. The two previous models that provide time constraints on the formation of the Phepane Dome are a model of the cooling and crystallization of the Bushveld Complex (200 kyrs: Cawthorn and Walraven, 1998), and a model of the development of the Phepane diapir (1 Myrs: Gerya et al., 2004). The time estimates from this study constrain a similar range, with the likely duration range of 2 to 760 kyrs, and maximum time estimates greater than 1 Myrs for both O and Li diffusion.

A longer timescale than the 200 kyrs for crystallization and cooling of the Bushveld Complex is consistent with the assumption that diffusive exchange between the Bushveld Complex and the Phepane Dome should continue after the Bushveld magma is completely crystallized. The maximum time estimates are also consistent with the development of the diapir in 1 Myrs, although the best fit models might suggest a slightly shorter timescale, since diffusion should also continue after the diapir has been frozen in. Thus, these models of diffusive exchange are in good agreement with previous models of the time for Phepane Dome formation, indicating that this technique is a viable method for constraining timescales of geologic events such as contact metamorphism and diapirism.

This study has shown the utility of both Li and O isotopic exchange as meaningful methods for determining the timescales of contact metamorphic events. In this case, Li provided more useful information because of the greater diffusivity of Li relative to O. Thus, the application of two isotopic systems of varying diffusivity is recommended for settings of unknown timescales. In addition, this study used important constraints on the diffusivity of Li from experimental studies of Li diffusion and comparisons to the well studied system of O isotopic exchange. The resultant order of magnitude difference between the O and Li diffusive distances indicates that Li is able to diffuse more rapidly in contact metamorphic settings, consistent with the experimental findings. This comparison of Li to O diffusion was crucial in the quantification of the parameters used in modeling (e.g., the orders of magnitude difference in diffusivities). The consistent time estimates from both

isotopic exchange models and the similarity to previous timescale estimates strengthens the comparison of two isotopic systems.

References

- Baxter, E.F., and D.J. DePaolo, 2002. Field measurement of high temperature bulk reaction rates II: Interpretation of results from a field site near Simplon Pass, Switzerland. *Am. J. Sci.* 304: 465-316.
- Bevington, P.R., and D.K. Robinson, 1992. Data reduction and error analysis for the physical sciences. The McGraw-Hill Companies, Inc. New York City, p. 219.
- Bickle, M.J., and D. McKenzie, 1987. The transport of heat and matter by fluids during metamorphism. *Contrib. Mineral. Petrol.* 95: 384-392.
- Buick, I.S., Maas, R., and R. Gibson, 2001. Precise U-Pb titanite age constraints on the emplacement of the Bushveld Complex, South Africa. *J. of Geol. Soc. (London, U.K.)*. 158: 3-6.
- Brenan, J.M., Ryerson, F.J., and H.F. Shaw, 1998. The role of aqueous fluids in the slab-to-mantle transfer of boron, beryllium, and lithium during subduction. *Geochim. Cosmochim. Acta.* 62: 3337-3347.
- Bryant, C.J., Chappell, B.W., Bennett, V.C., and M. T. McCulloch, 2004. Lithium isotopic compositions of the New England Batholith: correlations with inferred source rock compositions. *Transactions of the Royal Society of Edinburgh- Earth Sciences.* 95:199-214.
- Cartwright, I., and J.W. Valley, 1991. Steep oxygen-isotope gradients at marble-metagranite contacts in the northwestern Adirondack Mountains, New York, USA: products of fluid-hosted diffusion. *Earth Planet. Sci. Lett.* 107, 148-163
- Cawthorn, R.G., and F. Walraven, 1998. Emplacement and Crystallization Time for the Bushveld Complex. *J. Petrol.* 39 no. 9, 1669-1687.
- Cawthorn, R.G., 1999. The platinum and palladium resources of the Bushveld Complex. *South African Journal of Science.* 95: 481-489.
- Chan, L.H., Leeman, W.P., and T. Plank, 2006. Lithium isotopic composition of marine sediments. *Geochem. Geophys. Geosyst.* 7, Q06005.

- Clarke, B.M., Uken, R., Watkeys, M.K., and J. Reinhardt, 2005. Folding of the Rustenburg Layered Suite adjacent to the Steelpoort pericline: implications for syn-Bushveld tectonism in the Eastern Bushveld Complex. *South African Journal of Geology*. 108: 397-412.
- Clayton, R.N., and T.K. Mayeda, 1963. The use of bromine pentafluoride in the extraction of oxygen from oxides and silicates for isotopic analysis. *Geochim. Cosmochim. Acta*. 27, 43-52.
- Clayton, R.N., and S.W. Kiefer, 1991. Oxygen isotope thermometer calibrations. In Taylor, Jr., H.P., O'Neil, J.R., and I.R. Kaplan, (eds.) *Stable Isotope Geochemistry: A Tribute to Samuel Epstein*. Special Publication. 3: 3-10.
- Cole, D.R., and S. Chakraborty, 2001. Rate and Mechanisms of Isotopic Exchange. In Valley, J.W., and Cole, D.R., (eds.) *Reviews in Mineralogy and Geochemistry: Stable Isotope Geochemistry*. V.43: 84-223.
- Crank, J., *The Mathematics of Diffusion*. Oxford University Press, Oxford, 1975. p. 414.
- Eriksson, P.G., Altermann W., Catuneanu, O., van der Merwe, R., and A.J. Bumby, 2001. Major influences on the evolution of the 2.67-2.1 Ga Transvaal basin, Kaapvaal craton. *Sediment. Geol. Special Issue*. 241:205-231.
- Fritz, S.J., 1992. Measuring the ratio of aqueous diffusion-coefficients between $^7\text{LiCl}$ and $^6\text{LiCl}$ by osmometry. *Geochim. Cosmochim. Acta*. 56: 3781-3789.
- Gerya, T.V., and D.A. Yuen, 2003. Rayleigh-Taylor instabilities from hydration and melting propel 'cold plumes' at subduction zones. *Earth Planet. Sci. Lett.* 212: 47-62.
- Gerya, T.V., Uken R, Reinhardt J, Watkeys M.K., Maresch W.V., and B.M. Clarke, 2003. Cold fingers in a hot magma: Numerical modeling of country-rock diapirs in the Bushveld Complex, South Africa. *Geology*. 39 (9): 753-756.
- Gerya, T.V., Uken, R., Reinhardt, J., Watkeys, M.K., Maresch, W.V., and B.M. Clarke, 2004. "Cold" diapirs triggered by intrusion of the Bushveld Complex: Insight from two-dimensional numerical modeling. *Geol. Soc. Am. Special Paper* 380.

- Giletti, B.J., 1989. Diffusion effects on oxygen isotopic temperatures of slowly cooled igneous and metamorphic rocks. *Earth Planet. Sci. Lett.* 77: 218-228.
- Giletti, B.J. and R.A. Yund, 1984. Oxygen diffusion in quartz. *J. Geophys. Res.* V. 89, B6: 4039-4046.
- Götze, J., Plotze, M., and D. Habermann, 2001. Origin, spectral characteristics and preactical applications of the cathodoluminescence (CL) of quartz- a review. *Mineral. Petrol.* 71: 225-250.
- Govindaraju, K., 1995. 1995 Working Values with Confidence-Limits for 26-CRPG, ANRT, and IWG-GIT Geostandards. *Geostandards Newsletter.* v. 19 Special Issue: 1-32.
- Hall, P.S., and C. Kincaid, 2001. Diapiric Flow at Subduction Zones: A Recipe for Rapid Transport. *Science.* 292: 2472-2475.
- Harris, N., McMillan, A., Holness, M., Uken, R., Watkeys, M., Rogers, N., and A. Fallick, 2003. Melt Generation and Fluid Flow in the Thermal Aureole of the Bushveld Complex. *J. Petrol.* 44 no. 9, 1031-1054.
- Harris, C., Pronost, J.J.M., Ashwal, L.D., and R.G. Cawthorn, 2005. Oxygen and Hydrogen Isotope Stratigraphy of the Rustenburg Layered Suite, Bushveld Complex: Constraints on Crustal Contamination. *J. Petrol.* 46 (3): 575-601.
- Hill, M., Barker, F., Hunter, D., and R. Knight, 1996. Geochemical Characteristics and Origin of the Lebowa Granite Suite, Bushveld Complex. *International Geology Review.* 38 (3), 195-227.
- Holness, M.B., 1998. Contrasting rock permeability in the aureole of the Ballachulish igneous complex, Scottish Highlands: the influence of surface energy? *Contrib Mineral Petrol.* 131: 86-94.
- Jeffcoate, A.B., Elliott, T., Thomas, A., and C. Bouman, 2004. Precise, small sample size determinations of lithium isotopic compositions of geological reference materials and modern seawater by MC-ICP-MS. *Geostand. Geoanal. Res.* 28: 161-172.
- Johnson, T.E., Gibson, R.L., Brown, M., Buick, I.S., and I. Cartwright, 2003. Partial melting of metapelitic rocks beneath the Bushveld Complex, South Africa. *J. Petrol.* 44 (5): 789-813.

- Johnson, T., Brown, M., Gibson, R., and B. Wing, 2004. Spinel-cordierite symplectites replacing andalucite: evidence for melt-assisted diapirism in the Bushveld Complex, South Africa. *J. Metamorph. Geol.* 22, 529-545.
- Kinnaird, J.A., Hutchinson, D., Schurmann, L., Nex, P.A.M., and R. de Lange, 2005. Petrology and mineralization of the southern Platreef: northern limb of the Bushveld Complex, South Africa. *Miner. Deposita.* 40: 576-597.
- Kisakurek B., Widdowson, M., and R.H., James, 2004. Behavior of Li isotopes during continental weathering: The Bidar laterite profile, India. *Chem. Geol.* 212: 27-44.
- Kretz, R., 1983. Symbols for rock forming minerals. *Am. Mineral.* 68: 227-279.
- Li, Y.H. and S. Gregory, 1974. Diffusion of ions in seawater and deep sea sediments. *Geochim. Cosmochim. Acta.* 38 (5): 703-714.
- Marks, M.A.W., Rudnick, R.L., McCammon, C., Vennemann, T., and G. Markl, 2007. Arrested kinetic Li isotope fractionation at the margin of the Ilimaussaq complex, South Greenland: Evidence for open-system processes during the final cooling of per-alkaline igneous rocks. *Chem. Geol.* 246: 207-230.
- Marschall, H.R., Altherr, R., and L. Rupke. 2007a. Squeezing out the slab – modeling the release of Li, Be and B during progressive high-pressure metamorphism. *Chem. Geol.* 239: 323-335.
- Marschall, H.R., Pogge von Strandmann, P.A.E., Seitz, H.M., Elliott, T., and Y. Niu, 2007b. The lithium isotopic composition of orogenic eclogites and deep subducted slabs. *Earth Planet. Sci. Lett.* 262: 563-580.
- Molyneux, T.G., and P.S. Klinkert. 1978. A structural interpretation of part of the eastern mafic lobe of the Bushveld Complex and its surrounds. *Transactions of the Geological Society of South Africa.* 81,359-368.
- Moriguti, T., and E. Nakamura. 1998. High-yield lithium separation and the precise isotopic analysis for natural rock and aqueous samples. *Chem. Geol.* 145 (1-2): 91-104.
- Oishi Y., Terai, R., and H Ueda, 1975. Oxygen diffusion in liquid silicates and relation to their viscosity. In Cooper A.R., Huer A.H., (eds) *Mass Transport Phenomena in Cerams* 9:297-310. Plenum Press, New York.

- Ottolini, L., Le Fevre, B., and R., Vannucci, 2004. Direct assessment of mantle boron and lithium contents and distribution by SIMS analyses of peridotite minerals. *Earth Planet. Sci. Lett* 228: 19-36.
- Paquin, J., and R. Altherr, 2002. Subduction-related lithium metasomatism during exhumation of the Alpe Arami ultrahigh-pressure garnet peridotite (Central Alps, Switzerland). *Contrib. Mineral. Petrol.* 145 (5): 623-640.
- Park, W.R., Ripley, E.M., Severson, M., and S. Hauck, 1999. Stable isotopic studies of mafic sills and proterozoic metasedimentary rocks located beneath the Duluth Complex, Minnesota. *Geochim. Cosmochim. Acta.* 6, 657-674.
- Parkinson, I.J., Hammond, S.J., James, R.H., and N.W. Rogers, 2007. High-temperature lithium isotopic fractionation: Insights from lithium isotope diffusion in magmatic systems. *Earth Planet. Sci. Lett.* 257; 609-621.
- Penniston-Dorland, S., 2001. Illumination of vein quartz textures in a porphyry copper ore deposit using scanned cathodoluminescence: Grasberg Igneous Complex, Irian Jaya, Indonesia. *Am. Mineral.* 86: 652-666.
- Pistiner, J.S., and G.M. Henderson, 2003. Lithium-isotope fractionation during continental weathering processes. *Earth Planet. Sci. Lett.* 214: 327-339.
- Richter, F.M., Davis, A.M., DePaolo, D.M., and E.B. Watson, 2003. Isotope fractionation by chemical diffusion between molten basalt and rhyolite. *Geochim. Cosmochim. Acta.* 67, 3905-3923.
- Roedder, E., Fluid Inclusions, *Reviews in Mineralogy* v.12. 1984, Mineralogical Society of America, Chicago. P. 45.
- Rudnick, R.L., Tomascak, P.B., Njo, H.B., and R.L. Gardner, 2004. Extreme lithium isotopic fractionation during continental weathering revealed in saprolites from South Carolina. *Chem. Geol.* 212, 45-57.
- Schiffries, C.M., and D.M. Rye, 1989. Stable isotopic systematics of the Bushveld Complex: I. Constraints on magmatic processes in layered intrusions. *Am. J. Sci.* 289: 841-873.
- Schiffries, C.M., and D.M. Rye, 1990. Stable isotopic systematics of the Bushveld Complex: II. Constraints on hydrothermal processes in layered intrusions. *Am. J. Sci.* 290: 209-245.

- Shieh, Y.N., and H.P. Taylor, Jr., 1969. Oxygen and carbon isotope studies of contact metamorphism of carbonate rocks. *J. Petrol.* 10, 307-331.
- Sprunt, E., Dengler, L., and D. Sloan, 1978. Effects of metamorphism on quartz cathodoluminescence. *Geology.* 6: 305-308.
- Teng, F.Z., McDonough, W.F., Rudnick, R.L., Dalpe, C., Tomascak, P.B., Chappell, B.W., and S. Gao, 2004. Lithium isotopic composition and concentration of the upper continental crust. *Geochim. Cosmochim. Acta* 68 20, 4167-4178
- Teng, F.Z., McDonough, W.F., Rudnick, R.L., and R.J. Walker, 2006a. Diffusion-driven extreme lithium isotopic fractionation in country rocks of the Tin Mountain pegmatite. *Earth Planet. Sci. Lett.* 243, 701-710.
- Teng, F.Z., McDonough, W.F., Rudnick, R.L., Walker, R. J., and M.C. Sirbescu, 2006b. Lithium isotopic systematics of granites and pegmatites from the Black Hills, South Dakota. *Am. Mineral.* 91: 1488-1498.
- Teng, F.-Z., McDonough, W.F., Rudnick, R.L., and B.A. Wing, 2007. Limited lithium isotopic fractionation during progressive metamorphic dehydration in metapelites: a case study from the Onawa contact aureole, Maine. *Chem. Geol.* 239, 1–12.
- Teng, F.-Z., Rudnick, R.L., McDonough, W.F., Gao, S., Tomascak, P.B., and Y. Liu, 2008. Lithium isotopic composition and concentration of the deep continental crust. *Chem. Geol.* 255: 47-59.
- Teng, F.-Z., Rudnick, R.L., McDonough, W.F., and F.-Y. Wu, 2009. Lithium isotopic systematics of A-type granites and their mafic enclaves: Further constraints on the Li isotopic composition of the continental crust. *Chem. Geol.* In press.
- Tomascak, P.B., 2004. Developments in the Understanding and Application of Lithium Isotopes in the Earth and Planetary Sciences. *Reviews in Mineralogy & Geochemistry.* 55: 153-196.
- Tomascak, P.B., Langmuir, C.H., le Roux, P.J., and S.B. Shirey, 2008. Lithium isotopes in global mid-ocean ridge basalts. *Geochim. Cosmochim. Acta.* 72: 1626-1637.
- Uken, R., and M.K. Watkeys, 1997. Diapirism initiated by the Bushveld Complex, South Africa. *Geology.* 25 no. 8, 723-726.

- Valley et al., 1995. UWG-2, a garnet standard for oxygen isotopic ratios: Strategies for high precision and accuracy with laser heating. *Geochim. Cosmochim. Acta.* 59 (24): 5223-5231.
- Valley, J.W., and C.M. Graham, 1996. Ion microprobe analysis of oxygen isotope ratios in quartz from Skye granite: Healed micro-cracks, fluid flow, and hydrothermal exchange. *Contrib. Mineral. Petrol.* 124: 225-234.
- Van der Plas, L., and A.C. Tobi, 1965. A chart for judging the reliability of point counting results. *Amer. J. Science.* 263: 37-90.
- Vernon, R.H., 1968. Microstructures of high-grade metamorphic rocks at Broken Hill Australia. *J. Petrol.* 9: 1-22.
- Walraven, F., Armstrong, R.A., and F.J. Kruger, 1990. A chronostratigraphic framework for the north-central Kaapvaal craton, the Bushveld Complex and Vredefort structure. *Tectonophysics.* 171, 23-48.
- Watson, E.B., and E.F. Baxter, 2007. Diffusion in solid Earth systems. *Earth Planet. Sci. Lett.* 253. 307-327.
- Wendlandt, R.W., 1991. Oxygen diffusion in basalt and andesite melts: Experimental results of chemical versus tracer diffusion. *Contrib. Mineral. Petrol.* 108, 463-471.
- Wunder, B., Meixner, A., Romer, R.L., Feenstra, A., Schettler, G., and W. Heinrich, 2007. Lithium isotope fractionation between Li-bearing staurolite, Li-mica and aqueous fluids: An experimental study. *Chem. Geol.* 238: 277-290.